

# Dissertation

submitted to the

Combined Faculties of the Natural Sciences and Mathematics  
of the Ruperto-Carola-University of Heidelberg, Germany

for the degree of

Doctor of Natural Science

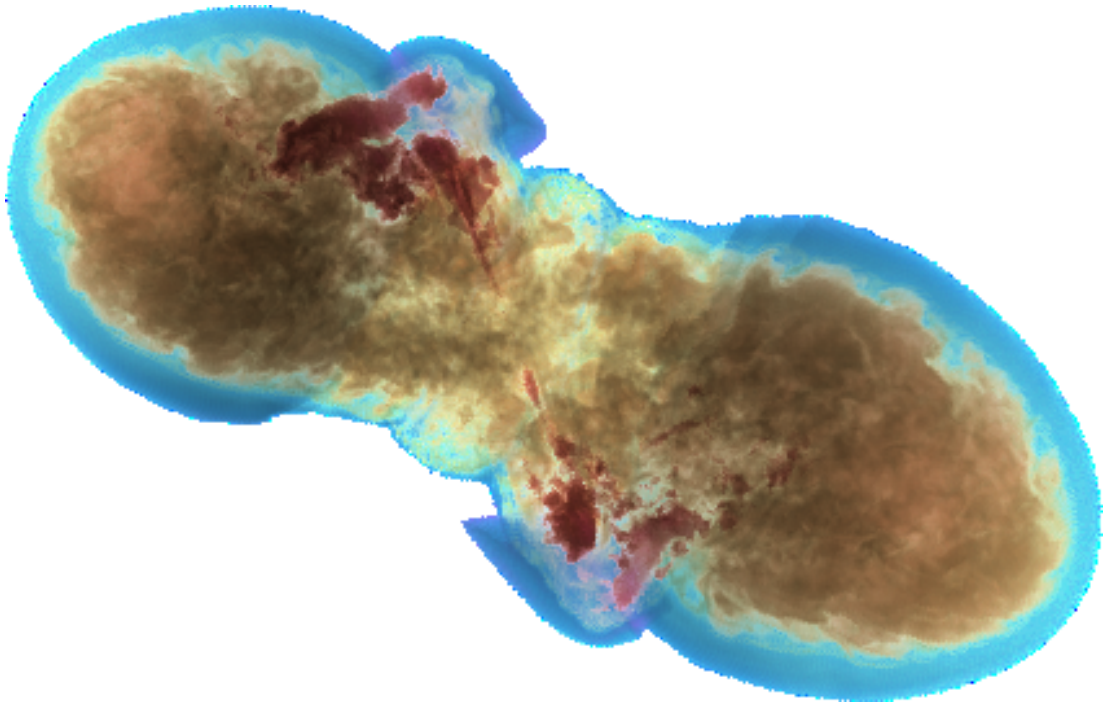
Put forward by

Salvatore Cielo

Born in: Palermo, Italy

Oral Examination: 2015-02-06





---

---

# Numerical Models of AGN Jet Feedback

---

---

Referees:           Dr. Andrea Valerio Macciò  
                          Prof. Dr. Björn Malte Schäfer



# Zusammenfassung

**Numerische Modelle des AGN-Feedbacks** - Die Kerne aktiver Galaxien (AGNs) treiben die leuchtkräftigsten Quellen im Universum und erzeugen die auf großen Skalen beobachteten, sehr energiereichen Radio-Jets. Diese Prozesse sind wichtig für die Modelle und numerischen Simulationen, die die Entstehung von Galaxien untersuchen, und die die Energie der AGN benötigen, um eine zu starke Kühlung des Gases im Zentrum zu verhindern.

In dieser Dissertation untersuchen wir mit Hilfe hydrodynamischer Simulationen den Einfluß von Jets auf das inter-galaktische Medium individueller Halos, insbesondere für den Fall massereicher Galaxien. Für die Simulationen wurde der FLASH Code verwendet. Dabei ermöglichte das Verfahren der adaptiven Gitterverfeinerung die komplexen, auf verschiedenen Längenskalen arbeitenden physikalischen Prozesse auf Skalen von Mpc bis hinunter auf einige zehn pc aufzulösen.

Im ersten Teil der Dissertation beschreiben wir detailliert die ersten Millionen Jahre der Jetentwicklung, wobei wir deren Entwicklungsstadien präzise identifizieren und unserer Ergebnisse durch Vergleiche mit theoretischen Modellen testen. Wir diskutieren die Zirkulationswege des Gases durch den "Kokon", den die Jets gegraben haben, und untersuchen einen möglichen Zusammenhang mit einer Selbstregulierung der Jetaktivität.

Im zweiten Teil erweitern wir unsere Untersuchung auf kosmologisch relevante Zeitskalen. Wir untersuchen detailliert die Thermodynamik des Jet-Gas-Systems, und berücksichtigen dabei die mechanische Arbeit, die geleistet wird, den globalen Energiehaushalt und den Volumenanteil des Gases, das durch den Jet erhitzt wird.

Schließlich diskutieren wir einige Erweiterungen unseres Model, wie z.B. mehrmalige Jet-Episoden, und versuchen eine Brücke zu schlagen zu einem direkten Vergleich mit Beobachtungen im Röntgenbereich.

# Abstract

**Numerical Models of AGN Jet Feedback** - Active Galactic Nuclei (AGNs) power the most luminous sources in the Universe, and generate very energetic large-scale radio jets. These processes are important in galaxy formation models and numerical simulations, which require energy from AGNs to prevent central gas from overcooling.

In this thesis we use hydrodynamical simulations to explore the impact of jets on the intra-galactic medium of individual halos, with particular focus on massive galaxies. The simulations are performed with the FLASH code, and we took advantage of the Adaptive Mesh Refinement scheme to deal with the complex, multiscale physics of AGNs on scales ranging from Megaparsec down to a few tens of parsecs.

In the first part of this thesis we describe in detail the first few millions years of AGN jets, identifying precise evolutionary stages and testing our findings against theoretical models. We discuss gas circulation within the “cocoon” carved by the jet as a possible self-regulation mechanism for jet activities.

In the second part, we extend the analysis to cosmologically relevant timescales, and carry on a detailed thermodynamyc analysis of the jet-gas system, including mechanical work, global energy transfer and volume fraction of the heated gas. Finally, we present a few extensions of our model such as multiple jet events, and take a few steps towards direct comparison with X-ray observations.

*To Sicily*



“Thus, it was established thousands of years ago that the Universe as a whole, in its full complexity, cannot be represented by any simulation smaller than itself. In other words, you can’t get any picture of the Universe as a whole except by studying the entire Universe.”

(Isaac Asimov, Prelude to Foundation)



---

# Table of Contents

---

1	Introduction: Active Galactic Nuclei	17
1.1	What shines the brightest? . . . . .	17
1.1.1	Brightest, and fundamental . . . . .	21
1.2	AGNs and jets . . . . .	22
1.2.1	The AGN unified model . . . . .	22
1.2.2	Jet launching . . . . .	24
1.2.3	Comparison of astrophysical jets . . . . .	27
1.3	AGN Feedback . . . . .	28
1.3.1	The inefficient star formation and the overcooling problem . . . . .	28
1.3.2	AGN feedback in models of galaxy formation . . . . .	31
2	Jets with the FLASH Code	33
2.1	Introduction to Computational Fluid Dynamics and FLASH . . . . .	34
2.1.1	The Navier-Stokes equations . . . . .	36
2.1.2	Equation of State . . . . .	37
2.2	Discretization: Meshes and Adaptive Mesh Refinement . . . . .	38
2.2.1	Discretization: the finite volumes method . . . . .	38
2.2.2	Riemann solvers . . . . .	40
2.2.3	Adaptive Mesh Refinement in FLASH . . . . .	40
2.3	Complete list of the FLASH Units . . . . .	42

2.4	Our setup . . . . .	45
3	Early Evolution Stages of Jet/ISM Interaction	49
3.1	What we can learn from the early stages . . . . .	49
3.2	Simulation setup and runs . . . . .	52
3.2.1	Simulation volume . . . . .	52
3.2.2	Scaling relations, host galaxy and jet parameters . . . . .	54
3.3	Evolutionary stages . . . . .	56
3.4	Cocoon geometry . . . . .	59
3.5	Cocoon thermodynamics . . . . .	62
3.6	Backflow . . . . .	66
3.6.1	Overview on Backflow . . . . .	66
3.6.2	Backflow stability . . . . .	71
3.7	Discussion . . . . .	74
4	Long-term Evolution of the Jet/ISM System	77
4.1	Setup and simulation description . . . . .	79
4.2	Energy coupling with the halo gas . . . . .	80
4.3	Hot bubbles and volume coverage . . . . .	84
4.4	Discussion . . . . .	87
5	Work in Progress	89
5.1	Jet tilting . . . . .	89
5.1.1	Kinematics of powerful jets: recollimation shocks . . . . .	93
5.2	Cold clouds . . . . .	93
5.3	Synthetic X-ray images . . . . .	97
6	Summary and Conclusions	101
	References	104

---

## List of Figures

---

1.1	AGN unification scheme . . . . .	18
1.2	HST picture of a quasar . . . . .	20
1.3	AGNs' spectral features . . . . .	23
1.4	AGN unification scheme . . . . .	25
1.5	Multiwavelength view of Hercules A. . . . .	29
1.6	Stellar-halo mass relation . . . . .	30
2.1	FLASH's homepage headline . . . . .	34
2.2	AMR example in a jet simulation . . . . .	35
2.3	2D sample block with guard cells . . . . .	41
2.4	Sketch of the different componets in our setup . . . . .	47
3.1	3D ray-tracing density rendering . . . . .	50
3.2	Early jet stages . . . . .	56
3.3	Visual comparison varying jet and halo properties . . . . .	58
3.4	Geometrical properties of the cocoon . . . . .	59
3.5	Total pressure evolution . . . . .	61
3.6	Thermodynamics of the cocoon . . . . .	63
3.7	Mechanical $pdV$ work done by the cocoon expansion . . . . .	65
3.8	Central velocity field . . . . .	66
3.9	Gas mass evolution around the central region . . . . .	67

3.10	Sketch of backflow model . . . . .	69
3.11	Vorticity and specific angular momentum . . . . .	70
3.12	Conditions for existence of unstable K-H modes . . . . .	74
4.1	Chandra X-ray image of the Perseus Cluster . . . . .	78
4.2	Evolution of the SC <sub>42</sub> and FC <sub>42</sub> runs . . . . .	81
4.3	Gas total energy and coupling constant . . . . .	83
4.4	Advanced bubble phase . . . . .	85
4.5	Volume coverage . . . . .	86
5.1	Jet angle flipping . . . . .	91
5.2	Jet angle flipping 3D . . . . .	92
5.3	Recollimation shocks . . . . .	94
5.4	A single cold cloud . . . . .	95
5.5	A few clouds in a test run without jets . . . . .	96
5.6	Mesh refinement around a single cloud . . . . .	96
5.7	Jet encountering a single cloud . . . . .	97
5.8	Sample of synthetic X-ray images . . . . .	99

---

## List of Tables

---

1.1	Luminosity comparison of the most notable astrophysical sources. . . . .	19
1.2	Comparison of astrophysical jets. . . . .	28
3.1	Early jets: simulation parameters . . . . .	53
4.1	Parameters and timings for all the simulation runs. . . . .	82



---

# Introduction: Active Galactic Nuclei

---

## 1.1 What shines the brightest?

As soon as the *Homo Sapiens Sapiens*, after his appearance on Earth, was set with food and shelter, he started to look up to the skies. With a little fright, much hope, but most of all, endless curiosity.

The light sources we humans, from Earth, can see in the night sky with our unaided eye or portable binoculars are actually located no farther than a few thousand parsecs from the Sun, limited to about 8th visual magnitude, in excellent dark sky condition. The closest celestial bodies belong to the Solar System, but the most of these sources are isolated objects (mostly individual stars) in the solar neighborhood. There were the spectacular meteor showers, such as the *Perseids*, but apart from some intrinsic variability, and small individual proper motions - just for the most focusing observers - these objects did not appear to do very much, suggesting our ancestors quite a static picture of the cosmos. For millennia our understanding of the Universe has thus been biased by our geocentric perspective; the idea that the cosmos may be something lively and evolving (in some cases, even withing a single human lifespan) is rather new.

Yet, there always been a few exceptions, hints that there is more: *the Sagittarius arm* of our own Milky Way (Figure 1.1) is an astonishing view since the dawn of man; even a few extra-galactic sources are visible with no observational instruments, mostly bright nearby galaxies such as the *Andromeda Galaxy*, *M33*, *Centaurus A*.

Less than ten (galactic) *Supernova* events visible by naked eye have been recorded throughout human history; we would happily celebrate the birth of a new star (hence the name *Nova*, though *Novae* and *Supernovae* relate in fact to the death of a star); and indeed their appearance helped very much the developement of astronomy as a science, although it took quite long before we could regard at all this information from the right perspective.



**Figure 1.1:** Night sky above Paranal, ESO's Very Large Telescope (VLT) site, on 21 July 2007. The scene features a magnificent view of the Sagittarius Arm of the Milky Way, besides the VLT's laser guidance system. Credit: ESO/Yuri Beletsky. From <http://www.eso.org/public/images/eso0733a/>.

After having built countless telescopes, that have been providing us with a deep, and multi-wavelength view of the Universe, we now know quite well how it would look like for an unbiased observer, if any exists. In a nutshell: our current cosmological models assume that the Universe, on its largest scales, is homogeneous and isotropic; so the local observation point does not matter. We also know much about how structure initially forms and evolves (in the standard cosmological model), from the small to the large scales in a hierarchical fashion. We do not fully understand its composition yet, dominated on large scales by the little intelligible *Dark Energy*. But as we look at smaller scales, matter gets more and more important. Though the cosmic baryon -i.e. ordinary matter- fraction is today just about 5%, the rest being Dark Matter, only baryons participate in electro-magnetic interaction, thus it is all we can *look* at.

So, what would be the most prominent features our unbiased observer would see? In other words, what shines the brightest? Which astrophysical objects have the highest absolute magnitude?

Compiling Table 1.1 was quite an instructive task. In this table, the luminosity of the most notable astrophysical sources are compared: individual stars, which dominate our naked-eye views, do not even get close.

Supernovae are remarkably powerful; yet there are other point-like objects capable of outshining the entire galaxy that hosts them! Among these, *Gamma-Ray Bursts* have the highest peak luminosity, but are powered by extremely short-lived explosive events, a mere few seconds. This shortest class of GRBs we mention are believed to be

Source	Radius	Powered by	Luminosity erg/s	Lifetime years
Sun (G2 Main Sequence star)	$7 \times 10^6$ km	proton-proton chain	$3.846 \times 10^{33}$	$10^{10}$
R136a1 (Giant Wolf-Rayet star)	$2.45 \times 10^8$ km	Thermonuclear reactions in shell	$3.37 \times 10^{40}$	few $\times 10^6$
Type Ia Super Nova	$1 \times 10^5$ km <sup>a</sup>	Runaway nuclear burning (C, O)	$2. \times 10^{43}$	0.01 (peak)
M87 (Giant elliptic galaxy)	$\approx 150$ kpc	$\approx 10^{13}$ stars	$2. \times 10^{44}$	several $10^9$
Short Gamma Ray Burst	few km <sup>b</sup>	Binary neutron star merger	$10^{51}$	$6 \times 10^{-8}$ (2s)
Typical Quasar	0.05 pc	Gravito-magnetic engine <sup>c</sup>	$10^{46}$	$10^7$

<sup>a</sup>Estimated radius of a white dwarf star

<sup>b</sup>Order of magnitude of a neutron star radius

<sup>c</sup>Thermal + Blandford-Znajek processes from accretion disk

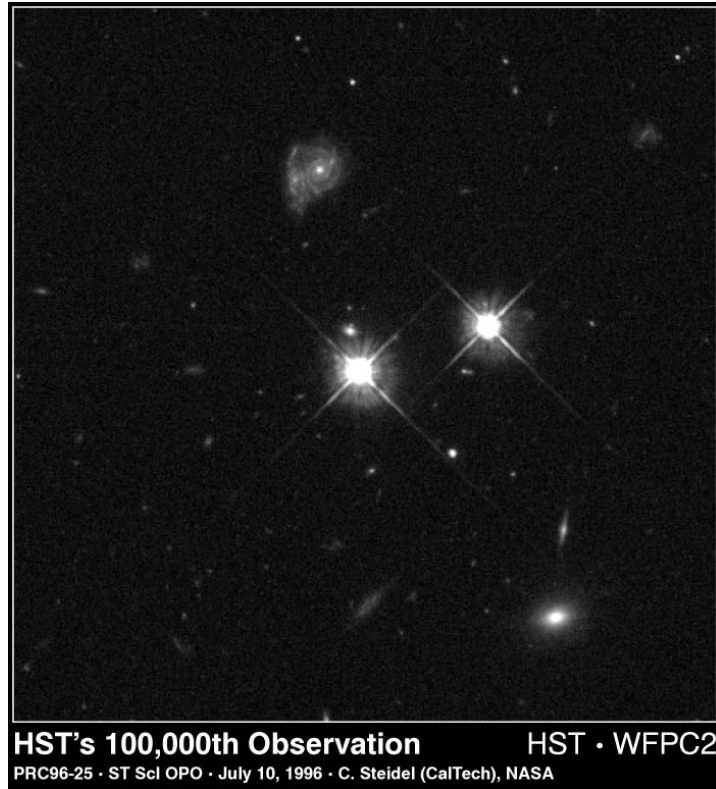
**Table 1.1:** Luminosity comparison of the most notable astrophysical sources. For each source we list its typical size, the physical process(es) powering them, their luminosity and lifetime. Despite being a composite of trillions of stars, giant galaxies are not the most energetic source. *Gamma-Ray Bursts* have the highest peak luminosity, but are powered by extremely short-lived explosive events. Manifestations of *Active Galactic Nuclei* (AGNs) such as *Quasars* are the *sustained* sources with highest peak luminosities; besides being the one that emit most energy throughout their whole lifespan.

caused by the violent merging of a binary neutron star, though other classes of GRBs may be caused by core-collapse Super-/Hyper- Novae.

Manifestations of *Active Galactic Nuclei* (AGNs) such as *Quasars* are the *sustained* sources with highest peak luminosities, besides being by far the ones that emit most energy throughout their whole lifespan. Figure 1.2 shows a very famous picture of a quasar taken by the Hubble Space Telescope: the object (center-left), as far as 9 billions lightyears from Earth is seen as a point source as bright as a closeby star (center-right), and shines brighter than an elliptical galaxy visible in its close foreground. We will shortly discuss Quasar's observational features and what we know about their nature in Section 1.2, before getting along with this thesis' main topic, i.e. modeling the feedback of these record-worthy energy outputs on their host galaxies and halos.

There are yet two other general aspects worth mentioning before getting deeper in the topic. The first is related to the very nature of the AGNs. We anticipate -it is indeed well-known, and beyond reasonable doubt- that the very cores of galactic nuclei are but SuperMassive Black Holes (SMBHs), millions to billions times more massive than our Sun. A Black Hole is -to make a long story short- a gravitationally collapsed region of spacetime, so dense it can even capture all the photons in its proximity. It takes a

**Figure 1.2:** This milestone picture, famous also for being Hubble Space Telescope's 100,000th exposure, shows a quasar (center), as far as 9 billions lightyears from Earth, seen as a point source as bright as a closeby star (center-right). The fainter dot just above it is an elliptical galaxy in the quasar's foreground, about 2 billions lightyears closer.



bit of irony to realize that the brightest event in the Universe is ultimately caused by the darkest possible object, and in its largest occurrence! Yet it is not strange at all: matter happening to be in SMBHs' proximities can store large amounts of gravitational potential energy. Just, it was not easy to unravel the working principles of the engine that converts this energy into electromagnetic radiation; indeed a few dark spots still exist in the theory.

The other fundamental aspect to be considered regards the improvement of our models for understanding the astrophysical phenomena. Together with new and always improving telescopes, we have had better mathematical and physical models to compare to the objects we were observing. Let us think to the evolution of the theory of gravity, or the developements of theoretical asterosismology, just to name a few. Astrophysics needs detailed and *complete* models: in astrophysics it is not possible, just for the scales of its subjects, to perform experiments in which all the conditions are preset; though we have really much to observe, we are forced to adopt an holistic approach.

More recently, we have also being building computers and very large computer clusters, developing meanwhile software applications that greatly improved the predicting power of our models. If the pure gravitational N-body problem has no general exact solution for  $N > 2$ , now we can easily run simulations with millions or billions of bodies, and also deal everyday with even more challenging problems such as three-dimensional fluid dynamics, such as in this present work; this is due not only to the power of modern computers, but also to the developement and software implementation of algorithms such as the *finite volume methods* (which make use of the *Riemann*

*problem*) and the *Smoothed Particle Hydrodynamics* schemes, to cite only some of the most broadly used.

Isn't it a shining light by itself?

### 1.1.1 Brightest, and fundamental

Krawczynski and Treister (2013) compiled a remarkably complete list of the salient motivations for the study of AGNs:

**AGN Taxonomy:** AGNs are among the brightest extragalactic sources and account for a large fraction of the electromagnetic energy output of the Universe, motivating their taxonomy and statistical characterization. The study of AGNs in the nearby Universe shows that the diversity of AGNs can be understood as resulting from observing a smaller number of basic AGN types from different viewing angles (see Section 1.2.1).

**Accretion Physics:** AGNs are powered by the accretion of magnetized plasma. Studies of AGN accretion flows complement studies of other accretion flows in astrophysics: accretion onto protostars and stars, accretion onto compact stellar remnants (neutron stars and stellar mass black holes), and the accretion that powers gamma-ray bursts. One goal of the studies of AGN accretion flows is to provide a physical explanation of the different types of AGNs and their states in terms of the nature of their accretion flows and environments (see Section 1.2.3).

**Role in Eco-Systems:** AGNs play an important role for galactic and galaxy cluster eco-systems, i.e. their mechanical and electromagnetic power contributes to the heating of the interstellar and intracluster medium, and thus influences the star formation of the host systems (main topic of this thesis).

**History through Cosmic Time:** Deep radio, IR, optical and X-ray observations of AGNs have provided us with a wealth of information about the cosmic history of the formation and growth of supermassive black holes and the evolution of AGNs. Related areas of research are to clarify the role of AGNs in re-ionizing the intergalactic medium, and to explain the correlation between black hole masses and the properties of the host galaxy observed in the local Universe.

**Fundamental Physics:** On the most fundamental level, AGNs allow us to test the theory of general relativity (GR). GR's no-hair theorem states that Kerr (and more generally Kerr-Newman) solutions are the only stationary, axially symmetric vacuum solutions of the Einstein equations with an event horizon. Testing if astrophysical black holes are Kerr black holes thus constitutes a powerful test of GR in the observationally poorly constrained strong-gravity regime Psaltis (2008).

**Astroparticle Physics:** AGNs are astroparticle physics laboratories. A few examples: The TeV  $\gamma$ -ray emission from AGNs tells us that they can accelerate particles to  $>$ TeV energies and AGNs might even be the sources of Ultra High Energy

Cosmic Rays. The studies of the broadband emission from AGNs allows us to perform time resolved studies of the particle acceleration processes. AGN observations can also be used to constrain Lorentz Invariance violations (e.g. Abdo et al., 2009), and to set upper and lower limits on extragalactic magnetic fields (see the discussion in Taylor et al. (2011); Broderick et al. (2012)).

**AGNs as Beacons at Cosmological Distances:** The emission from AGNs can be used to study the properties of objects, diffuse matter, and radiation fields that are located between us and the AGNs. High-resolution spectra of high-redshift, low-metallicity quasar absorption line systems have been used to constrain the relative abundance of the light elements produced during the epoch of the Big Bang Nucleosynthesis Fields and Sarkar (2006). Measurements of the Gunn-Peterson optical depths of high-redshift quasars constrain the re-ionization history of the intergalactic medium Fan et al. (2006). X-Ray Absorption lines constrain the abundance and properties of warm-hot intergalactic medium Yao et al. (2012). The study of the GeV and TeV  $\gamma$ -ray energy spectra of blazars can be used to constrain the energy spectrum of the infrared and optical Extragalactic Background Light Meyer et al. (2012).

## 1.2 AGNs and jets

### 1.2.1 The AGN unified model

Some of the gravitational energy of the material accreted by AGNs is converted into heat and electromagnetic radiation inside the accretion disk and is radiated away by the accretion disk. Some of the material processed through the accretion disk escapes the accretion system as collimated (jets) and uncollimated (winds) outflows. The event horizon of a non-rotating Schwarzschild black hole is two times the gravitational radius:

$$r_s = \frac{2GM_{\text{BH}}}{c^2} \approx 2.95 \left( \frac{M_{\text{BH}}}{M_{\odot}} \right) \text{ km} \approx 4.2 \left( \frac{M_{\text{BH}}}{10^6 M_{\odot}} \right) R_{\odot} \quad (1.1)$$

Approximately 10%-20% of AGNs are radio loud (radio to optical spectral index  $>0.35$ , see e.g. della Ceca et al. (1994); Kellermann et al. (1998)), and show bright extended radio features with sizes up to  $\sim 1$  Mpc ( $3.08 \times 10^{24}$  cm). The AGN phenomenon thus spans  $\sim 11$  orders of magnitudes in size scales; from another perspective, the energies emitted by the central engine are comparable to the binding energy of the host galactic halo:  $10^{58} - 10^{62}$  erg, for halos ranging from hosting just an isolated *Early Type Galaxy* (ETG) to large galactic clusters.

Having to figure out how objects spanning a similar range of spatial scales work is a very demanding task; especially in the numerical field. This is mostly true for AGNs because they host complex structure at intermediate scales, too! The relevant physical processes to look at change accordingly. Figure 1.3 is entrusted the task of presenting the reader all these different structures, according to the mostly accreted

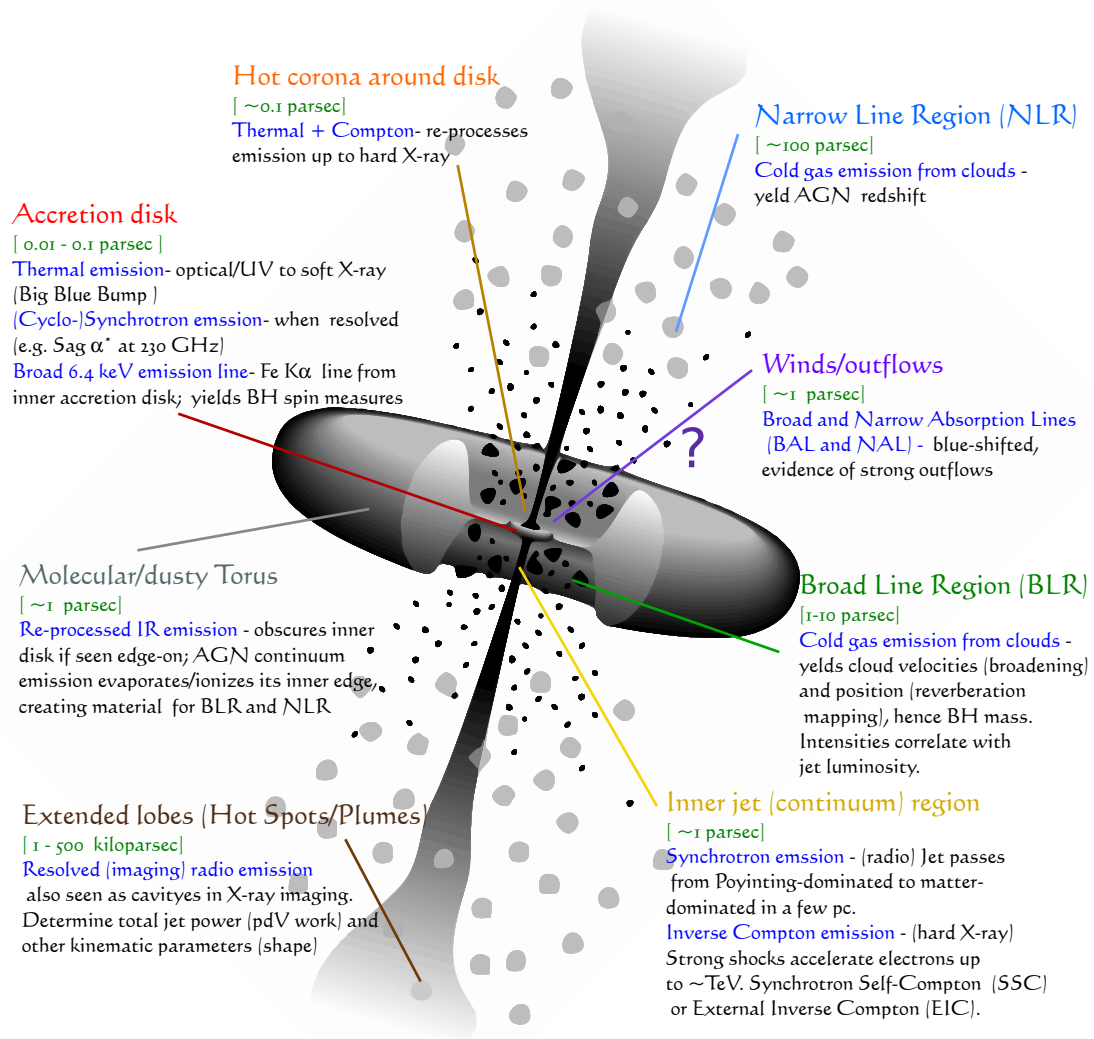


**Figure 1.3:** How the unified AGN model explains the spectral features of these objects. Note the multiscale structure, spanning several order of magnitudes in size (image not to scale). The color coding differentiates the structures; order-of-magnitude estimates of the structures' scale are indicated in light green; the spectral features (mostly emission) are highlighted in blue. Image adapted from: Astronomical Society of the Pacific (1995).

model. Next to each component, we list the main observational features it is believed to produce.

Now, in order to link all the components together, the model must explain (from Krawczynski and Treister (2013)):

1. how matter and magnetic fields are transported towards the accretion disks of the SMBHs;
2. which types of accretion disks occur in nature and how they work;
3. which physical mechanisms are responsible for accretion disk state transitions and flares;

4. how the individual emission components are produced,
5. how jets form, transform, accelerate and/or decelerate at different distances from the SMBHs;
6. how AGNs interact with their environment.

The first three of the above points are related to processes taking place in the accretion disk, and to how the disk interacts with the SMBH. A detailed exposition of these processes is beyond the scope of this thesis, which focuses mainly on the last point (feedback). Indeed, much numerical work has been recently done in this direction, though it focuses on scales -both temporal and spatial- much smaller than we do (see remarks in Section 3.1). In section 1.2.2 we will just give a brief account of the mostly trusted jet-launching mechanisms.

As anticipated, a great prediction of the model sketched in Figure 1.3, is to unify several -quite different- observed categories under a unique label, varying just a few AGN parameters and their inclination angle in the sky. This milestone result is summarized, better than many words could do, in Figure 1.4.

The first, true physical distinction is among *radio loud* and *radio quiet* quasars (i.e. with active jets or not); we are interested in modelling only the former category. Among this category, the next (and to large extent, last) physical aspect to consider is the morphologic *Fanaroff-Riley classification* (Fanaroff and Riley, 1974). This distinction, of which we will make large use in defining the jet parameters (e.g. Table 3.1), determines whether the radio jets have (FR II) or not (FR I) strong terminal shocks in the contact point with the surrounding gas. If present these features are called *Hot Spots* (HSs). In other words, a FR I radio galaxy is brightest in its central point, a FR II presents two brightness peaks at its edges; indeed, nowadays most sources are fully resolved, allowing us to distinguish the exact morphology. This morphologic classification is an important indicator of the jets' power and interaction with the environment: while the blasting (and more powerful) FR II jets can most often dominate the evolution of their host galaxy, they are a relatively rare occurrence.

### 1.2.2 Jet launching

Again, Krawczynski and Treister (2013) compile a remarkable review on jet-launching mechanisms.

The question of how matter and magnetic fields move towards the central engine (the feeding problem) does not have a simple answer as it depends on the cosmic epoch and the type and evolutionary state of the host (a single galaxy or a galaxy inside a galaxy cluster). The main challenge is to explain how the matter can shed all but a tiny fraction of its initial angular momentum while it goes through different phases and moves from  $\sim$ kpc distances to the accretion disk (e.g. Hopkins, 2012; McKinney et al., 2012). One of the open questions concerns the feeding of magnetic fields with a preferred polarity into the accretion flow, as such magnetic fields can suppress plasma instabilities in the disk, and can explain the presence of a strong single polarity magnetic field in the surrounding of the black hole, i.e. in the plunging region between the

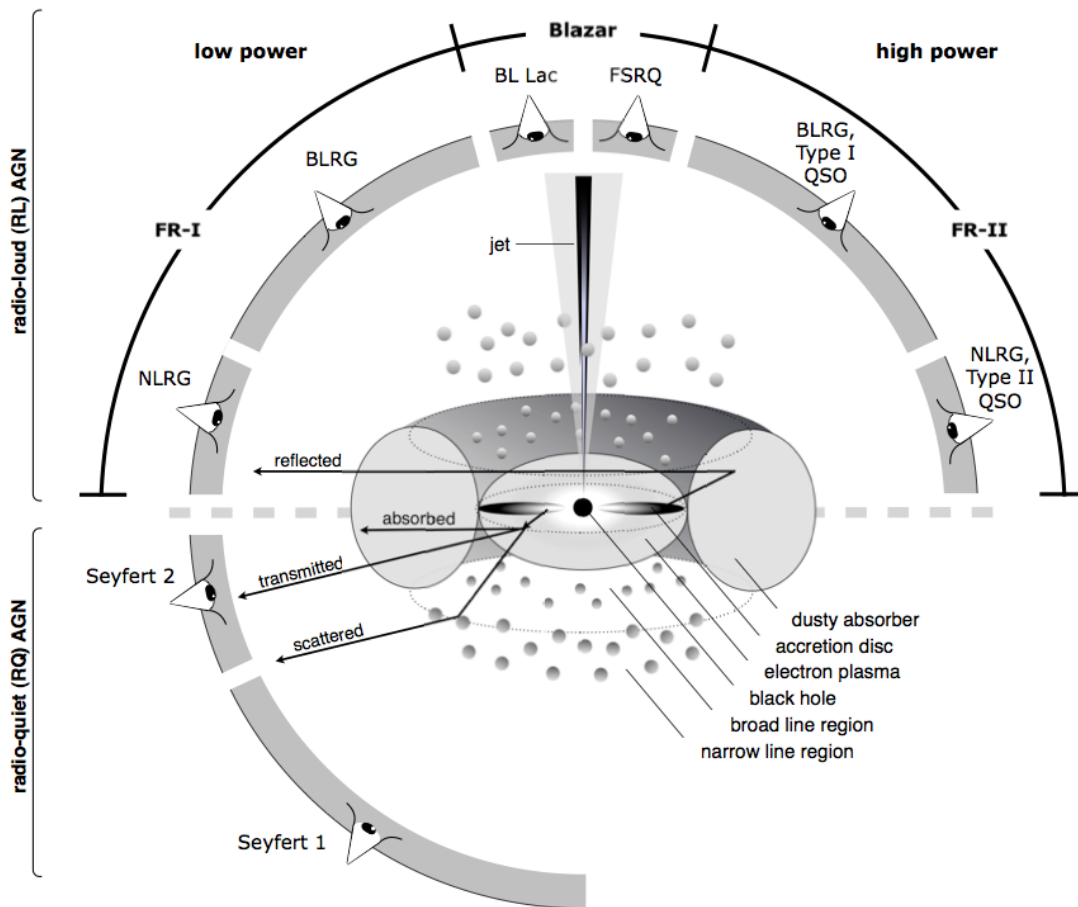


**Figure 1.4:** AGN unification scheme (image not to scale). It is possible to connect all the different AGN phenomenology in one picture; this AGN model explains all the observed classes accounting just for jet presence/absence (radio-loud or radio-quiet AGN), jet power, and the observer's inclination angle. Image credit: Beckmann and Shrader 2012

event horizon and the innermost circular stable orbit (ISCO). Such magnetic fields are required in some models of accretion and jet formation.

Accretion disks transform gravitational energy of matter into electromagnetic and mechanical energy. Shakura & Sunyaev (1973) introduced a model for a geometrically thin (with a thickness  $H$  at radius  $r$  such that  $H(r)/r \ll 1$ ), optically thick accretion disk Shakura and Sunyaev (1973). Assuming that the disk matter orbits the black hole on circular geodesics, that there is no torque at the ISCO, that the disk radiates away all the dissipated energy, and that no heat is transported in radial direction, the radial structure of the disk is entirely determined by mass, energy, and angular momentum conservation Shakura and Sunyaev (1973); Page and Thorne (1974). Using a prescription for the viscosity of the disk, the horizontal disk structure can be inferred. Although it was suspected that magnetic turbulence caused by the differential rotation of the accretion disk material was responsible for the viscosity, it was only in 1991 that Balbus & Hawley identified the magneto-rotational instability (MRI) as the driving instability based on numerical simulations Balbus and Hawley (1991).

A number of authors discuss alternative accretion flows. Ichimaru (1977) describes a two-state model to explain two qualitatively different emission states of the X-ray binary Cygnus X-1 (Ichimaru 1977). Whereas the high-soft state corresponds to the geometrically thin, optically thick radiatively efficient accretion disk of Shakura & Sunyaev, the low-hard state corresponds to a geometrically thick, optically thin radiatively inefficient accretion flow (RIAF). In the latter case, a thermal instability of the disk plasma develops when dissipative heating exceeds the radiative cooling causing the disk to puff up. Narayan et al. (1994) discusses a self-similar geometrically thick RIAF flow, the advection dominated accretion flows (ADAFs), in which the gas orbits the black hole with a velocity well below that of Keplerian orbits (Narayan and Yi 1994). The authors remark that such flows can form for low accretion rates when the flow is optically thin, or for very high accretion rates when the flow is optically thick and the cooling time of the plasma is much longer than the accretion rate. Variations of ADAFs include convection-dominated accretion flows (CDAFs) (Di Matteo et al. (2000); Quataert and Gruzinov (2000)), and advection-dominated inflow-outflow solutions (ADIOSs) (Blandford and Begelman (1999); Begelman (2012)).

The jet is probably launched by the combined effect of thermal pressure, centrifugal forces, and the Blandford-Znajek process. The latter involves the conversion of the rotational energy of a black hole spinning in the magnetic field anchored in the accretion disk into electromagnetic energy (Blandford and Znajek (1977)). In the presence of a favorably shaped outflow channel (formed by a geometrically thick accretion disk or by a less collimated wind), the flow can accelerate owing to magnetic pressure gradients. Energy conservation dictates that the terminal Lorentz factor of the jet obeys  $\Gamma_j^\infty < \sigma_0$  with  $\sigma_0$  being the magnetization (ratio of electromagnetic to particle energy densities) at the base of the jet, so that  $\sigma \gg 1$  is required to explain  $\Gamma_j^\infty \gg 1$ .

We would like to know which accretion flows occur in nature, which flow properties lead to the observed phenomenology, and how the observed jets form. Attempts in this direction include the identification of the radio quietness and loudness (the absence or presence of a jet) with geometrically thin and geometrically thick accretion flows, respectively. Some authors explain the difference between BL Lacs and FSRQs by invoking radiatively inefficient (with weak BLR emission) accretion flows for the former and radiatively efficient (strong BLR emission) accretion flows for the latter sources. Unfortunately, none of these associations is firm at the time of writing.

Recently it has become possible to employ 2D and 3D general relativistic magnetohydrodynamic (GRMHD) simulations with sufficient resolution to test some of the assumptions underlying the analytical and semi-analytical models. Most simulations neglect radiative transfer of heat owing to computational limitations. Such simulations have been used, for example, to test the assumption of zero torque at the ISCO (and zero energy dissipation of the disk plasma within the ISCO). The results indicate that the zero-torque approximation introduces rather small errors, i.e. it underestimates the emitted luminosity by  $\sim 5\%$  (Noble et al. (2011); Penna et al. (2012)). McKinney et al. (2012) studied rather thick ( $H/r \sim 0.3$ ) accretion flows with large-scale dipole and quadrupole magnetic fields and obtained two interesting results: (i) the structure of the accreted magnetic field is decisive for the formation of a collimated relativistic outflow; an accretion disk with a dipole magnetic field geometry does pro-

duce a jet, but disks fed by plasma without an ordered magnetic field or with higher moment magnetic field geometries do not (see also: McKinney and Narayan, 2007; Beckwith et al., 2008); (ii) somewhat unexpectedly, the jets are stable even though the toroidal component of the magnetic field that accelerates the jets could disrupt the flow owing to helical kink and screw modes. Several effects – including gradual shear, stabilizing sheaths, or sideways expansion – may be responsible for stabilizing the outflow.

As ordered magnetic fields are needed for the production of jets, McKinney et al. (2012) employ 3D GRMHD simulations to study a geometrically thick flow supplied with strongly magnetized plasma. They find that for rapidly spinning black holes toroidal magnetic fields can lead to large patches of single-polarity poloidal magnetic fields threading the black hole enabling the transformation of rotational energy of the black hole into Poynting flux energy. Strong poloidal magnetic fields build up in the inner region of the disk and compress it into a geometrically thin accretion flow in which the strong poloidal magnetic field suppresses the MRI. As mentioned above, further studies are needed to understand which accretion flows are actually realized in nature.

### 1.2.3 Comparison of astrophysical jets

Earlier we had highlighted that studies of different types of astrophysical jets can complement each other. AGN jets are the most powerful and best resolved; on the other end, jets from Low Mass X-ray binary stars (LMXBs), having typical durations of order a few months or weeks, can teach us more about jet dusty cycles (if one manages to target them fast enough!). Young Stellar Objects (YSOs) and the already mentioned Gamma-ray Bursts (GRBs) are also traditionally associated with jets. Other classes of jets exists, too. For instance, X-ray binaries give sometimes rise to radio-loud object, the so-called *radio X-ray binaries* or *microquasars*, which show -on smaller scales- many kinematic analogies with their larger relatives quasars.

Remarkably, a jet may be formed just in the presence of a central mass fed by an accretion disk<sup>1</sup>. If the central mass is not a black hole, or at least a very compact object, the conditions for the aforementioned Blandford-Znajek (BZ) process, in which the jet is powered taking energy from the spin the black hole, are no longer verified. But it is possible for jets to be launched directly by the disk magneto-rotational energy, as shown by Blandford and Payne (1982). One immediate consequence of this, is that jet launched via this process would have a much heavier composition (i.e. contain more adronic matter) than the (initially) Poynting flux-dominated BZ jets, leading to a qualitatively different evolution, at least in the early phases. This has indeed be detected in a few Xray binary sources (Díaz Trigo et al., 2013). In fact, even though acceleration and collimation mechanisms are similar, it is true that different jets are observable because of different processes .

Table 1.2 presents a very informative comparison of all objects classically associ-

<sup>1</sup>It is actually under debate whether jets can be originated without accretion disks, for instance by weak recollimations shocks from initially broader outflows, though for AGNs this appears out of doubt.

Object	Central Mass $M_{\odot}$	Powered by	Jet velocity (or Lorentz $\gamma$ )	Timescale years
Young Stellar Objects	$0.08 - 8^a$	Accreting young star	100 – 350 km/s	$10^5 - 10^6^b$
AGNs	$10^6 - 10^{10}$	Accreting SMBH	$\gamma = 3 - 10$	$10^6 - 10^8$
Long Gamma Ray Burst <sup>c</sup>	8 – 40	Accreting BH or-core collapse SN	$\gamma \simeq 300$	$\gtrsim 10^{-6}$
Massive X-ray binaries	5 – 10	Compact object accreting from companion's <i>winds</i>	0.26 c	$10^{-3} - 10^0$
Low mass X-ray binaries	2 – 5	Compact object accreting from companion's <i>shell</i>	0.1 c	$10^{-3} - 10^0$

<sup>a</sup>Lower limit: a brown dwarf's mass

<sup>b</sup>Stages in which YSOs have optically thick disks

<sup>c</sup>Jet presence very likely but not directly verified

**Table 1.2:** Comparison of classical astrophysical jets, listing central mass, accretion process powering the jets, outflow velocity and typical timescales (object variability/duty-cycle).

ated with astrophysical jets. While central mass and typical timescale/variability span several orders of magnitude, Livio (2004) notes how virtually all the time the outflow velocity  $v_{jet}$  is roughly equal to the escape velocity from the central object, concluding that the jets are launched from the innermost accretion region. A launching process ruled by magneto-centrifugal acceleration in an accretion disk (such as both BZ and BP), would indeed behave accordingly: the magnetic energy of the inner disk region could grow almost indefinitely until a jet can escape; in the case of AGNs, this process can safely be defined the most powerful engine of the Universe.

## 1.3 AGN Feedback

### 1.3.1 The inefficient star formation and the overcooling problem

The large energies AGNs are capable of emitting (comparable in some cases to the total binding energy of a galactic halo), urges us to include them in our models of galaxy formation and evolution. If these considerations were not enough, we see examples of galaxies dominated by radio jets, such as the very bright jets of Hercules A (Figure 1.5), that observed in optical looks just like a pretty regular isolated elliptical galaxy, even though a very large one. Objects like it (very powerful Fanaroff-Riley II radio-galaxies) are in fact quite extreme, but their study can be very instructive.

What's more, our models seem to lack mechanisms of gas heating on the high-mass

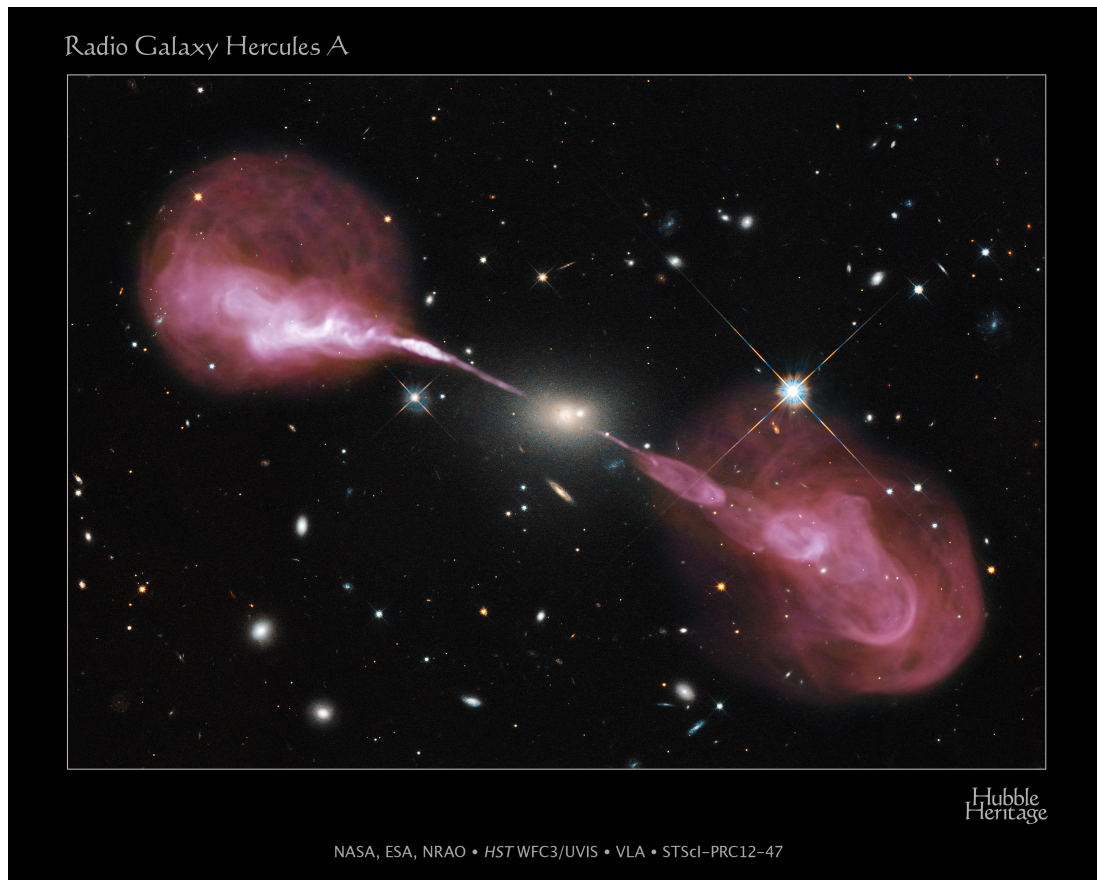


**Figure 1.5:** Multiwavelength view of the Hercules A galaxy, one of the brightest example of radio jets.

end. Figure 1.6 shows the relation between the stellar mass (from galaxy luminosity) and total halo mass ( $M_h$ ). The observational data have been derived by Moster et al. (2010) by the *abundance matching* technique, i.e. ranking masses (from cosmological simulations) and luminosities (observed), and pairing them in the same order.

At the time of writing, more recent versions of the relation exist, obtained with more refined techniques and also incorporating newer data, but the main point we want to stress persists, as it does all the way to  $z = 0$ .

That figure features a comparison between the relation and hydrodynamic simulations of galaxy formation (a cosmological volume by Kannan et al., 2014, from which the plot is borrowed). Each point is an individual simulated galaxy. At the low-mass end of the relation, the simulations are able to reproduce the stellar masses reasonably well. This success has been achieved by proper implementation of baryon feedback, mainly feedback from supernovae and heating by stellar radiation (e.g. Stinson et al., 2013). Yet, the simulations largely overestimate the stellar content for  $M_h \gtrsim 10^{12} M_\odot$ . This means that clearly some physics operating in large galactic halos has not been properly understood or modelled. Generally speaking, feedback from stars or supernovae works by blowing gas away, so in large galactic halos it cannot be as effective, since the deeper potential well does not let the gas escape.

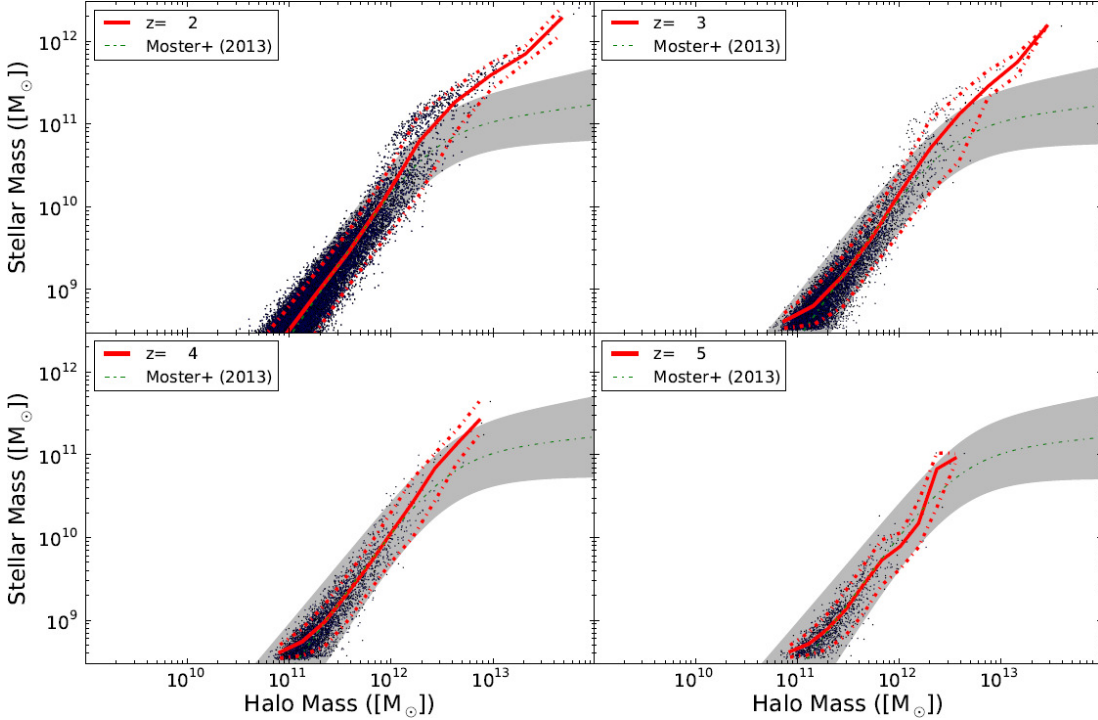


**Figure 1.6:** Evolution of the stellar-halo mass relation. The green line is the expected relation between the total (gas + dark matter + stars) halo mass and the stellar mass, obtained by *abundance matching* techniques by Moster et al. (2010), with scatter. The dots represent individual galaxies from a cosmological volume simulation ( $16 h^{-1}$  Mpc) by Kannan et al. 2014. The red lines mark the median of the simulation points and their 10th and 90th percentile. One can see how galaxy with halo mass  $M_h > 10^{12} M_\odot$  have a much larger stellar mass than expected. This exemplifies the *overcooling* problem our models undergo, suggesting that we are missing important physics. Credit: Kannan et al. 2014.

On cluster scales, this results in much more cold gas ( $10 - 100 M_\odot / yr$ ) flowing into the halo center (*cooling flow problem*), cooling further by emitting brehmsstrahlung radiation. This of course affects the halo center for several kpc, resulting in unrealistic entropy profiles (Babul et al., 2002).

In general, gas cools very efficiently at the center of dark matter halos, thus forming galaxies with too high stellar masses (cooling and star formation are processes always included in the simulations). This is referred to as *the overcooling problem*. Sometimes it is also called *catastrophic cooling*, since it is a runaway process: gas cools, losing pressure support; thus it sinks and collects onto the halo center, where its density grows, cooling even more efficiently.

In order to improve our models, we might need a better implementation of radiative cooling, or a better coupling with radiation (for instance, simulations including *radiative transfer*). But it is true that feedback from AGNs has to be operating in those mass regimes, and potentially AGNs contain enough energy to prevent the triggering of catastrophic cooling (Babul et al., 2002; McCarthy et al., 2008), and reconcile observed and predicted stellar contents at the high-mass end (e.g. Croton et al., 2006).

### 1.3.2 AGN feedback in models of galaxy formation

Since the paper by Silk and Rees (1998), the importance of AGN jet feedback received strong support from both theoretical (e.g. Sutherland and Bicknell, 2007; Gaibler et al., 2012) and observational (e.g. Schawinski et al., 2006; Elbaz et al., 2009) perspectives. Yet for theorists dealing with AGN feedback is quite complex, because several different outflow mechanisms have been observed/proposed to possibly originate from an AGN, mostly determined by the rate of the mass inflow onto the SMBH (Section 1.2.2). It is possible to distinguish (see e.g. Fanidakis et al., 2012): a *quasar* (radiative) mode powered by a high accretion rate; a *jet* (or *kinetic* or *radio*) mode, when having a lower one. Radio mode feedback is required to shut down star formation (SF) at low redshift and prevent cooling flows from forming (negative feedback: Croton et al., 2006, Somerville et al., 2008b, Tortora et al., 2009, Fabian, 2012). The jet mode might be the only mechanism active for long enough to have significant impact on galactic SF. As an additional complication, AGNs are sometimes reported to have the opposite effect (*Positive feedback*, see e.g. Gaibler et al., 2012).

Even if theorists have to deal with all these ambiguities -and are often urged to simplify-, feedback from Active Galactic Nuclei is now a crucial ingredient in theoretical models and simulations of galaxy formation and evolution; we will briefly mention only some of the most recent studies.

As for semi-analytical models, for instance, Somerville et al. (2008b) showed how it can affect the properties of galaxies and their surrounding gas, while Fanidakis et al. (2012) found this kind of feedback necessary to reproduce the observed AGN luminosity functions.

The consequences of AGN feedback are now being investigated by several numerical groups, by introducing sub-grid<sup>2</sup> models of AGN feedback directly in galaxy formation simulations.

Schaye et al. (2014) adopt a particle simulation scheme (the GADGET3 code), integrating AGN feedback without needing to modify the radiative cooling prescriptions, aided in this by their high resolution. In Vogelsberger et al. (2014), an AGN feedback implementation is added to a self-consistent galaxy formation scenario in the moving-mesh code AREPO. They account for both radio and quasar mode -as from Sijacki et al. 2007a. Although the feedback prescriptions (*Super Novae* + AGNs) in these examples can often quench galactic star formation down to the observed values, the authors point out how careful calibration is required; the risk of fine-tuning and overestimating the feedback efficiency is very high.

Dubois et al. (2014b,a) use the grid code RAMSES to follow galaxy-Black Hole relationships through cosmic history, stressing that AGN feedback also affects the morphology of galaxies, and can regulate post-merger gas inflows.

Though we are ultimately interested in the effects on galaxy formation, in this thesis we adopt a different approach. Rather than testing “ad hoc” subgrid models, we focus on highly resolved hydrodynamic simulations of the interaction of *individual* jets with

<sup>2</sup>The scales on which AGN feedback operates are very rarely well resolved.

the interstellar and circumgalactic medium (ISM and CGM) of their host galaxy.

Simulations of direct jet/gas interaction produced a vast literature, recently featuring a full tridimensional approach. Some of these works will be described in Section 3.1. Most studies focus either on galaxy-cluster scale (e.g. Morsony et al., 2013), or on galactic environment but for short timescales (e.g. Gaibler et al., 2012; Perucho et al., 2014a). On the other hand, galaxy formation models predict AGN feedback to be at work already for Milky Way-size galaxies (Fanidakis et al., 2013) and for cosmological timescales (Somerville et al., 2008b), as also in those regimes the overcooling problem is present (Section 1.3.1).

We are mostly interested in modeling jet feedback in individual galaxies.

---

## Jets with the FLASH Code

---

Jets from AGNs involve complex physics, but it is possible to deal with them as essentially a fluid dynamics problem. Especially if we want to investigate the effects of the mechanical thrust of AGNs on their host halo (including heating from shocks, the effect of turbulences, gas circulation) and the thermodynamic state of such systems<sup>1</sup>.

A non-linear problem, as every one in hydrodynamics. Still its astrophysical basis is rather complex, considering the multi-scale nature of AGNs (Section 1.2) and the nonlinear nature of shocks and turbulence. Moreover, we mentioned in Section 1.1 how in astrophysics we are often forced to take the holistic approach, and include all the physical processes that could be at work. Usually, which thing is especially true in numerical simulations, this requires good planning and expertise in understanding what must be included and what can be dropped, as long as not enough resources are available.

In this case, *radiative cooling* must be considered (the main reason for the investigation of AGN feedback is to stop galactic halos from excessive cooling). Also *gravity* has to be present: the buoyant forces on the hot gas largely contribute to shape the radio sources (Chapter 4). The bulk of the gravitational potential is generated by the dark matter density, but the self-gravity of the gas has to be included, too -except maybe for the earliest stages (as in Chapter 3). Coupling with stellar feedback would be also very important on long terms, so much work has been done in this direction (see Chapter 5).

The bad news is that each additional bit of physics added to the model, comes with its own (space and time!) resolution requirements, which are sometimes more strict than the hydrodynamic ones, thus adding significant computational load.

---

<sup>1</sup>In principle, there could be more physics that ordinary hydrodynamics could not grasp correctly: radiation, magnetic fields, high-energy particles. Yet, on galactic halo scales, the contribution of these physical processes should not really be determinant.

The good news is that we are still left with an hydrodynamical problem: it was possible -with relatively minor modifications to our source code- to include these effects in the main engine, though this required extensive coding and testing.

## 2.1 Introduction to Computational Fluid Dynamics and FLASH

We use FLASH (see Fryxell et al., 2000), version 4.0. In this section, we will go through the fundamental elements of *computational fluid dynamics* (CFD), with particular attention on how each issue is implemented in FLASH. Of course, an exhaustive exposition of fluid dynamics (or CFD) is beyond the aim of this document.

First, a few introductory words on FLASH: FLASH is

a publicly available multiphysics multiscale simulation code with a wide international user base. Research projects include high-energy density physics, thermonuclear-powered supernovae, exascale computing co-design, fluid-structure interactions, and development of implicit solvers for "stiff" systems. (FLASH homepage)

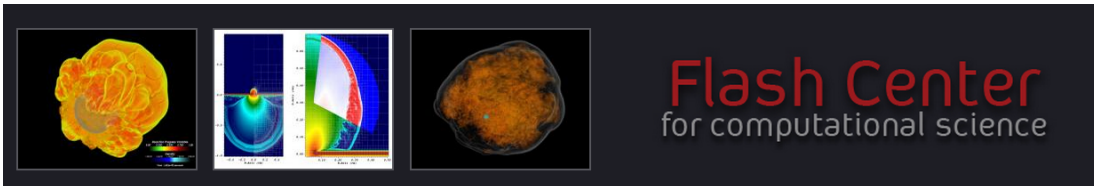


**Figure 2.1:** FLASH's homepage headline - <http://flash.uchicago.edu/site/index.shtml>.

Most importantly, FLASH makes use of the Adaptive Mesh Refinement (AMR) scheme. This concept will be explained in detail in Section 2.2. Briefly, in AMR the simulation domain is discretized in a mesh that is not uniform nor static, but is capable of getting coarser or finer according to the resolution needed in each particular region. This happens automatically during each simulation run -following the user's directives- and allows efficiently to deal with multi-scale problems, in which in different regions there is structure that needs to be resolved on different scales. AMR in FLASH is a complex data structure, that allows to reach high resolution where needed, while saving computational power, memory and disk space in the other parts of the domain. Just what our problem needed.

AMR allows us to resolve 150 pc over a simulation box side of order Mpc (though exact box size and resolution are specified exactly case by case in the following chapters) in a fully three-dimensional case. Figure 2.2 shows an example of an AMR mesh in one of our jet simulations; one can see how the grid assumes a different *refinement level* on different structure.

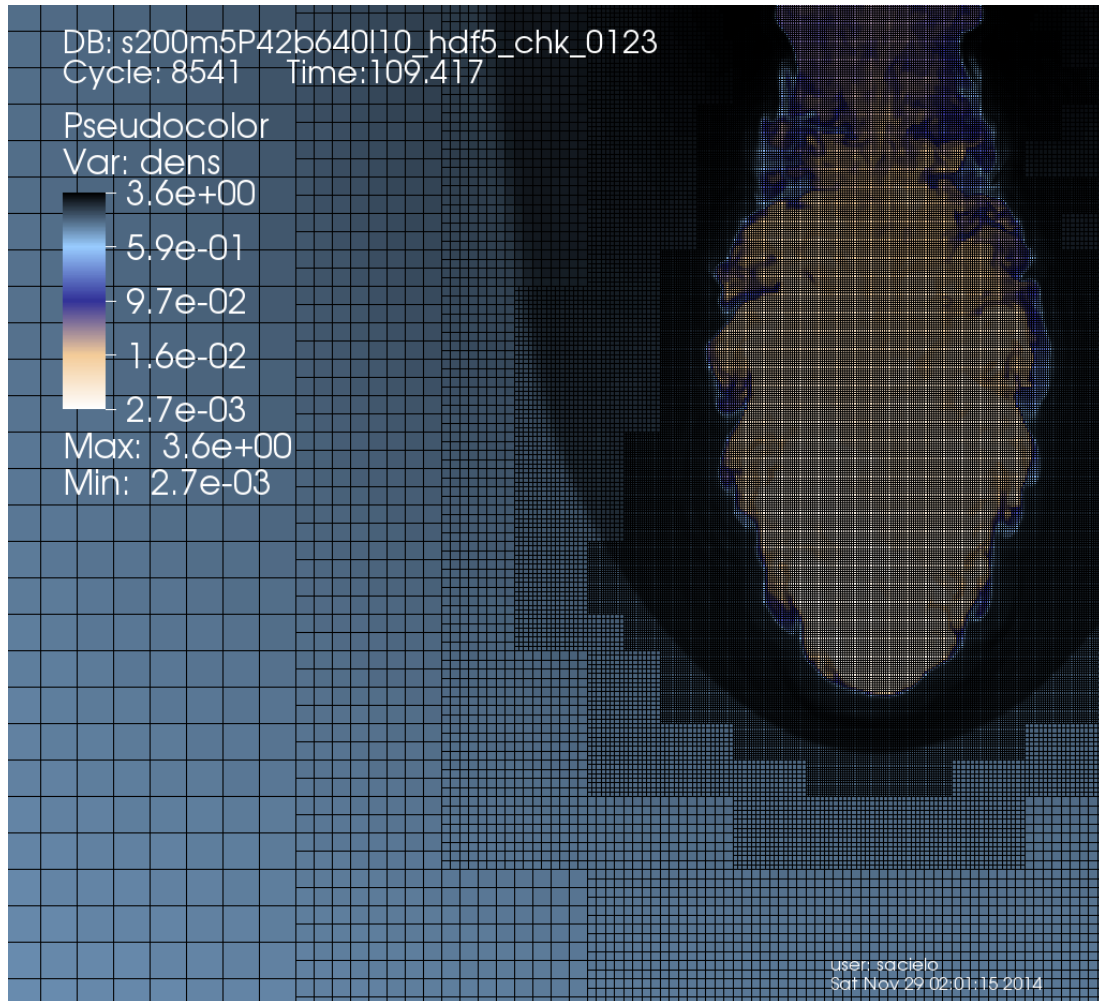


**Figure 2.2:** AMR mesh in one of our jet simulations; one can see how the grid assumes a different *refinement level* on different structure. This picture shows a central slice of the 3D simulation volume; the color code is according to the gas density. The simulation is set so that the refinement level is higher where the density changes (gradients) are higher; the same is true for the gas temperature; the refinement is highest on the turbulent hot bubble, degrading towards outside.

FLASH is written mostly in Fortran90 language, and features a fully modular structure, in which several *Units* are chosen by the user and linked together to produce an executable for the problem under investigation.

FLASH, as virtually all modern simulation softwares, is massively parallel, i.e. designed for working on large multi-core machines. It uses the Message-Passing Interface (MPI) library for inter-processor communication and the HDF5 or Parallel-NetCDF library for parallel I/O to achieve portability and scalability on a variety of different parallel computers.

In Section 2.3, after a review of the general CFD concepts, we will describe all the main FLASH units in detail.

### 2.1.1 The Navier-Stokes equations

At the beginning of this chapter, we said that we will be dealing with jets as a fluid dynamics problem. The natural way of solving a fluid problem is to make use of an *eulerian approach* which leads to the *Navier-Stokes equations*. The solutions of these equations yield the values of the velocity (and density, and pressure) fields, in eulerian fashion indeed<sup>2</sup>.

The Navier-Stokes equations are a form of *continuity equation*, which can be seen as expressing a mechanical *conservation law*, but for a *continuum fluid*. In differential form this is simply:

$$\frac{\partial Q}{\partial t} + \nabla \cdot (Q\mathbf{v}) = S \quad (2.1)$$

which states that, for any point in space, the change rate of an intensive quantity  $Q$  (scalar or vector) plus the divergence of  $Q\mathbf{v}$  equals the local source term  $S$ . Taking  $Q$  to be the fluid density  $\rho$  and its momentum  $\mathbf{p} = \rho\mathbf{v}$  gives:

(Navier-Stokes)

$$\frac{\partial \rho}{\partial t} + \nabla \cdot (\rho\mathbf{v}) = 0, \quad (2.2a)$$

$$\rho \left( \frac{\partial \mathbf{v}}{\partial t} + \mathbf{v} \nabla \cdot \mathbf{v} \right) = -\nabla p + \nabla \cdot \sigma + \mathbf{f}, \quad (2.2b)$$

where we have calculated a few derivatives and explicitated the source functions. The source function for the mass continuity equation is here set to zero<sup>3</sup>, while for the momentum equation the source terms are effectively force densities: the (negative) gradient of the fluid pressure  $p$ , plus the (tensor) divergence of the stress tensor  $\sigma$ , plus all external force densities, included in the  $\mathbf{f}$  term. For instance, gravity will contribute with a  $-\rho \nabla \Phi$  term,  $\Phi$  being the expression of the gravitational potential. In our case, the density will include both gas and dark-matter density. If viscosity is not present (i.e.  $\sigma$  is a diagonal tensor) the equations are named the *Euler's equations* (their first derivation being due to Leonard Euler). Let us write them down, in the actual form FLASH solves them:

(Euler)

$$\frac{\partial \rho}{\partial t} + \nabla \cdot (\rho\mathbf{v}) = 0 \quad (2.3a)$$

$$\frac{\partial \rho\mathbf{v}}{\partial t} + \nabla \cdot (\rho\mathbf{v}\mathbf{v}) + \nabla p = \rho\mathbf{g} \quad (2.3b)$$

$$\frac{\partial \rho E}{\partial t} + \nabla \cdot [(\rho E + p)\mathbf{v}] = \rho\mathbf{v} \cdot \mathbf{g}, \quad (2.3c)$$

where the equation for the higher momentum, the energy  $E$ , has been added, and in the sources we consider only the gravitational acceleration  $\mathbf{g}$ .  $E$  is the total gas energy,

<sup>2</sup>Lagrangian approaches, focusing on positions, lead to particle-based methods. Although today these methods allow to deal with hydrodynamics -such as in the *smoothed particles hydrodynamics* (SPH)- they are not ideal for this problem for the above argumentation.

<sup>3</sup>This is not compulsory; for instance the jet injection pints will have it non-zero

sum of the thermal ( $\epsilon$ ) and kinetic components:

$$E = \epsilon + \frac{1}{2}|\mathbf{v}|^2. \quad (2.4)$$

### 2.1.2 Equation of State

One could continue deriving equations as in 2.2 for the higher-order momenta, but it is already possible to see the need for an *equation of state* (EOS, i.e. an expression relating  $\rho$  and  $p$ ) for closure, in order give a complete set of equations<sup>4</sup>. The formulation of the continuity equation 2.1 is very general, valid for instance in both the classical and relativistic regime, provided that one considers the correct expressions for velocities, fluxes and EOS.

FLASH, as well as many modern codes, allows a broad selection of EOSs. FLASH uses the method of Colella & Glaz (1985) to handle general equations of state. General equations of state contain 4 adiabatic indices (Chandrasekhar 1939), but the method of Colella & Glaz parameterizes the EOS and requires only two of the adiabatic indices. The first is necessary to calculate the adiabatic sound speed and is given by

$$\gamma_1 = \frac{\rho}{p} \frac{\partial p}{\partial \rho}. \quad (2.5)$$

The second relates the pressure to the energy and is given by

$$\gamma_4 = 1 + \frac{p}{\rho\epsilon}. \quad (2.6)$$

Throughout all our work, we used the gamma-law EOS, which models a simple ideal gas with a constant adiabatic index  $\gamma$ , because for an ideal gas, all adiabatic indices are equal. For comparison with some recent simulation work featuring a relativistic EOS (but in 2D) the reader may check Perucho et al. (2014b).

The relationship between density, pressure, and specific internal energy is

$$p = (\gamma - 1) \rho\epsilon. \quad (2.7)$$

We also have an expression relating pressure to the temperature

$$p = \frac{N_a k_B}{\bar{A}} \rho T, \quad (2.8)$$

where  $N_a$  is the Avogadro number,  $k_B$  is the Boltzmann constant, and  $\bar{A}$  is the average atomic mass, defined as

$$\frac{1}{\bar{A}} = \sum_i \frac{X_i}{A_i}, \quad (2.9)$$

---

<sup>4</sup>One would need some form of closure relation anyway, unless ALL the momenta are known.

where is the mass fraction of the  $i$ th element. Equating these expressions for pressure yields an expression for the specific internal energy as a function of temperature

$$\epsilon = \frac{1}{\gamma - 1} \frac{N_a k_B}{\bar{A}} T. \quad (2.10)$$

## 2.2 Discretization: Meshes and Adaptive Mesh Refinement

The Euler's equations 2.3 are partial-derivatives differential equations. In order to have computers solving them, the first step is to have them *discretized* in space and time, i.e. sampled on a discrete spatial domain and a set of discrete values of the time variable.

A warning is necessary here: in digital signal processing, discretization always comes together with *quantization*: the (floating point) numbers a computer uses to represent the values of the fields in play, belong themselves to a discrete set (each number being composed by a finite number of binary digits). This leads to unavoidable rounding or overflow errors. Today this is virtually never a problem for an ordinary computer, but programmers and users must know that this can happen: one must -for instance- adopt an adequate physical unit system (see Section 2.3) and stable algorithms when dealing with processes potentially instable problems (e.g. hydrodynamic turbulence or thermal instabilities).

Remarkably, the astronomical community possesses good know-how about discretization, since digital signal processing is now at the base of (practically) every professional telescope.

The finer the mesh, the better the *resolution* of the simulation; as a general rule, *Nyquist theorem* states that in order to resolve a phenomenon having a characteristic lengthscale  $\lambda$  in a discretized approach, the smallest sampling element should be  $\lambda/2$ . This is also true for the time variable.

A little disclaimer is maybe needed: in the following we will describe the discretization operation in just a qualitative fashion; further discussion would be a too long digression from this work's main topic. CFD is also a continuously evolving field, in which new schemes are frequently born; we want to cover mostly what FLASH uses. Although we do include a little broader overview on the generalities, our exposition will not cover all the methods used.

The reader familiar with (or not interested in) the basics of computational dynamics may prefer to skip to Section 2.3.

### 2.2.1 Discretization: the finite volumes method

There are several approaches to discretize differential equations. The *finite differences methods*, for instance, is a simple way to turn such equations in algebraic equations. In this case, one would sample the variables on the nodes of a finite grid, and approximate the partial derivatives with differences of the values in contiguous points.

Most CFD problems use instead the *finite volume* approach. In this case, instead of the nodes of a grid, one focuses more on the volume elements -the *cells*- in which the grid divides space. Quantities are summed or averaged on each cell's volume, while *divergence* terms in the equations of motions are integrated and converted into surface integral along the cells' edges (faces). So, one actually reasons in terms of *fluxes* through the cells' walls.

The finite volumes approach presents several advantages:

**Natural interpretation** - It is analogous to the differential line of reasoning between infinitesimal volume elements that leads to the derivation of the continuity equation 2.1 in the first place, just with finite size volumes. This makes it a method of natural and intuitive interpretation.

**Flux conservation** - The cells share their edges, so the flux that enters a cell from one direction must leave a neighbor cell (or a few of them) from the same face in the opposite direction. This is expressed by saying that the method is *conservative*. Again, this a very convenient way of working with continuity equations.

**Very general mesh requirements** - The method is suitable both for structured and unstructured meshes; for instance, having shifted the attention from derivatives to fluxes, it does not rely on a coordinate system as much as the finite differences method described above: it just needs a complete tassellation of space. In cartesian coordinates -as in this work- this is easily achieved. Curvilinear coordinate system (such as the polar coordinates) require a bit more care, but are perfectly manageable. Also unstructured space tassellations such as the one provided by the *Delauney triangulation* or *tetrahedral decomposition* are allowed, and broadly used<sup>5</sup>. The mesh may also move or change with time (as FLASH's AMR). Some codes make use of several of these features at once (e.g. the AREPO code, Springel, 2010).

**Resolution does not follow mass** - Broadly speaking, one downside of particle-based methods is that the *local* resolution is dictated by the number of particles in the area. This is not ideal, since the densest regions -the ones with the largest numbers of particles- are not always the ones that need to be resolved best. Finite volume grids allow much more control. As we sketched when presenting FLASH (Section 2.1) and we will specify later in this same section, in FLASH refinement is triggered by steep variable gradients (any variable of the problem can be chosen), such that the best resolutions are achieved at the edges of any detected structure.

Each method has its own downsides. Finite volumes methods, for instance, do not *automatically* conserve lagrangian quantities (e.g. angular momentum) in isolated systems as particle-based systems do, so additional care is required when computing fluxes. Also, if a mesh has a preferential orientation or shape, this might introduce numerical noise and impact the result. Finally, in the AMR case, the mesh complexity can sometimes grow very fast, especially if the structures to resolve expand. One should

<sup>5</sup>These meshes are also powerful tools in modern computer graphics

take care not to operate too much in a regime where large volumes are fully refined; if this happens, it may be better to switch back to something simpler as uniform grid.

### 2.2.2 Riemann solvers

After discretization, we are left with piecewise data, separated by discontinuities at the cell boundaries, whose equation of motion is in the form of a differential conservation law. This configuration, even outside the CFD context, is named *Riemann problem*. Analytical solutions to the Riemann problem involve *characteristic curves*<sup>6</sup> and present discontinuities. In classical fluid dynamics, such solutions are obtained by some combination of shock and rarefaction waves; but they can be written down explicitly. This is at the base of the approach used by most simulation software to solve the Euler equation 2.3. This portion of the software is called a *Riemann solver*. In three dimensions, *unsplit* Riemann solvers deal with the full cell networks at once, while *split* ones foliate first the domain along some coordinate axis<sup>7</sup>, considering layers or lines of cells all together, always reducing the problem to one dimension. The process is then repeated on each layer until the solution is found for each cell. On the following iterations, the process will alternate order of foliation among the different coordinates.

FLASH contains several Riemann solvers, implemented in the *Hydro* and *Driver* units (see Section 2.3). These solvers feature several improvements with respect to the simple procedure sketched above. An example among all: the Piecewise Parabolic Method (PPM) -that we broadly use in this work- assumes the data to be piecewise-constant and approximates them with parabolic functions. So, it is considering more than two cells at the time, and allows the introduction of several additional mechanisms (i.e. slope limiters) that control and eliminate possible unphysical waves. The PPM features second-order accuracy, and it is considered one of the most reliable methods.

### 2.2.3 Adaptive Mesh Refinement in FLASH

At this point, the core mechanism of the Adaptive Mesh Refinement is easy to explain. FLASH's default implementation of the AMR scheme is based on the *blocks* of the PARAMESH library. The domain is physically divided in blocks; several refinement levels coexist, so that the simulation domain is exactly *tassellated* by the coarsest block layer<sup>8</sup>. When necessary, a block is dichotomically splitted in each dimension, generating new blocks besides the existing ones. The blocks are logically organized in a tree-like scheme, in which sub-blocks have a *parent-daughter* relationship.

This choice has also the advantage that the *leaf blocks* (i.e. the blocks with no daughters) tassellate the full domain at the maximum resolution. So, for the analysis one can

<sup>6</sup>I.e. curves along whose coordinates the partial derivatives in the equations becomes ordinary derivatives

<sup>7</sup>This kind of split solvers need a structured grid such as in cartesian or polar coordinates.

<sup>8</sup>many schemes actually require the coarsest level to be made by a single block

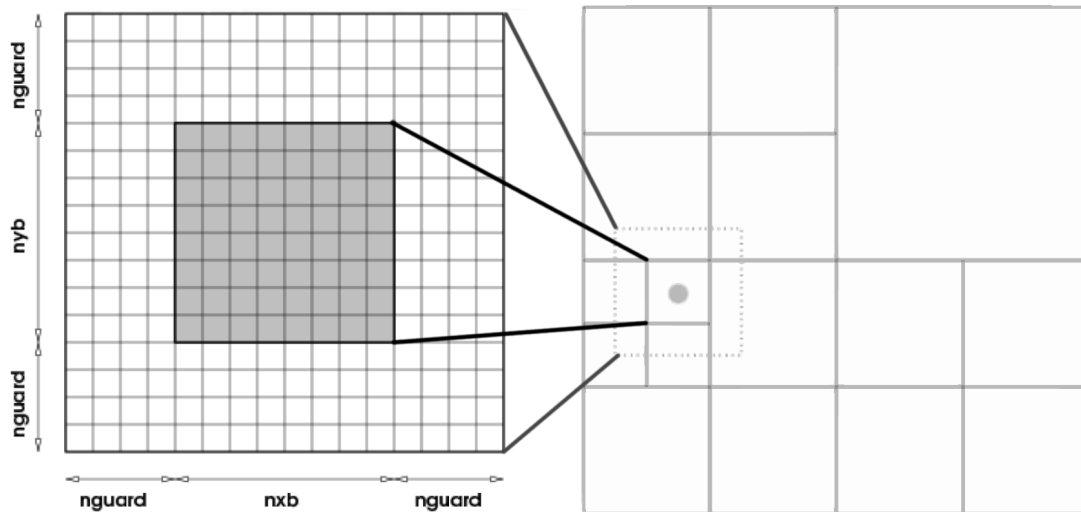


**Figure 2.3:** Right: A simple computational domain showing varying levels of refinement in a total of 16 blocks. The dotted lines outline the guard cells for the block marked with a circle. Left: zoom-in on a single 2-D block showing the interior cells (shaded) and the perimeter of guard cells. Adapted from FLASH user guide

just select them; this is an easy operation since FLASH labels leaf blocks with a specific flag.

Likewise, *derefinement* happens if higher resolution is no longer needed in a specific region. This is simply achieved by discarding the refined blocks.

The blocks are just the data structure taking care of the mesh refinement/derefinement. Each block is indeed divided in a specified number of cells, on which the actual computation is performed. We always used the default value of eight cells per block along each dimension (so, in 3D for each block we have  $8^3 = 512$  cells), but any number may be chosen. A perimeter of *guard cells* -of width *nguard* cells in each coordinate direction- surrounds each block of local data, providing it with data from the neighboring blocks or with boundary conditions (see Figure 2.3); this allows parallel domain decomposition among the different processors.

The refinement criterion used by PARAMESH is adapted from Löhner (1987). Löhner's error estimator was originally developed for finite element applications and has the advantage that it uses a mostly local calculation. Furthermore, the estimator is dimensionless and can be applied with complete generality to any of the field variables of the simulation or any combination of them. Löhner's estimator is a modified second derivative, normalized by the average of the gradient over one computational cell. The exact definition may be found in FLASH's userguide. In our setup, FLASH checks for both density and pressure estimators, triggering refinement if they are larger than 0.8, and de-refinement if they get smaller than 0.6.

For the sake of completeness, we mention that the block-based AMR described above is just one of the possible approaches. Another popular scheme is the *patch*-based AMR. In this case, there are no blocks to be dichotomically splitted, but rectangular patches of the desired refinement level are placed in the region to refine. Patches are somehow more flexible than blocks, allowing even for high jumps in refinement

levels among contiguous regions; but patches in general can overlap, sometimes making it difficult to reconstruct a domain tassellation with no repetition. The coming versions of FLASH will introduce patch-based AMR based on the CHOMBO library, currently under testing (the latest FLASH release at the time of writing is version 4.2.2).

### 2.3 Complete list of the FLASH Units

The following is a list of the main units in FLASH 4, each along with a very brief description.

Note that in most cases the Units implementations cannot be used just as they are, but must be -often heavily- edited by the user. Sometimes all is provided are empty placeholders (named *stubs* in the FLASH environment) that must be written entirely by the user, to form an organic setup. The work contained in this thesis comes from source code in large part originally written. Our active programming work is indicated in the list, highlighted by `frameboxes`.

**Driver Unit** controls the initialization and evolution of FLASH simulations. In addition, at the highest level, the Driver unit organizes the interaction between units. Initialization can be from scratch or from a stored *checkpoint file* produced by a previous simulation. The Driver Unit also determines the timestep of the simulation, in an adaptive fashion.

We have our jets launched by a subroutine within this unit. At initialization time, a small region around the injection point is refined to the maximum AMR level possible. Then, a few grid cells are treated as source terms for all the time the jets are on (having density, pressure and velocity set to the user specified value). The jet is thus launched *by hand*.

**Grid Unit** coordinates the Eulerian grid in which the simulation volume is discretized, and its eventual interaction with Particle Unit. It manages the AMR structure, in our case using the block-based PARAMESH library, in which refinement is achieved by recursive binary division.

**IO Unit** All output is in a very versatile custom version of HDF5 file.

The output files have a hierarchical structure that follows the PARAMESH blocks. For advanced scientific analysis, low-level control on the data is required. Much care has been spent in the development of an analysis pipeline, allowing the users to take advantage of the hierarchical data format. This has been achieved by the use of the Matlab and VisIt softwares.

**Runtime Parameters Unit** stores and maintains a global linked lists of runtime parameters that are used during program execution.

**Multispecies Unit** handles setting, querying, and operating on the properties of fluids, in case it is requested to follow multiple fluid species (e.g. for calculations involving nuclear reactions networks).

**Physical Constants Unit** provides a set of common constants, such as the gravitational constant, in various systems of measurement units. The default system of units is CGS, so named for having a length unit in centimeters, a mass unit in grams, and a time unit in seconds.

The default choice of the CGS system conflicts strongly with astronomical units. Having a typical simulation box of half a Megaparsec, and typical gas densities around one particle per cubic centimeter, working in CGS would mean to operate with exponents of order  $\pm 20$ . This is definitely not advisable in single precision numbers, and indeed early tests show significant numerical rounding errors (Section 2.2), especially when evaluating radiative cooling terms (see the Local Source Terms Units below), which are proportional to the square of the gas density. The best solution to this problem is to adopt a different unit system, in order to deal with numbers as close to the unit as possible, where floating point numbers perform best. We have then introduced a unit system initially unknown to FLASH: the cosmology-friendly FLY system (Antonuccio-Delogu et al., 2003). In this system, the unit length  $L_0$ , time  $t_0$  and mass  $M_0$  are chosen to be, respectively

$$L_0 = 1 \text{ Mpc } h^{-1} = 3.08568 \times 10^{25} h^{-1} \text{ cm}; \quad (2.11)$$

$$t_0 = \frac{2}{3} H_0 = 2.05759 \times 10^{17} h^{-1} \text{ s}; \quad (2.12)$$

$$M_0 = 5.22904 \times 10^{12} h^{-1} M_{\odot}. \quad (2.13)$$

$h$  being the reduced *Hubble constant* of cosmology (set to 0.7 in our case). To change the unit system, one starts we had to change manually the values of the physical constants stored in this Unit, but fixing of inconsistencies throughout all the FLASH filesystem (and long testing) was necessary.

**Hydrodynamics Unit** solves Euler's equations for compressible gas dynamics in one, two, or three spatial dimensions (see Section 2.1.1). Among the several hydrodynamic solvers we make use of the Pfft (standing for Parallel fast fourier transform) in Chapter 3 and the PPM (Piecewise parabolic method) in Chapter 4.

**Equation of State Unit** implements the equation of state needed by the hydrodynamics and nuclear burning solvers (see Section 2.1.2).

**Local Source Terms Units** contains several units that implement forcing terms. The Burn, Stir, Ionize, and Diffuse units contain implementations in FLASH4. Two other units, Cool and Heat, contain only stub level routines.

Radiative cooling had to be added, just a stub being provided. Now our setup can read cooling table by Sutherland (1993) for all the gas metallicity range they provide. This implementation works for the gas temperature in the range  $[10^{4.5}, 10^8]$  K; for higher gas temperature a pure Bremsstrahlung term was added. Again, the FLY unit system helped avoiding numerical rounding errors. It was also necessary to add an explicit calculation of the cooling timestep (according to Field, 1965), so that simulations can slow down (i.e. reduce the running timesteps) if necessary to resolve cooling, in particular during possible *thermal instability* events. A similar work could be done in the near future to include ultraviolet background heating (starting from Haardt and Madau, 1996). So far the jets are the only source of heating present in our simulations.

**Diffuse Unit** implements diffusive effects, such as heat conduction, viscosity, and mass diffusivity.

**Gravity Unit** computes gravitational source terms for the code (RHS in equation 2.3). These source terms can be provided in the form of the gravitational potential  $\Phi(x)$  or the gravitational acceleration  $\mathbf{g}(x) = -\nabla\Phi(x)$ . The gravitational field can be externally imposed or self-consistently computed from the gas density via the *Poisson equation*:

$$\nabla^2\Phi(x) = 4\pi G \rho(x) \quad (2.14)$$

where  $G$  is Newton's gravitational constant. The Gravity Unit contains several gravity solver algorithms; the choice is mainly affected by the hydrodynamical solver adopted; we could adopt the either the Pfft or the PPM.

Though FLASH allowed to impose an external potential or to calculate the fluid self gravity, it did not allow to adopt a combination of both. We added the self-gravity of the hot gas present in the galactic halos we consider on top of an external Dark Matter potential. The Dark Matter profile we chose is a broadly used NFW (Navarro et al., 1996), for which we provided the potential  $\Phi(x)$ ; this choice turned also handy for assigning the gas' initial conditions (see Section 2.4).

**Particles Unit** FLASH can deal with several type of particles. They can be *active*, if they interact somehow with the main mesh, or simple *passive* fluid tracers.

A particular type of active particles are the *Sink* particles. Their nature of sinks allows them to accrete gas mass by sweeping (if moving) or pure gravitational attraction. Sink particles were developed to remove sink regions from the grid, since gravity calculations in such regions can be particularly computationally intense. In astrophysical environment, they are instead mostly used for modeling star formation via direct *Jeans' collapse*; this can of

course be seen only in the scales resolved by the simulations; on galactic-size or larger simulations, as in this case, one definitely cannot resolve formation of individual stars. But gas clouds a few tens or even hundreds of parsecs in size can be seen collapse in a sink. Sink particles were fully integrated in our setup, though no actual production run involving this feature has been launched yet.

**Cosmology Unit** solves the Friedmann equation for the scale factor in an expanding universe, applies a cosmological redshift to the hydrodynamical quantities, and supplies library functions for various routine cosmological calculations needed by the rest of the code for initializing, performing, and analyzing cosmological simulations. We do not make explicit use of cosmology.

**Material Properties Unit** can additionally consider a fluid's diffusion, viscosity, conductivity, opacity, magnetic resistivity.

**Radiative Transfer Unit** Quite a recent addition; allows computation of radiative transfer making use of the *Multigroup diffusion* approximation.

## 2.4 Our setup

After describing the physical processes modeled in our setup, all is left to specify is the initial conditions we adopt and the parameters of our jets. In this section we will introduce the different components, while the values of all the parameters will be set for each simulation as specified in Sections 3.2 and 4.1.

Our setup comprises:

**A dark matter halo** in the form of a static gravitational potential. As specified in Section 2.3, we use a spherically symmetric Navarro-Frenk-White (NFW) density profile (Navarro et al., 1996):

$$\rho_{\text{NFW}}(r) = \frac{\rho_{\text{NFW}}^0}{\frac{r}{r_s} \left(1 + \frac{r}{r_s}\right)^2} \quad (2.15)$$

where  $\rho_{\text{NFW}}^0$  and the *scale radius*  $r_s$  vary from halo to halo. This dark matter density creates a gravitational potential of the form:

$$\Phi_{\text{NFW}}(r) = -4\pi G \rho_{\text{NFW}}^0 r_s^2 \frac{\ln\left(1 + \frac{r}{r_s}\right)}{\frac{r}{r_s}} \quad (2.16)$$

having chosen  $\Phi_{\text{NFW}}(r = +\infty) = 0$ .

**A hot gas component** For the coronal gas in the hot halo, we adopt the simple initial density profile from Capelo et al. (2010). This corresponds to gas at a uniform

temperature  $T_0$  in hydrostatic equilibrium with an external potential  $\Phi$  (neglecting, but only at this stage, the gas' self-gravity):

$$\rho_{\text{gas}}(r) = \rho_{\text{gas}}^0 e^{-\frac{\mu m_p \Phi}{k_B T_0}} \quad (2.17)$$

where  $\rho_{\text{gas}}^0$  is a normalization parameter,  $\mu m_p$  is the mean gas molecular weight and  $k_B$  is Boltzmann's constant. We have  $\Phi = \Phi_{\text{NFW}}$ , but other components (e.g. gravity from stars) may be simply added at this stage.

**A bipolar jet** We shoot a hot, bipolar jet from the halo center. In order to keep the jet cross section  $A_{\text{jet}}$  of such jet as small as possible, we developed a discretized jet model that can be shot directly from a few selected cells. The jet has got a uniform, cylindrical profile, with constant injection density  $\rho_{\text{jet}}$  and velocity  $v_{\text{jet}}$ . Earlier attempts with a smoother profile had been done, but our grid has resulted -on average- too coarse to make it of practical use; unlike Tortora et al. (2009), who used such a profile, but only in 2D simulation, and adopt a simulation box often smaller than ours. We have our jets obeying to the following constraints:

(Jets' Power)

$$P_{\text{jet}} = \rho_{\text{jet}} A_{\text{jet}} v_{\text{jet}}^3 \quad (2.18a)$$

(Jets' Mach number)

$$\mathcal{M}_{\text{jet}} = \frac{v_{\text{jet}}}{\sqrt{\gamma p_{\text{jet}} / \rho_{\text{jet}}}} \quad (2.18b)$$

(Jets' density contrast)

$$\delta_{\text{jet}} = \rho_{\text{gas}}^0 / \rho_{\text{jet}} \quad (2.18c)$$

Here  $\mathcal{M}_{\text{jet}}$  is the jet's *internal Mach number* and  $p_{\text{jet}}$  is its thermal pressure (in Equation 2.18b, the adiabatic expression for the gas sound speed has been used).

We fix  $P_{\text{jet}}$ ,  $A_{\text{jet}}$ ,  $\mathcal{M}_{\text{jet}}$  and  $\delta_{\text{jet}}$  and solve for the rest.  $A_{\text{jet}}$  depends on the jet orientation with respect to the simulation grid, and the distribution of cells that constitute the jet base (the approximation of a cylinder with cubic cells). All these aspects are calculated in advance.

Parametrizing the jet/gas density contrast  $\delta_{\text{jet}}$  (typically in the range 50 – 200, but not always, as in Chapter 3) as in Equation 2.18c -rather than directly  $\rho_{\text{jet}}$ - is handy when changing the halo parameters.

**A cold gas component** The setup contains also a cold/warm gas component, in the form of an arbitrary distribution of spherical clouds, featuring a *Truncated Isothermal Sphere* (TIS) density profile (Shapiro et al., 1999). This profile grants a finite central density, as the cold gas is supported by the coronal gas' external pressure, with which is in equilibrium. There is also the possibility of providing the clouds with bulk orbital velocity around the halo, and internal density dispersion. The aim is to use these clouds to model warm neutral gas (typically  $10^4$  K) in which star formation could take place (to be traced by sink particles as discussed in Section 2.3), extending what done in 2D by Tortora et al. (2009).



**Figure 2.4:** This cartoon (not to scale) has been obtained by collageing actual renderings of simulation outputs. It sketches: a hot gas halo (orange), an evolved jet shot from the halo center (green) and some cold gas clouds (light blue). The cold gas clouds are not included in the main simulations presented in this work, but some runs featuring them are discussed in Section 5.2

Simulations featuring these cold gas clouds are to be run in the near future (see Section 5.2).

The interplay of the gaseous components is sketched in Figure 2.4.



---

## Early Evolution Stages of Jet/ISM Interaction <sup>1</sup>

---

We begin our study of the interactions of an AGN with the InterStellar Medium (ISM) by exposing the results of some of our simulations, aiming to model the first few millions of years of such systems with a very high level of detail. This work is important in order to understand the effects of the fundamental parameters in play by varying the properties of the jet and/or the host halo (Section 2.4). In turn, not needing long-term evolution, it is possible for the moment to adopt a small simulation box (see Section 3.2), neglect the gas self-gravity and push the resolution level up (see discussion in Section 2.3).

### 3.1 What we can learn from the early stages

This setup allows us to address many highly debated questions. Among the most important of these questions, some concern, generally speaking:

1. the first evolutionary stages of these objects: if and how observed compact radio sources<sup>2</sup> eventually evolve into extended sources such as FR II galaxies;
2. whether the coupling between the AGN and the rest of its host galaxy or halo is high enough to allow for substantial energy transfer, and how this is achieved;
3. the jet physical composition and thermodynamic state after its contacts with the ISM, which also greatly affects the previous point;
4. whether some self-regulation mechanism is driving the alternation between active and passive phases, e.g. by regulating the central mass inflow rate.

---

<sup>1</sup>Essentially, Cielo et al. (2014)

<sup>2</sup>such as CSSs, *Compact Steep Spectrum sources* and GPSs, *Gigahertz Peaked Spectrum sources*

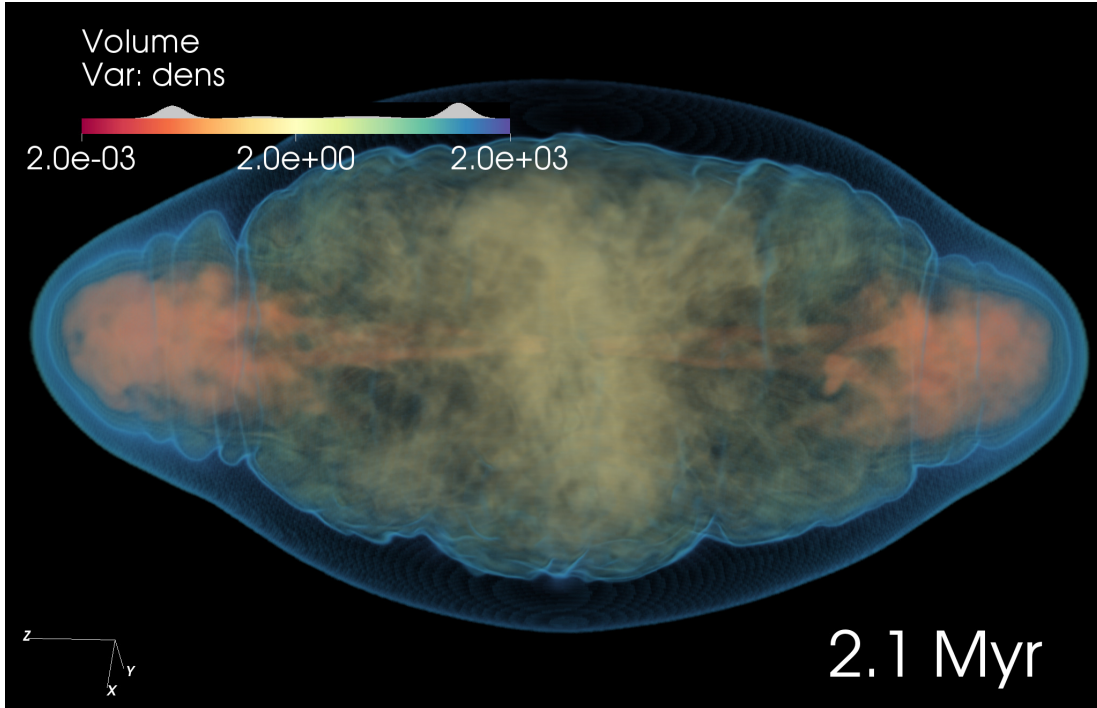


**Figure 3.1:** 3D ray-tracing density rendering of run dj-250p6, at 2.1 Myr. The legend shows, above the color code, the corresponding opacity used for the ray tracing. This combination was chosen to highlight different regions: bow shock (blue), cocoon material (yellow), jets and lobes (orange). The external ISM is not shown for simplicity.

For decades, several steps have been taken in theoretically models or implementations of jet feedback in coherently simulated scenarios to investigate these problems. Most difficulties arise from AGNs being intrinsically multi-scale objects, in which one has to model and resolve several physical processes, such as hydrodynamics, radiative cooling, gravity and star formation, as pointed out extensively in Chapter 1.

As for the early evolution of radio galaxies, several analytic models have been proposed. The model by Falle (1991) and later extended by Kaiser and Alexander (1997); Alexander (2002) describes the *global average* properties of cocoon dynamics in term of this expansion, predicting that the cocoon's expansion is self-similar during most of its life. However, this self-similar expansion model leaves out questions related to the internal dynamics and thermodynamics of the jet-cocoon system. Under realistic circumstances, self-similarity may not hold, and indeed it is not likely to. Kino and Kawakatu (2005) and Kawakatu et al. (2008) propose a model for expansion in a non-uniform ISM which accounts separately for the cocoon transverse expansion, thus not implying (albeit not excluding) self-similarity, and test it against young radio galaxies.

Important results have been found also through simulations: for instance Sutherland and Bicknell (2007) described precise evolutionary stages for the jet/cocoon system; on larger scales Heinz et al. (2006) reproduced X-ray luminosities of observed bright sources such as Cyg $\alpha$ .

Other authors such as Sheikhnezami et al. (2012); Fendt and Sheikhnezami (2013) provided insights on jet-launching mechanisms from magnetized accretions disks;

McKinney et al. (2012) studied accretion flows on spinning black holes in general relativistic magnetohydrodynamic (GRMHD) simulations, finding highly magnetized states that drive inflows and generate stable relativistic jets in agreement with the *Blandford-Znajek* (BZ) jet model (Blandford and Znajek, 1977). Also Sadowski et al. (2013) and Penna et al. (2013) used GRMHD simulations to investigate different disk and magnetic field configurations, that again appear consistent with the BZ model (see also Section 1.2.2).

The energy balance of the jet feedback, and its effects on star formation have been studied through hydrodynamic simulations: Gaibler et al. (2011) found asymmetries between the two lobes to be significant; Gaibler et al. (2008) and Gaibler et al. (2012) studied the interaction with the ISM, with particular attention to star formation, favouring a positive feedback scenario. Tortora et al. (2009) obtained color indexes from 2D simulations, which indeed suggested a positive feedback initial transient phase, triggered by mechanic gas compression, but overall negative feedback (due to cold gas heating and clump destruction) after a few tens of Myr. Their predicted colours agree well with observed spheroidal galaxies that had AGN-related events.

The importance of self-regulation in AGN environments has been recently highlighted by Gaspari et al. (2011b,a), who studied in detail the interplay of AGNs with cold/hot accretion. Antonuccio-Delogu and Silk (2010a) have demonstrated the rise of *backflows* within the global circulation inside a *cocoon* (see Perucho and Martí, 2007; Rossi et al., 2008; Mizuta et al., 2010) generated by the interaction of an AGN jet with the ISM of its host galaxy. Such backflows have been noticed since the first numerical simulations (Norman et al., 1982; Antonuccio-Delogu and Silk, 2010a); they do act as a self-regulation mechanism, driving gas back towards the meridional plane in a two-lobe system. In the aforementioned work by Antonuccio-Delogu and Silk (2010a), these backflow are a consequence of local discontinuities in the entropy. In that framework, *Crocco's theorem* states that such discontinuities act as a vorticity source term. Since very large entropy discontinuities are present at the interface between the jet and the Hot Spot (HS), strong vorticity may be naturally generated in FR II sources through this mechanism, driving the backflows. This latter paper also observed how the backflows were stable for most of the evolution of the jet-cocoon system, but the scope of this work was restricted by the fact that the simulations were only in 2D.

One problem with analytic models is that it is difficult to predict which among the jet/cocoon internal dynamics are relevant, and properly include them. Though for example Kaiser and Alexander (1997) include jet recollimation shocks, other dynamics may be in play: jet propagation generates turbulence within the cocoon and, if this turbulence is isotropic, an isotropic *turbulent pressure*  $p_t$  arises, which adds to the gaseous thermal pressure<sup>3</sup>  $p_g$ . Also, the results depend on the assumption for the gas distribution in the ISM. This is true also for simulations: changing for instance the distribution of the cold (or warm) gas phase affects the results heavily; also, there is so far no general agreement on feedback outcomes or indications for a unitary picture of AGN jets.

---

<sup>3</sup>Throughout this paper we will use uppercase  $P$  to denote power, and lowercase  $p$  to denote pressure

In the present paper we focus our attention on the *internal* properties of the jet-cocoon system in a new set of full 3D, *Adaptive Mesh Refinement* (AMR) simulations, where we provide detailed cocoon shape measurements. We try to compensate our ignorance on the jets' physical composition by running different "families" of simulations varying the jet/ISM density contrast and relating this to the cocoon shape. We then investigate the jet/cocoon thermodynamical properties: how pressure shares between turbulent and isothermal pressures, whether turbulent pressure affects the global dynamics of the cocoon, and how this is linked to the evolution of the system. We analyse the cocoon/ISM energy balance, including the energy deposition in the form of mechanical " $p dV$ " work and likewise " $T dS$ " exchanged heat.

In the end, we present updated results on backflows: we study how much they can contribute to supply the accretion region around the SMBH with gas and energy. The backflow carries very hot, high pressure gas; thus, it can heavily affect the *circumnuclear star formation* and the properties of the accretion disc.

The simulation setup we use is introduced in Section 3.2, while an overview of the typical run evolution is in Section 3.3. Section 3.4 and 3.5 are dedicated to cocoon geometry and thermodynamics, respectively. We deal with backflows in Section 3.6, while in Section 3.6.2 we also investigate their *stability*, which affects this feedback mechanism. Section 3.7 contains the discussion.

## 3.2 Simulation setup and runs

### 3.2.1 Simulation volume

The initial setup is devised to model the environment of a spheroid, which could either be an early-type galaxy or a pseudo-bulge component of a late-type one, with an isothermal gaseous profile embedded in equilibrium within a Dark Matter halo. In the present work we are mainly interested in modelling the large-scale properties of the jet-cocoon system, thus we do not put a disc of cold clouds as, for instance, in Wagner et al. (2012). A disc indeed is not likely to affect large-scale properties, as found for instance in Gaibler et al. (2012).

Our jets propagate into a hot, isothermal ( $T = 10^7\text{K}$ ), low-density ISM, representative of the diffuse ISM of the spheroid described above. The spheroid is not rotating, in order to test the effects of the jet in the most straightforward way. We wrote our setup in FLASH, a block-structured, adaptive mesh-refinement hydrodynamic code (see Fryxell et al., 2000). We adopt a rectangular simulation box, with a volume of  $[60 \times 60 \times (2 \times 60)] \text{ kpc}^3$ , so that the jet can be shot from the centre and propagate parallel to the longest side. We had FLASH dealing with it as the juxtaposition of two cubic cells, through the use of the *Multigrid/Pfft* hydro-solver, capable of dealing with simulation boxes of such composite (non-cubic) shape. *Multigrid* refers to the algorithm capability of dealing with grids with non-uniform resolution (as many in FLASH can); *Pfft* explicates that Fourier transforms are executed with parallel solvers on the whole domain, instead of serial solvers applied block-by-block by local processors. This improves the algorithm scalability and fixes an important load imbalance

Name	$\sigma_V$	$\rho_{halo}^c$	$\rho_{jet}$	$p_{jet}$	$\log(P_{jet})$	$\mathcal{M}_{int}$	$t_{MAX}$
	km s <sup>-1</sup>	MFLY Mpc <sup>-3</sup>	MFLY Mpc <sup>-3</sup>	PFLY	Watt		Myr
<i>Fiducial family</i>							
150p3	150	2311.3	23.113	10 <sup>3</sup>	37.6727	164.4	2.2
150p5	150	2311.3	23.113	10 <sup>5</sup>	37.6727	16.4	3.1
150p6	150	2311.3	23.113	10 <sup>6</sup>	37.6727	5.2	3.6
200p5	200	1748.28	17.4828	10 <sup>5</sup>	37.9359	19.2	2.3
200p6	200	1748.28	17.4828	10 <sup>6</sup>	37.9359	6.1	2.7
250p5	250	1410.2	14.102	10 <sup>5</sup>	37.14	21.7	1.9
250p6	250	1410.2	14.102	10 <sup>6</sup>	37.14	6.9	3.8
<i>Denser ISM family</i>							
d+200p5	200	17482.8	17.4828	10 <sup>5</sup>	37.9359	19.2	1.4
d+200p6	200	17482.8	17.4828	10 <sup>6</sup>	37.9359	6.1	2.8
d+250p5	250	14102	14.102	10 <sup>5</sup>	38.14	21.7	5.7
d+250p6	250	14102	14.102	10 <sup>6</sup>	38.14	6.9	5.5
<i>Light jet family</i>							
dj-200p5	200	1748.28	1.74828	10 <sup>5</sup>	37.9359	13.1	2.1
dj-200p6	200	1748.28	1.74828	10 <sup>6</sup>	37.9359	4.13	2.5
dj-250p6	250	1410.2	1.4102	10 <sup>6</sup>	38.14	4.67	3.1

**Table 3.1:** Defining parameters of our simulation runs: run name, halo central velocity dispersion  $\sigma_V$ , central (Dark Matter) halo density  $\rho_{halo}^c$ , jet density  $\rho_{jet}$ , jet pressure  $p_{jet}$  (a proxy for its internal energy  $e_{jet}$ ), jet injection mechanical power  $P_{jet}$ , the related jet's internal Mach number  $\mathcal{M}_{int}$ , final simulation epoch  $t_{MAX}$ . The other halo and jet physical parameters are all uniquely determined from these ones by using the scaling relations discussed in Section 3.2. The first seven runs make up our *fiducial* family, and have their density contrast  $\rho_{halo}^c / \rho_{jet}$  set to 100. The prefix “d+” denotes the *denser ISM* runs, that have a ten times larger  $\rho_{halo}^c$ . Prefix “dj-” denotes the *light jet* family, that has instead the  $\rho_{jet}$  reduced by the same factor. Thus in both cases  $\rho_{halo}^c / \rho_{jet} = 1000$ . We remind that MFLY  $\simeq 5.23 \times 10^{12} M_\odot$  and PFLY  $\simeq 1.80 \times 10^{-15}$  Pa.

of some original Multigrid methods. We use the FLASH default *outflow* boundary conditions on all the sides of the box.

We take advantage of the FLASH Adaptive Mesh Refinement (AMR) capabilities to achieve high spatial resolution: in the FLASH AMR implementation, the simulation volume is recursively divided on-the-fly in blocks, splitting in half along each direction at each level of refinement (e.g. in 3D every block is split in 8 equal parts). This goes on until the user-set refinement criteria are no longer verified (i.e. gradients calculated on the grid are not too large), or the chosen maximum refinement level  $l_{max}$  is reached. We use the FLASH's default refinement criteria, based on Loehner's error estimator, set to 0.8 for refinement and 0.6 for de-refinement. In all the runs we show in this work (Table 3.1) we put  $l_{max} = 9$ . This implies that the smallest block will have a volume  $L_b^3 / (2^9)^3 = 7.45 \times 10^{-9} L_b^3$ . Each block is further divided in cells: we use  $8^3$  cells per block. "In this way, we have a smallest cell size of  $6 \times 10^4 pc / 8 / 2^9 \simeq 14.6 pc$ , sufficient to resolve small scale turbulence creation/dissipation.

We adopt, as the internal unit system, the *FLY system* ( $L_0 = 1 \text{ Mpc} t_0 = 2/3 H_0, M_0 = 5.229 \times 10^{12} M_\odot$ , so that:  $GM_0 t_0^2 / L_0^3 = 1$ , see Antonuccio-Delogu et al., 2003) in order to avoid numerical truncation problems which may arise in SI or CGS units.

Our physical setup includes gravity from an external, static dark matter halo having a NFW (Navarro et al., 1996) density profile, plus the contribution of a central SMBH. As for the hydrodynamic component, we model a single-fluid multi-phase gas. A hot ISM phase is specified as an initially isothermal ( $10^7$  K) plasma, embedded in gravitational equilibrium within the NFW external potential, and subject to radiative cooling. The other component we adopt are the jets: from the very centre of the halo we launch two jets in opposite directions, modeled as a uniform, cylindric constant source term of about 30 pc diameter (a few cells).

We also include plasma energy loss by radiative cooling, implemented as prescribed by Sutherland (1993), whose tables have been extended to higher plasma temperature, up to  $10^{12}$ K (Antonuccio-Delogu and Silk, 2008a, Appendix B).

We then follow the evolution of the jets+ISM system for several Myr, in order to observe the early stages of their life, and the transition phase to larger sources such as the Medium-sized Symmetric Objects (MSOs) or fully-developed FR II galaxies. A visual impression is given in the 3D rendering in Figure 3.1.

### 3.2.2 Scaling relations, host galaxy and jet parameters

Our setup can be seen as the 3D extension of the one adopted in Antonuccio-Delogu and Silk (2008a, 2010a). For our first family of runs (which we call the *fiducial* runs in Table 3.1), the physical parameters of the halo and jet are all chosen as in Antonuccio-Delogu and Silk (2010a), taking just the average value of the scaling relations cited therein, with the aim to describe low/medium power FR II radiogalaxies. Everything is once again calibrated on the halo central velocity dispersion  $\sigma_V$ .

The virial mass  $M_{vir}$  of the host halo is assumed to scale with  $\sigma_v$  as in Figure 3 of

Lintott et al. (2006)

$$M_{vir} = 2.57 \times 10^{12} \left( \frac{\sigma_V}{200 \text{ km s}^{-1}} \right)^{2.99 \pm 0.15} M_\odot \quad (3.1)$$

which we use in turn to predict the halo concentration parameter  $c_{NFW}$  as in Macciò et al. (2008):

$$c_{NFW} = 9 \left( \frac{M_{vir}}{M_*} \right)^{-0.13}, \quad M_* = 1.5 \times 10^{13} h^{-1} M_\odot \quad (3.2)$$

From these two parameters, one can analytically calculate the halo's virial radius  $r_{vir}$ , taken as the radius for which

$$M_{vir} = 200 \times \frac{4}{3} \pi r_{vir}^3 \rho_{crit} \quad (3.3)$$

where  $\rho_{crit}$  is the critical density of the Universe. We do not aim to be cosmologically accurate, so we just use a  $\Lambda$ -CDM cosmology with reduced Hubble constant  $h = 0.7$ . We finally calculate the halo central (dark matter) density from the definition of the  $c_{NFW}$  parameter:

$$\rho_{NFW}^0 = M_{vir} / (4.0 \pi f_c r_S^3) \quad (3.4)$$

being  $r_S = r_{vir} / c_{NFW}$  the *scale radius* of the halo and

$$f_c = \log \left( 1 + c_{NFW} - \frac{c_{NFW}}{1 + c_{NFW}} \right).$$

For the central black hole, we assume that its mass  $M_{BH}$  scales with  $\sigma_V$  according to the relation found by Ferrarese and Merritt (2000):

$$M_{BH} = (1.2 \pm 0.2) \times 10^8 \left( \frac{\sigma_V}{200 \text{ km s}^{-1}} \right)^{3.57 \pm 0.3} M_\odot \quad (3.5)$$

and finally, for the jet total mechanical power  $P_{jet}$  we follow Eq. 9 of Liu et al. (2006) (where we put  $\lambda = L_{bol} / L_{edd} = 0.1$ ):

$$\log_{10}(P_{jet}) = -0.22 + 0.59 \log_{10} \left( \frac{M_{BH}}{M_\odot} \right) + 33.48 \quad (3.6)$$

where  $P_{jet}$  is expressed in Watt; this assumes that the jet power ultimately comes from BZ process, as supported by recent GRMHD simulations (e.g. Tchekhovskoy et al., 2012).

We have then chosen three cases, namely the ones corresponding to  $\sigma_V = 150, 200$  and  $250 \text{ km s}^{-1}$ . In the fiducial runs, the jet density  $\rho_{jet}$  is assumed to be  $1/100$  of the central halo density; the source velocity  $v_{jet}$  is thus determined by  $P_{jet}$ . In order to completely specify the source thermodynamic state, we have to also set the pressure  $p_{jet}$  of the jet plasma (or, equivalently, its temperature  $T_{jet}$ ). This variation corresponds to different internal Mach numbers  $\mathcal{M}_{int}$  of the jet, so by varying this parameter we can explore different regimes.

We limit ourselves to the supersonic case -where the system is not supposed to be very sensitive to this parameter- pushing towards the edge of the transonic case

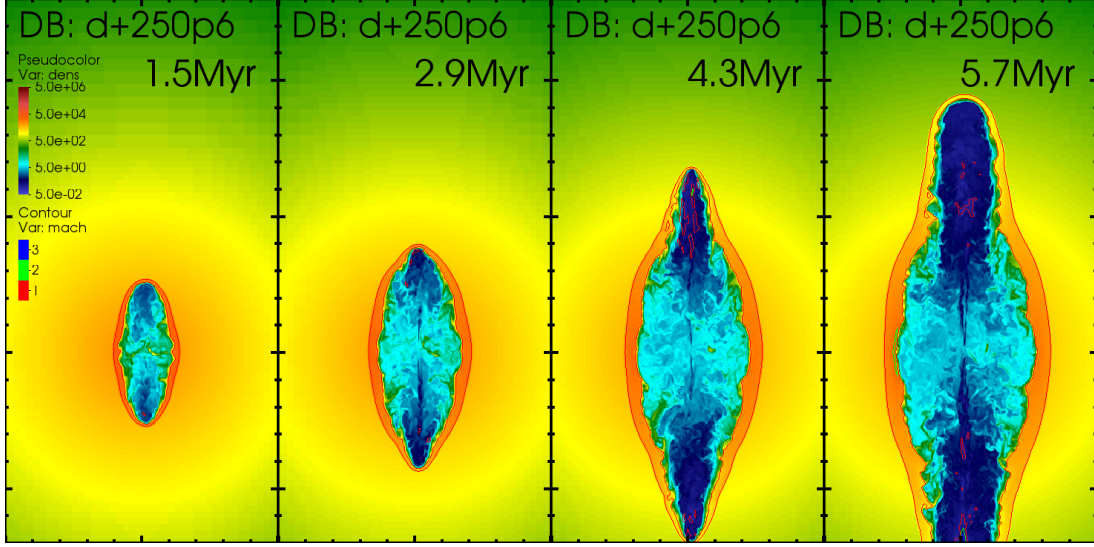


**Figure 3.2:** Central plane density slices of run d+250p6, showing four evolutionary stages, from 1.5 to 5.7 Myr. The contours show the fluid Mach number. Size:  $10 \times 20$  kpc (small ticks every kpc, large ones every 5 kpc). The halo centre is located at 7 kpc from the bottom edge. This run has been chosen for having the highest simulation age, and for showing clearly many important features, such as cocoon formation and penetration.

( $\mathcal{M}_{int} \sim 4$ ). In order to approach these values, we had to set  $p_{jet} = 10^6 \text{PFLY}$  (i.e.  $1.8 \times 10^{-9} \text{Pa}$ ). For the highly supersonic runs, we have safely set a value of  $p_{jet}$  ten times smaller.

We then designed a *light jet* family of runs, denoted by the prefix “dj-” and obtained by decreasing the jet density in order to have a density contrast of 1/1000. In turn we raised  $v_{jet}$  to still match the same  $P_{jet}$ . Jets of such densities are considered *very light*, yet they are commonly adopted in order to have less elongated cocoons (Gaibler et al., 2008). Thus, we decided to run a third family, the *denser ISM* family (“d+” prefix), where the same density contrast is obtained by raising the ISM central density by a factor of ten.

### 3.3 Evolutionary stages

The runs listed in Table 3.1 show different evolution paths, yet we can identify three main evolutionary phases. In Figure 3.2 we show one significant run for illustration purposes (run d+250p6), while differences among runs are presented in Figure 3.4.

Furthermore, some runs more than others show asymmetry between the two jets/cocoons, so that the two halves of the cocoon can be at different stages at the same time. But these asymmetries are never very significant, as they get less pronounced with increasing simulation time  $t_{age}$ . This is simply a consequence of the development of turbulence, as asymmetry occurs apparently “at random” for what concerns direction, timing and intensity.

We can identify three main phases in the evolution of the jet-cocoon system:

1. **“C” phase: Cocoon and hotspot formation** - At the very beginning of the simulation ( $t \lesssim 0.1$  Myr) the (highly supersonic) jet produces -through a strong shock- a *hotspot* (HS) right where the dense ISM is frontally hit. The HS spans less than 1 kpc in size, and it is characterized by very high temperature ( $T \gtrsim 10^{11}$  K) and pressure.

Meanwhile, an ellipsoidal *bow shock* region starts to expand from the centre, moving at approximately its local speed of sound. This wavefront wipes and accumulates gas in a thin (roughly a few hundreds of pc) layer, that “shields” the ISM from the hot jets. This bow-shock fronts continues to propagate in all directions, isolating an “inner” region: the cocoon. In the following we will (as in e.g. Falle, 1991, Kino and Kawakatu, 2005) treat the cocoon as a two-axial ellipsoid. We also follow separately its two halves, accounting for asymmetry between the two jets. We will indicate the semi-major axis with  $r_{HS}$ , as it coincides with the distance of the HS from the centre<sup>4</sup>. The semi-minor axis will be  $r_C$ , for *cocoon radius*.

This phase lasts about 0.3 Myr for the fiducial runs, but it can last up to  $\leq 1$  Myr if the density contrast is enhanced. In Figure 3.2, a late C phase is shown in the first panel. For many aspects, this phase corresponds to the “transition phase” mentioned in Alexander (2006) for young, compact radio sources, until the forming cocoon reaches a well-defined shape (which may still evolve after that). Yet this transition requires longer times than predicted in that work (a few hundreds of thousands of years instead of a few tens of thousands) due to the complexity of the hydrodynamics.

2. **“F” phase: Forward propagation** - This stage shows quite complex hydrodynamics. Once the cocoon has formed, the internal jet propagates forward and may undergo some recollimation shocks, more likely for high  $\mathcal{M}_{int}$ . In the forward direction, the jet keeps building pressure in the HS. At the same time the jet is coupled to the cocoon, providing energy and gas to “inflate” it.

Asymmetry and irregularity in the cocoon start to be visible at this stage, together with significant backflows (see Section 3.6); the contribution of the turbulent pressure  $p_t$  is decreasing but still dynamically important (Figs. 3.5 and 3.6). The cocoon axis ratio  $r_{HS}/r_C$  seems here to settle on a well defined regime, but not necessarily self-similar. During this stage the jet pierces its own cocoon (see Section 3.4), thus decoupling from it. This usually, but not always, coincides with the beginning of the next phase. Phase F lasts until about 2 Myr (or 3, for enhanced density contrast runs), and corresponds to the second panel of Figure 3.2.

3. **“L” phase: Lobe formation** - Right after the cocoon piercing, the ISM is no longer shielded from the jet; also, the “naked” HS is now in the outskirts of the halo (about 20 kpc), where the gas density and pressure are not high enough for similar shielding effects. Thus, the gas coming from the jet and the inner part of the cocoon undergoes a fast and less directional expansion; the outcome of this is

<sup>4</sup>Actually, having a bipolar jet, we take the mean of these two distances for each run; see Section 3.4 for a formal definition of these parameters

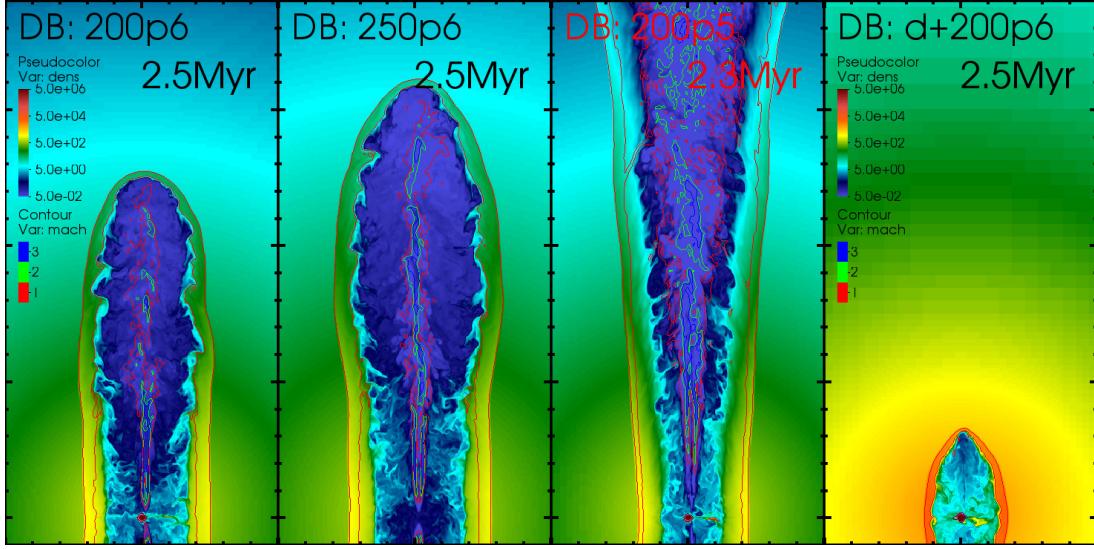


**Figure 3.3:** Visual comparison of different runs at 2.5 Myr. Image size and color code are the same as Figure 3.2. **First panel:** here we take run 200p6 as a reference model. In the next panels we change one parameter per time. **Second panel:** run 250p6; increasing  $\sigma_V$  leads to a faster and more penetrating jet. **Third panel:** run 200p5, shown at 2.3 Myr only due to its very fast evolution. Decreasing  $p_{jet}$ , cocoon piercing events occur earlier, so the jets propagate faster, while the cocoon semi-minor axis  $r_C$  remains smaller; lobes form faster. **Fourth panel:** run d+200p6 (note the higher ISM density) shows that an increased density contrast results in a rounder cocoon and a slower propagation.

the formation of large lobes (a few tens of kpc, still expanding at the end of the simulation time) similar to the ones observed in FR II radiogalaxies, the HS being still well-defined (Kharb et al., 2008).

Due to this expansion, the cocoon semi-minor axis  $r_C$  is now an ill-defined quantity (as there is no longer a cocoon); indeed in Figure 3.4 it has a clear turn-up point. The denser ISM and light jets families runs show again a delayed behaviour, so not all of them were reached the state of having well-defined lobes; but all show cocoon piercing. The moment of piercing and the subsequent expansion are shown in the third and fourth panel of Figure 3.2, respectively.

Usually, after the cocoon piercing, the rapid expansion causes FLASH to refine a very large volume, requiring much more memory; thus the simulation runs stop at this stage. In one case (200p5) the jet went out the simulation box before that happened. The different components (jets, early lobes, cocoon material and bow shock region) are all highlighted in Figure 3.1.

This picture shows some elements in common with earlier simulations (Sutherland and Bicknell, 2007; Tortora et al., 2009; Gaibler et al., 2011; Wagner and Bicknell, 2011; Antonuccio-Delogu and Silk, 2010b) and theoretical models (Falle, 1991; Alexander, 2006). Yet we are now able to link these elements with the internal dynamics, in a more organic picture. Details vary according to the different assumed ISM models, and the absence of cold gas in our runs. Comparison to 2D simulations performed with a similar setup (Tortora et al., 2009) shows striking differences. First, a much higher density contrast  $\rho_{ISM}/\rho_{jet}$  is needed in order to recover the same cocoon shape, that otherwise is more extended in the forward direction; this could be due to 2D

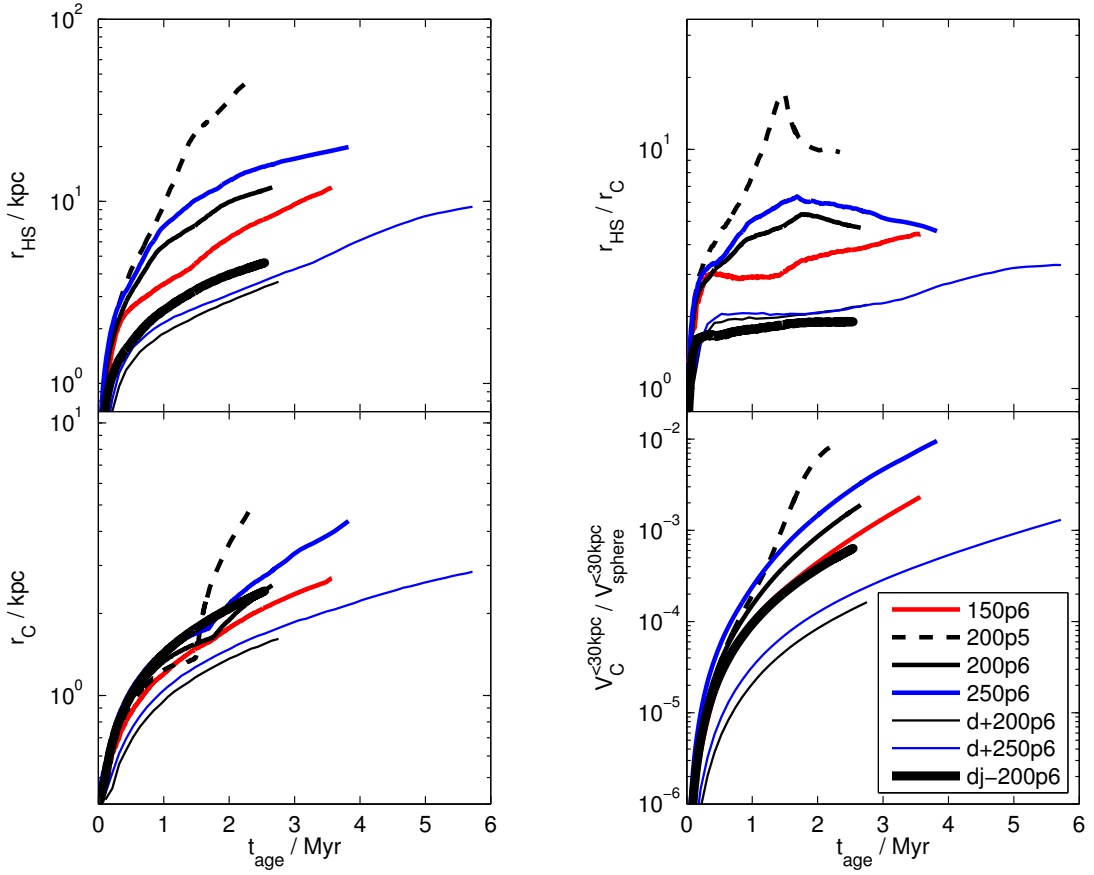


**Figure 3.4:** Geometrical properties of the cocoon (selected as the region where  $T > 2 \times 10^9$  K). **Plot style coding:** same line color means same  $\sigma_V$ , same line style means same  $p_{jet}$ , while line thickness discriminates *fiducial* runs ( $\rho_{jet} / \rho_{halo}^c = 0.01$ ) from *enhanced density contrast* runs ( $\rho_{jet} / \rho_{halo}^c = 0.001$ ). **Left:** time evolution of the cocoon average semi-major (top) and semi-minor (bottom) axes  $r_{HS}$  and  $r_C$ . **Right:** cocoon aspect ratio  $r_{HS}/r_C$  (up) and total volume  $V_C$  inside a 30 kpc-radius sphere (bottom) over time.

simulations not dealing properly with the turbulent pressure. The 2D simulations also tend easily to show too strong jet *recollimation*.

The gas circulation inside the cocoon looks also very different (see Section 3.6) once the third dimension is added.

### 3.4 Cocoon geometry

We want now to focus on the cocoon’s shape and size in the different runs. What we had shown by visual impression in Figure 3.3, will be now quantified in Figure 3.4, where we consider the evolution of the cocoon’s semimajor and semiminor axes and volume.

These quantities have been calculated as follows: first we have selected all the cells in the mesh’s grid in which the temperature is  $\leq 2 \times 10^9$  K; this includes, for all runs, the cocoon region, the jets and the lobes, leaving out only the bow shock front and the unperturbed ISM. We refer to this operation as our “cocoon selection”.

Then, the maximum extent along the jet axis define the semi-major axis  $r_{HS}$  (top-left panel in Figure 3.4), while the maximum extent along the transverse direction defines the semi-minor axis  $r_C$  (bottom-left panel). We also show the ratio  $r_{HS}/r_C$  as a cocoon shape indicator (top-right); note that no shape constraint is assumed in the semimajor and semiminor axes extraction, which are two independent numbers.

As a last geometric property of the cocoon, we want to estimate the fraction of the surrounding ISM that is affected by the jet. So we calculate the fraction of the cocoon volume  $V_C$  with respect to a sphere centered on the jet origin, and having a radius of 30 kpc (bottom-right). This volume fraction is then an indicator of the feedback activity on this scale.  $V_C$  is just the sum of the volumes of the cells that pass the cocoon selection criterion, being another measure independent from the semimajor and semiminor axes.

In the first three panels of Figure 3.4, kinks in the curves are visible, clearly corresponding to phase changes. During phase C, i.e. the first  $\sim 0.3$  Myr the density contrast is the only parameter that plays an important role in determining  $r_{HS}$  and the aspect ratio of the cocoon, so that the enhanced density contrast runs show the slowest forward propagation in favour of a less elongated cocoon shape. In other words, the cocoon inflation is a more isotropic process.

After entering phase F, i.e. after 0.5 to 1 Myr, we can distinguish the effects of all the parameters. From the plots we see that  $p_{jet}$  becomes the most important parameter; indeed the 200p5 (black dashed line) run shows little resistance from the ISM, and a very directional cocoon. The other fiducial runs decouple earlier from this trend, right after 1 Myr or less, the earlier the lower  $\sigma_V$ . It is worth recalling that, due to the scaling relations used in our parametrization scheme, higher  $\sigma_V$  means more massive haloes, but also higher jet power  $P_{jet}$  and velocity  $v_{jet}$ . So, this simply means that more powerful jets propagate faster, provided that the injection pressure  $p_{jet}$  is the same.

Nevertheless, for a density contrast of 1000, this is only a second order effect. Runs with this enhanced density contrast not only keep showing a less elongated cocoon which expands more slowly, but this expansion is also largely self-similar, with an aspect ratio close to the value of 2. Also, the aspect ratio can poorly distinguish light jets and denser ISM runs, the density contrast being more meaningful than the densities themselves (they in fact matter for  $r_C$  and the total cocoon volume). This is seen in no other run, with the possible exception of run 150p6, in which phase F lasts too short a time to draw a conclusion. In general, the behavior of the fiducial runs in this phase is quite complex and difficult to interpret, suggesting a very strong dependence on internal dynamics.

The cocoon geometry is well captured by the jet injection Mach number  $\mathcal{M}_{int}$  (Table 3.1); the lower it is, the slower and less elongated the cocoon will be. Cocoons created by jets with the same  $\mathcal{M}_{int}$  will be more spherical if the density contrast is higher. The moment of cocoon piercing, when phase L is entered, is clearly marked by an upwards kink in the aspect ratio and even more in  $r_C$ , which now measures the lobe transverse radius rather than the cocoon's. In turn,  $r_{HS}$  is often little affected. This explains why in a Fanaroff-Riley type II galaxy the jet will always be confined by a HS

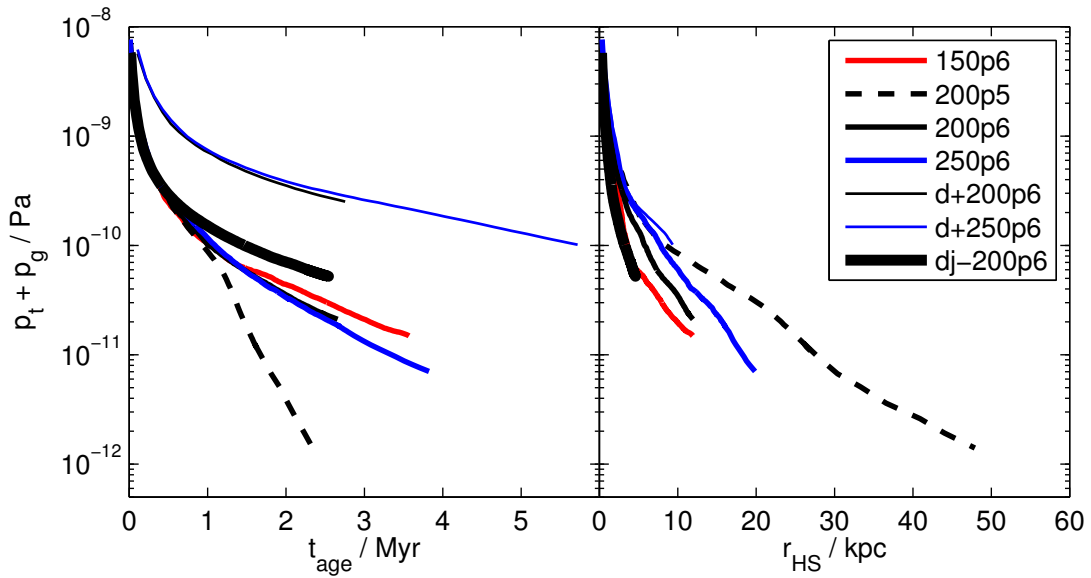


**Figure 3.5:** Total pressure (gas + turbulent) averaged inside the cocoon ( $T > 2 \times 10^9$  K), as a function of time (left) and of cocoon semi-major axis  $r_{HS}$ . The turbulent pressure is computed by Reynolds’ decomposition (see text).  
**Plot style coding:** same as Figure 3.4.

at its end<sup>5</sup> (and a HS is always present in our simulations too). So  $r_{HS}/r_C$  gets lower in most simulations due to the lobe expansion. In runs such as d+250p6 (thin blue solid line) yet this ratio increases. This behavior is illustrated in Figure 3.2: here cocoon piercing does not yet start the lobe creation, but the system is still in its F phase. In order to understand this, we provide some more insight on the piercing mechanism. The bow shock region has both an inner and an outer front, both expanding at the local sound speed (the red contours in the figure mark where the local Mach number is equal to 1). The layer comprised between these two fronts is yet very thin (just a few cells thick, say  $\leq 50$ pc) near the HS. In an elongated cocoon (like in the fiducial runs) this thin edge will be completely destroyed, giving a large opening for the jet to come out and expand in the lobes. In a more spherical cocoon the layer will be this thin only, say, within a few hundred parsecs from the HS; this configuration will thus offer a smaller hole to the jet. The lobes’ expansion is likely to occur at later times for these runs.

The cocoon volume (bottom right panel) increases smoothly with no clear sign of phase change, but it never exceeds 1% of the volume of a sphere of 30kpc radius; thus the ISM fraction affected by the jets is hardly significant in this stage. So feedback from *early* AGNs jet may have only very limited impact in the host galaxy. The cocoons and lobes are in fact still expanding, so one may be confident that in fully-developed sources the scenario will be different.

<sup>5</sup>This is sometimes referred to as the jet never turning “ballistic”

### 3.5 Cocoon thermodynamics

We have performed an analysis of the thermodynamic state of the cocoon; we show its temperature and pressure, together with the energy it exchanges with the external ISM. In the following, whenever we refer to an *intrinsic* quantity, we mean its average value within the cocoon; this does not necessarily imply that the cocoon is in a thermodynamic equilibrium state. In turn, this *cocoon average* is always weighted by the corresponding *extrinsic* quantity; so that every *cocoon average* will be always operated on quantities having the physical dimension of an energy. For instance, pressures will be weighted by cell volumes; velocities (which appear in the turbulent pressure calculation) will be squared and weighted by cell masses, etc.

In Figure 3.5 we show the cocoon mean *total pressure*, as a function of both  $t_{age}$  and  $r_{HS}$  (first and second panel, respectively). This pressure is defined as the sum of the gas (hydrodynamic) pressure  $p_g$  and the turbulent pressure  $p_t$ . The latter has been calculated through a standard Reynolds decomposition (the trace of the Reynolds' tensor), assuming as unperturbed velocity for each cell the mean velocity of its parent block. This is a natural choice, following directly from the AMR structure of our simulation: blocks and cells have different sizes according to their specific refinement level; so the scale on which we have to study (or we can resolve) turbulent motions varies in the same way.

When the ISM is denser (thin solid lines), the cocoon pressure as a function of time is much larger (roughly by a factor of 10, still increasing after the first 2Myr), but this is just because the pressure of the external ISM is likewise increased by a factor of 10 with respect to the fiducial cases. It is interesting to notice how this difference disappears in the second panel: cocoons with higher pressure will expand more slowly (see Figure 3.4) and thus (partially) compensate for this difference. For the same reason, models such as Kaiser and Alexander (1997) state their predictions for the pressure as a function of  $r_{HS}$  rather than  $t_{age}$ . Direct, quantitative comparison with these predictions would yet be of little significance and difficult to interpret, because of the different assumptions about the ISM density distribution.

Besides the trivial aforementioned density differences, all the curves decrease smoothly up to phase F; later, the rapid cocoon expansion in the 200p5 (dashed black line) runs makes its pressure turn down by two order of magnitudes in about 2Myr; much faster than the other ones. Density contrast and  $\sigma_V$  also play an important role, in concordance with the geometric properties described in the previous section. The general picture that we deduce is that a jet capable -for any reason- of building up a higher pressure, will result in a less elongated cocoon: the pressure, as expected, promotes isotropic expansion. In turn, a cocoon (the bow shock front, to be more precise) with a lower  $r_{HS}/r_C$  will need to move more gas from the ISM in order to inflate; thus it will expand more slowly.

The turbulent pressure fraction  $p_t/(p_t + p_g)$  is shown in Figure 3.6 (upper panel). During the first few tens of thousands years,  $p_t$  is very close to 25% of the total, in all the runs. Run 200p5 is again an extreme case, never showing signs of decay from this value. This can be explained in the following terms: for the consideration we

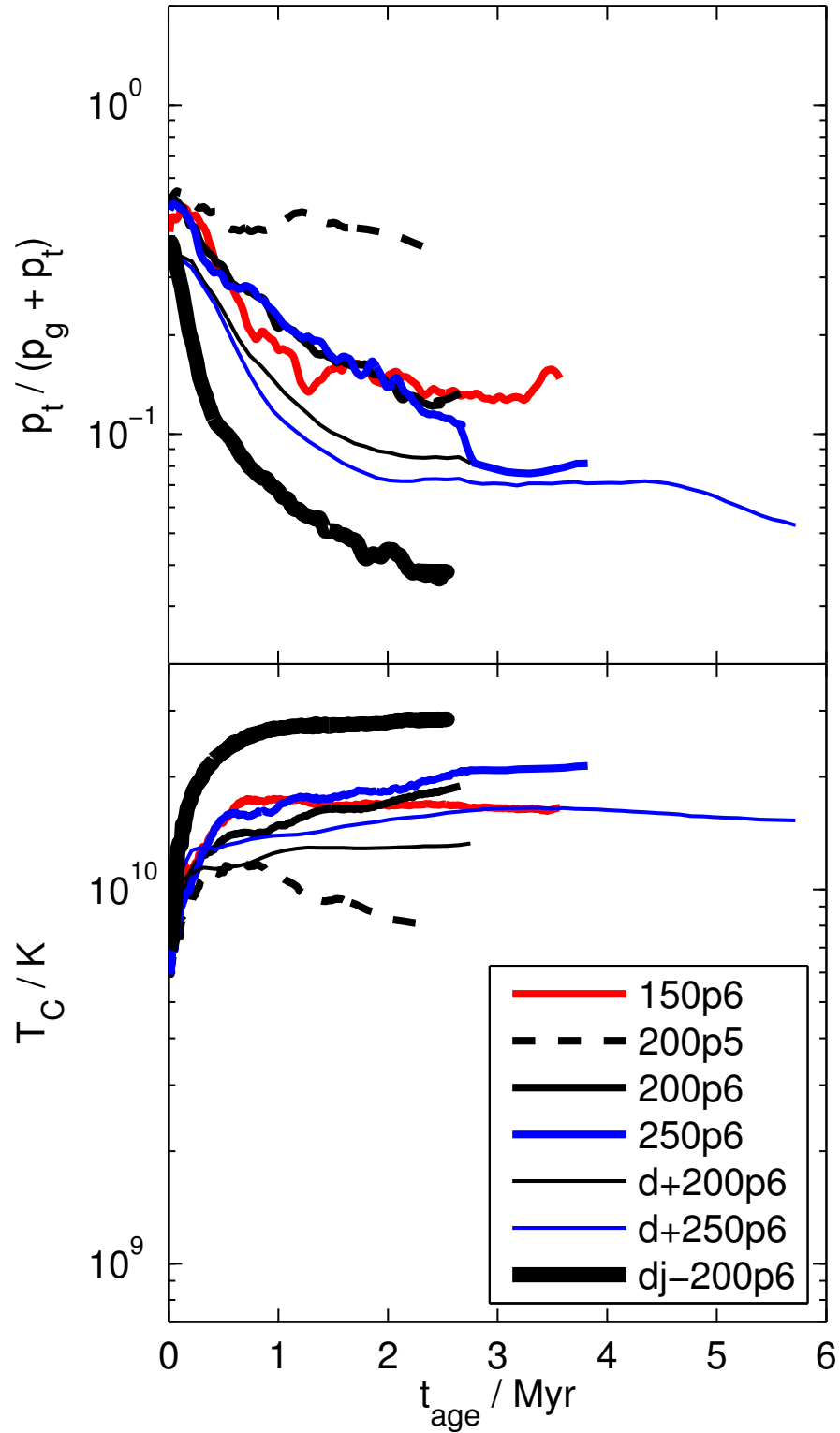


**Figure 3.6:** Thermodynamics of the cocoon ( $T > 2 \times 10^9$  K). **Plot style coding:** same color means same  $\sigma_v$ , same line style means same  $p_{jet}$ , while line thickness discriminates *fiducial* runs ( $\rho_{jet}/\rho_{halo}^c = 0.01$ ) from *enhanced density contrast* runs ( $\rho_{jet}/\rho_{halo}^c = 0.001$ ). **Upper panel:** Evolution of the turbulent fraction of the cocoon pressure  $p_t/(p_t + p_g)$ . **Lower panel:** Average cocoon temperature  $T_C$  as a function of time.

expressed in Section 3.2, a lower  $p_{jet}$  means a higher  $v_{jet}$ , so a higher shear inside the cocoon (compare runs in Figure 3.3), thus we can expect more turbulent motions. The fiducial runs (lines of intermediate thickness), are indistinguishable until 2.5 Myr. The *denser ISM* family converges to a little less than 10% after  $\sim 2$  Myr; in the light jets run the  $p_t$  fraction is already below 3% at that time. Almost all runs show, if not yet in complete convergence, that stability develops around these values.

The lower panel in 3.6 shows the time evolution of the average cocoon temperature  $T_C$ . Again, after a transition corresponding to phase C, all runs (except for 200p5) converge to some value in the range  $[1, 3] \times 10^{10}$  K, so that the jet-powered expansion is to a considerable extent an isothermal process. The actual convergence temperatures just reflect the thermodynamic state of the jet at injection. This convergence in both  $T_C$  and the  $p_t$  fraction means that some *self-regulation mechanism* is at work, stabilizing the turbulent pressure. Yet, this happens regardless of whether self-similarity in the expansion is achieved or not, while runs such as 200p5, undergoing fast expansion and thus relatively little interplay with the ISM, do not show such a convergence. So self-regulation appears more related to the interaction with the ISM, and all the complicated hydrodynamics therein (cocoon piercing, recollimation shocks, backflows; see Section 3.6), rather than to the geometry of the expansion, to which it is more often linked.

Finally, in Figure 3.7 we plot the energy exchanged between the cocoon and the ISM: the upper panel shows the *cumulative pdV* work of the cocoon  $W_C$ , while the lower panel likewise contains the  $TdS$  exchange of heat  $Q_C$ . The entropy  $S$ , here and in the following, is calculated as in Tooper (1969), by:

$$S = \rho \frac{N_A v k_B}{\mu} \ln \left( \frac{T^{1.5}}{\rho} \right)$$

where  $\mu = 0.5988$  is the mean molecular weight, while the temperature  $T$  and the density  $\rho$  are evaluated in each cell. Both quantities increase nearly linearly during phases F and L, so that the energy deposition, i.e. the essence of the feedback, is constant with time. The mechanical work  $W_C$ , that Antonuccio-Delogu and Silk (2008b); Tortora et al. (2009) associate to gas compression and ultimately to positive feedback, constantly outnumbers by an order of magnitude the exchanged heat  $Q_C$  (calculated as integral in the temperature/entropy state diagram), associated to the negative feedback. This also points to an early positive feedback in the innermost kpc (Tortora et al., 2009, Gaibler et al., 2012). Yet, the presence of cold gas and thermal conductivity may change this value significantly, so this must be taken as a lower limit.

Finally, the middle panel shows the ratio  $(W_C/t_{age})$  as a percentage of the injection power  $P_{jet}$  ( $P_{jet}$  is reported in Table 3.1); in other words, this quantity is the time average up to the instant  $t_{age}$  of the *jet/ISM energy coupling constant*. We notice that in these first few Myr, this is always within [3, 5]%; such values of coupling are believed to be very significant in the galaxy formation context (e.g. Sijacki et al., 2007a; Mocz et al., 2013).

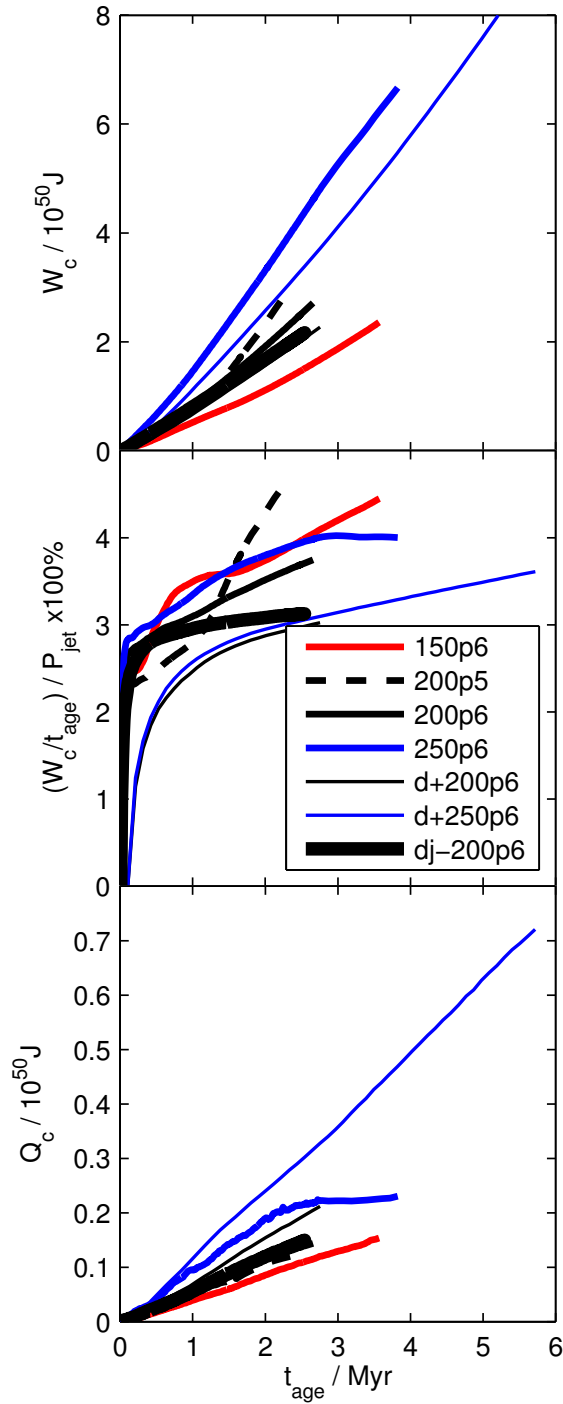


**Figure 3.7:** Mechanical  $pdV$  work  $W_c$  done by the cocoon expansion on the rest of the ISM (upper panel), (time-averaged) power developed by  $W_c$  as a percentage of the input power  $P_{\text{jet}}$  (middle panel) and  $TdS$  heat exchange  $Q_c$  as a function of time. The energies  $W_c$  and  $Q_c$  quantities are calculated as cumulative integrals in the cocoon volume-pressure and entropy-temperature diagrams, respectively. All values suggest that jet feedback is energetically significant even in the first Myr. **Plot style coding:** same as Figure 3.5.

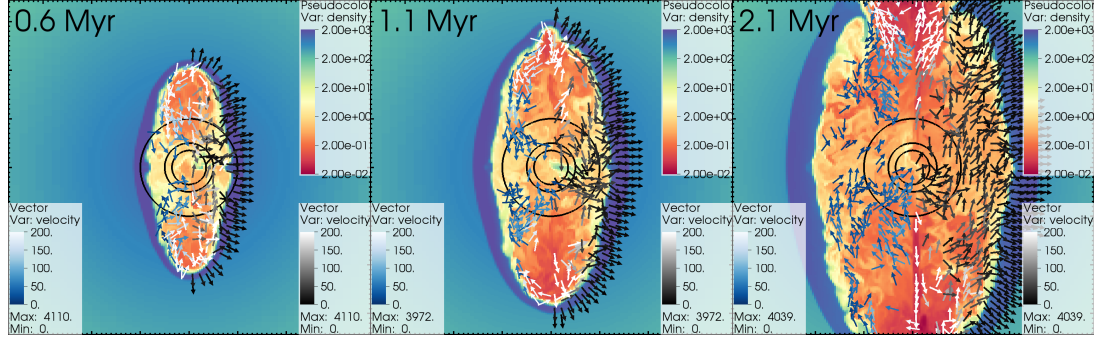


**Figure 3.8:** Central slices of run dj-250p6, at  $t_{age} = 0.6, 1.1$  and  $2.1$  Myr. Box size: 7 by 7 kpc. The background shows the gas density (pseudocolor plot). The arrows trace the velocity field  $\mathbf{v}$ . Left half (blue to white): backflow velocity only, i.e.  $\mathbf{v} \cdot \hat{z} < 0$ . Right half (black to white): projected expansion velocity on the x-y plane (i.e. where  $xv_x + yv_y > 0$ ). Contours at 0.35, 0.5, and 1 kpc distance from the centre are also shown as black circles.

## 3.6 Backflow

### 3.6.1 Overview on Backflow

Within the jet-cocoon system we can distinguish few flow structures with different (and time-varying) levels of regularity. Motion within the jet is mostly laminar, but Kelvin-Helmholtz instabilities along its path tend to produce turbulent eddies and may destabilize this flow. These turbulent eddies propagate within the cocoon and result in transonic turbulence.

Finally, we also observe a *backflow* within the cocoon. By this term we define a *spatially coherent* flow directed opposite to the jet itself. In all the runs we have performed, this backflow develops during the initial  $10^5 - 10^6$  years. This feature of jet-cocoon systems was already noticed in the first simulations of the propagation of relativistic jets into homogeneous atmospheres (Norman et al., 1982), and confirmed by more recent simulations (Rossi et al., 2008; Perucho and Martí, 2007).

Mizuta et al. (2010) distinguish backflows, according to their morphologies: a *straight* backflow, with flow lines extending from the tip of the hotspot back to the origin, and a *bent* one, where the flow lines are instead bent near the meridional plane. In their previous 2D simulations, Antonuccio-Delogu and Silk (2010a) also noticed the formation of these features, and noticed that the backflow turned from a *bent* to a *straight* morphology with evolving time.

As shown in Figure 3.8, a *straight* backflow arises during the early evolution of the cocoon (phase C and early phase F), spatially confined between the jet and the bow shock. Until about 0.6 Myr the backflow is coherently organised along streamlines extending almost continuously from the hotspots to the meridional plane, thus contributing to replenish the central accretion region and the disc with gas. However, the turbulence which develops within the cocoon acts to heavily perturb these backflows, and their large-scale coherence is completely destroyed after 2 – 3 Myr. In order to understand how much this backflow can affect the central SMBH, we plot in Figure 3.9 the evolution of the total gas mass and within a sphere of 1 kpc radius, centered at

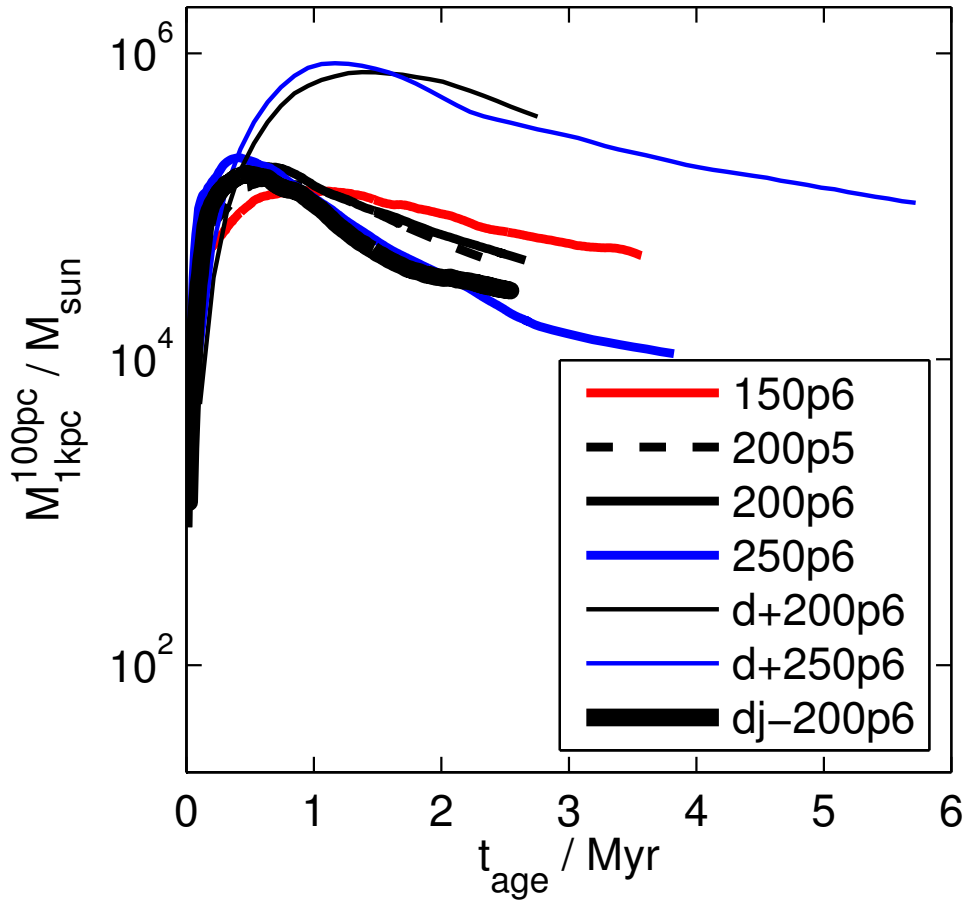


**Figure 3.9:** Total mass evolution around the central region of the jet-cocoon system. We compute the total mass within 1 kpc from the centre, excluding the central 0.1 kpc to avoid possible numerical contamination. We use our standard cocoon selection ( $T \geq 2 \times 10^9$  K) plus a density threshold ( $\rho \leq 4.23 \times 10^{-1} \text{cm}^{-3}$ ). In this way we eliminate from the computation both the central overdense region and the hot material from the jet. In the *fiducial* and the *light jets* runs, the increase in total mass during the first few  $10^5$  yr is mostly contributed by the backflowing gas converging towards the meridional plane. The same is true for runs from the *denser ISM* family (thin lines), but the mass increase is higher and peaks at later times. This is just due to the larger mass in the central region. **Plot style coding:** same as Figure 3.4.

the origin of the jet. We also remove the innermost 100 pc, that may introduce numerical error contamination (but gas accreted in the innermost kpc likely ends up in that region).

The backflow region is selected, besides the standard cocoon selection ( $T \geq 2 \times 10^9$  K), also by a density threshold criterion ( $\rho \leq 4.23 \times 10^{-1} \text{cm}^{-3}$ ), in order to select gas contributed from the backflow *but* not belonging to the jet. In all but the *denser ISM* runs, the mass accumulates from the innermost regions and proceeds towards the external regions, on time scales of  $t_{acc} \sim 10^5$  years, followed by a slower decrease ( $t_{age} \sim 2 - 3$  Myr).

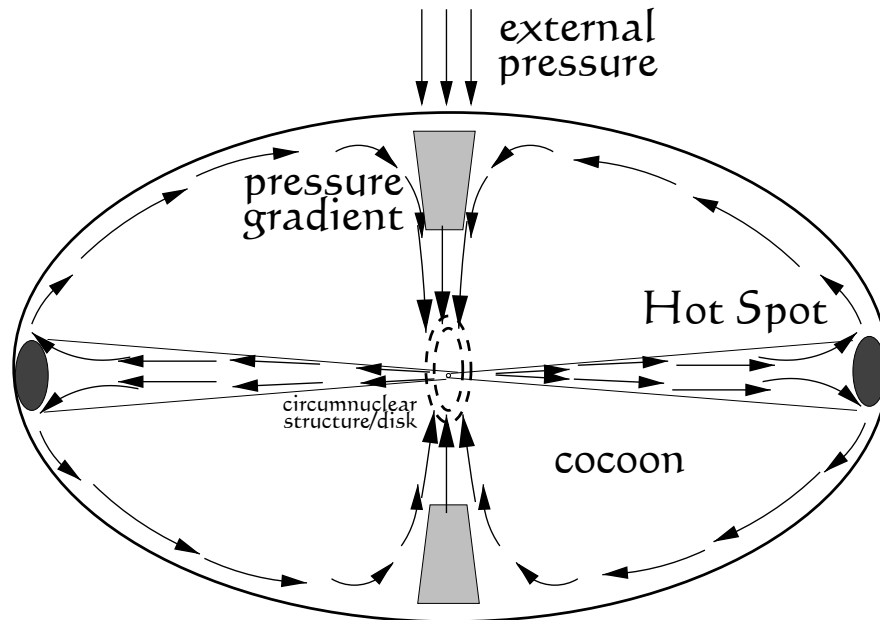
A maximum mass of  $0.8 - 2 \sim 10^5 M_{\odot}$  is accreted by the backflow, without any appreciable dependence of the time-scales of the backflow on either  $P_j$  or on  $\sigma_v$ , (i.e. on the global galaxy mass) for the *fiducial* runs. For those runs where the central density is

10 times larger (thin lines), we observe a similar behavior, except that the global mass of the backflow is correspondingly 10 times larger, and the decay time is longer ( $\simeq 1$  Myr). Thus, we conclude that the ISM density is the only parameter which determines the amount of gas which the backflow can drive back towards the SMBH accretion region.

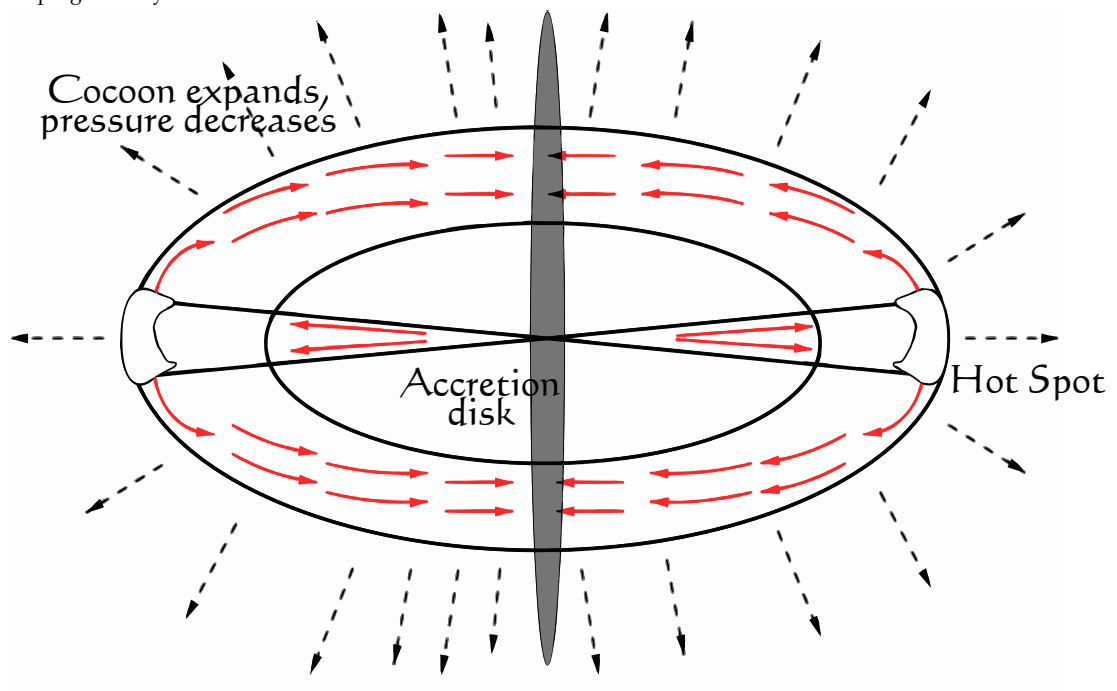
If we compare our backflows with the ones in Antonuccio-Delogu and Silk (2008b), we find that ours drive more gas to the central region during the first few  $t_{acc}$ ; later, they are still present, but only occasionally they reach the central region; indeed they propagate with ease for  $\lesssim 15$  kpc from the HS ( $\lesssim 5$  kpc for the enhanced density contrast runs), but fade after that distance.

In all the runs, we observe backflows reaching the central kpc for no longer than  $\simeq 2$  Myr, while the model predicts significant activity throughout the whole life of the jet/cocoon system. It is important to notice that the model was designed from the results of 2D simulations. The reason for this discrepancy is then to be found in the changes occurring when adding the third dimension. We propose three possible causes to account for backflow damping in 3D.

1. *Expansion dynamics* - In the model, the backflow originates from near the hotspot HS, from the jet gas which crosses the shock in the downstream region, due to the vorticity creation associated with the jump in the specific enthalpy (*Crocco's theorem*).  
The efficiency of this backflow in driving gas to the central region depends however on the expansion of the cocoon: if the velocity of the hotspot is larger than the average velocity of the gas flowing back, the latter will fade away. In addition to this, the expansion of the cocoon itself results in a decreased cocoon average density. The backflow/expansion interplay is sketched in Figure 3.10. In 3D, the volume expansion is faster, occurring in one more dimension. This is because those simulations were run in  $d/dz$  symmetry, in order to include a non-axisymmetric cold gas component. It will not be case in axisymmetry (2.5D simulations); for instance as in Walg et al. (2013), who study the cocoon morphology, too, though with a different equation of state for the gas.
2. *Large-scale vorticity* - In 3D, the gas has one more degree of freedom in its flows. So, the aforementioned vorticity on scales of the whole cocoon may result in more gas moving in the azimuthal direction rather than flowing back to the central plane, which is the only possible flow in 2D.
3. *Small-scale vorticity (Kelvin-Helmholtz instability)* - Coherent backflows give rise to shear, which eventually may lead to the rise of Kelvin-Helmholtz (KH) instabilities and thus turbulent vortexes. We investigate the stability of KH modes -and whether they can destroy the flow that generated them in our simulations- in Section 3.6.2. Once again, the third dimension is necessary for a correct description.



**Figure 3.10:** Model of backflow. Above: “classical” view of backflow, as in Antonuccio-Delogu and Silk (2008b). Gas circulation within the cocoon is internally dictated by pressure gradients, that push the gas back to the central region.  
Below: emerging view from 3D simulations (this work). As the cocoon expands laterally and pressure decreases, the outermost backflow streamlines are driven farther away and the material which they carry reaches the disc at progressively later times.



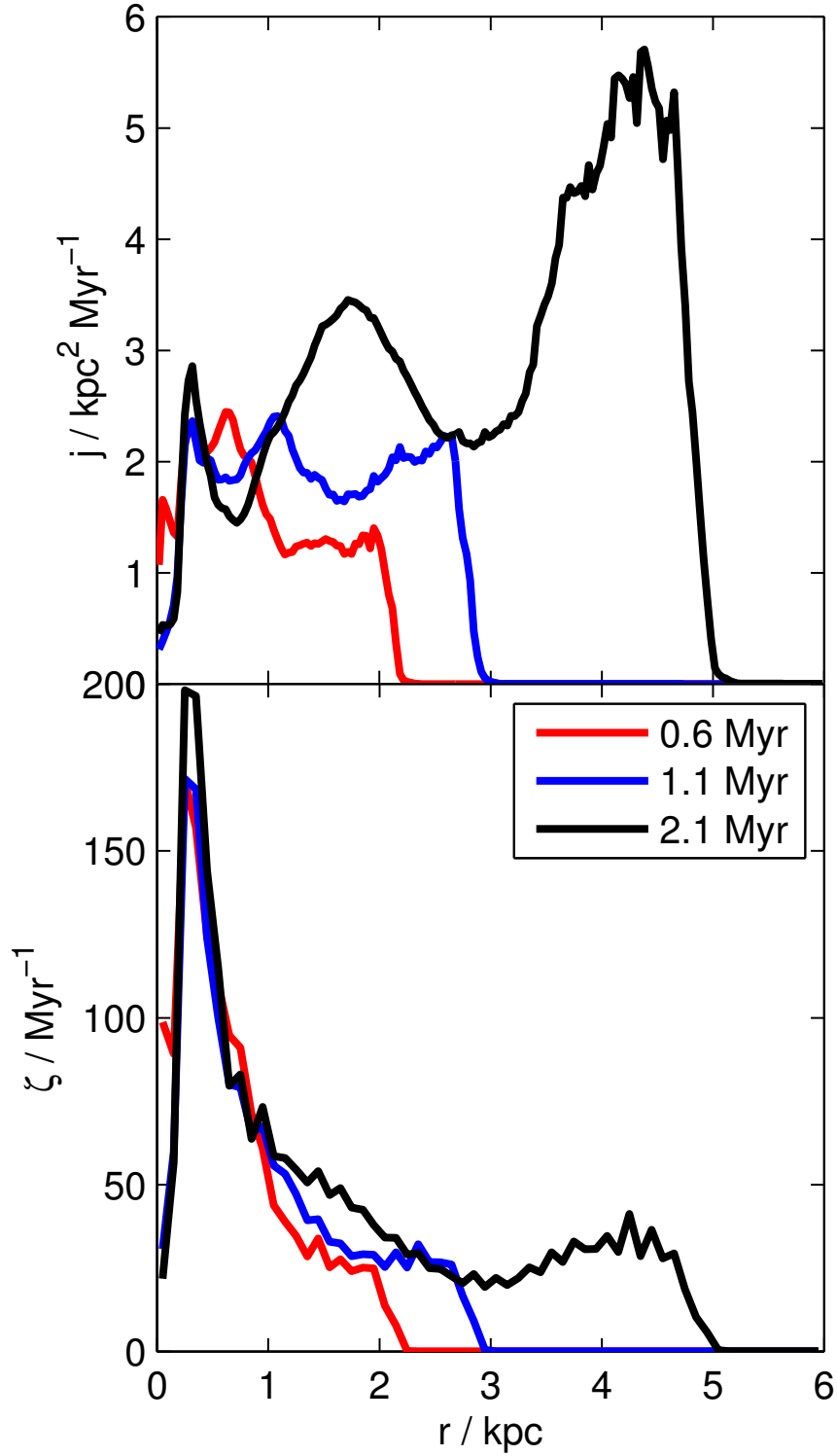


**Figure 3.11:** Magnitudes of specific angular momentum  $\mathbf{j} = \mathbf{r} \wedge \mathbf{v}$  and vorticity  $\boldsymbol{\zeta} = \nabla \wedge \mathbf{v}$ , in spherical bins for run dj-250p6, at  $t_{\text{age}} = 0.6, 1.1$  and  $2.1$  Myr; the snapshots are the same as Figure 3.8.

In order to test the first two options, in Figure 3.11 we plot the magnitude of the specific angular momentum  $\mathbf{j} = \mathbf{r} \wedge \mathbf{v}$  and the vorticity  $\boldsymbol{\zeta} = \nabla \wedge \mathbf{v}$  in spherical bins for run dj-250p6. No cocoon selection was applied this time. The three lines in the figure correspond to  $t_{age} = 0.6, 1.1$  and  $2.1$  Myr, i.e. the same snapshots as Figure 3.8.

Direct comparison with the latter figure is revealing: three separate peaks appear in  $j$ . The innermost one, always at  $\sim 0.3$  kpc, is dominated by the jet contribution (the jet has a cylindrical velocity profile, thus  $j$  becomes non-zero immediately when offset from the center), and it appears also in  $\zeta$ . The second one ( $0.7 - 1.9$  kpc) is consistent with the cocoon size, and locates the bulk of the backflowing gas. We can once again see how the backflows are relevant but can hardly reach the central region. The third peak in  $j$  ( $1.5 - 4.5$  kpc) has a more irregular and extended shape, suggesting its composite origin. Indeed, contributions from both the bow shock region and the HS are present. In the bow shock,  $j$  is simply consistent with (non-spherical) expansion, while the hot spot contains gas with high azimuthal velocities.

Similar information is provided by  $\zeta$ ; although the vorticity decays with distance from the center, a plateau of constant vorticity appears, suggesting structure on the same scales. Note that the average vorticity profile keeps constant with time, while the two outer peaks in the angular momentum distribution tend to increase their distance and magnitude. These peaks are associated with “rings” of highly rotating, shearing material, and it is interesting to note that these coherently rotating structures form as a consequence of the general circulation within the cocoon.

We end this overview section with some final consideration on the fate of the backflowing gas. It is true that, after about 2 Myr, the backflow is shut down; but we have shown that by that time a large amount of hot gas has been in the innermost 1 kpc. The final fate of this gas will depend on the dynamics of the cocoon. As is evident from Figure 3.8, the cocoon continues to expand laterally, and the gas advected in the meridional plane will follow this expansion. As long as this expansion lasts, most of this gas cannot settle into, e.g., a meridional disc. Our simulations lack sufficient spatial and temporal resolution to state whether a geometrically thin accretion disc may form around the SMBH.

However, if even a few percents of this advected gas mass can reach the innermost 100 pc (which is, again, likely yet hard to say from our results), it will ultimately contribute to raise the total amount of gas available for accretion onto the central BH. Thus, we argue that the gas in the meridional plane is likely to supply the accretion disc around the central BH, ultimately contributing to powering the jet itself.

### 3.6.2 Backflow stability

As we have previously noticed, in all the runs we have presented the backflow tends to disappear after some time. We have listed different physical mechanisms that can act to destabilize the backflow: here however we will focus our attention on the Kelvin-Helmholtz instabilities at the interfaces between the backflow and the bow shock on one side, the backflow and the jet on the other side. These interfaces are regions of very high shear, due to the negative velocity of the backflow w.r.t. both the jet and the

bow shock.

The dispersion relation for the linearised KH instability in a compressible fluid is given by Gerwin (1968):

$$\frac{x^2 - 1}{x^4} = a \frac{(x - m)^2 - b}{(x - m)^4} \quad (3.7)$$

where we have assumed a form:  $\exp i(kr - \omega t)$  for the perturbations and defined:  $x = \omega/c_s k$  and:  $m = V \cos \phi/c_s$  ( $V$  being the relative velocity between the backflow and one of the two interfaces, while  $\phi$  is the angle  $V$  makes with such interface, and  $c_s$  is the sound speed). The coefficients  $a$  and  $b$  are defined as:

$$a = \left( \frac{\Gamma_{blj}}{\Gamma_c} \right)^2 \left( \frac{c_c}{c_{blj}} \right)^2, \quad b = \left( \frac{c_c}{c_{blj}} \right)^2$$

and we have defined the polytropic indexes  $\Gamma_c, \Gamma_{blj}$  for the cocoon, bow shock and jet, respectively, as well as the sound speeds:  $c_c, c_{blj}$ .

The typical temperatures in the cocoon and in the jet exceed  $T \sim 10^{10}\text{K}$ , thus we will adopt for these regions a *relativistic* equation of state (EoS). More specifically, we adopt the fits to the multispecies relativistic EoS given by Chattopadhyay and Ryu (2009), so that the sound speed will be given by their eq. (5k):

$$c_{c,j} = c \left( \frac{2\Gamma\Theta}{f(\Theta|\xi) + 2\Theta} \right)^{1/2} \quad (3.8)$$

where:  $\Theta = kT/m_e c^2 \simeq 1.686 T_{10}$ ,  $T_{10} = T/10^{10}\text{K}$ ,  $f = e/(n_e - m_e c^2)$  is the scaled internal energy density, and  $\xi = n_{p+}/n_{e-}$  is the proton/electron density ratio. Chattopadhyay and Ryu propose an approximation for  $f$  (their eq. 5g), namely:

$$f = (2 - \xi) \left[ 1 + \Theta \frac{9\Theta + 3}{3\Theta + 2} \right] + \xi \left[ \frac{1}{\eta} + \Theta \frac{9\Theta + 3/\eta}{3\Theta + 2/\eta} \right] \quad (3.9)$$

Here  $\eta = m_{e-}/m_p \sim 5.44 \times 10^{-4}$ .

We look for an unstable mode by requiring that  $x$  in eq. 3.7 be purely imaginary:  $x = iw$ . Thus the left-hand side becomes real:  $(w^2 + 1)/w^4$ . The right-hand side is instead a complex expression, thus, requiring that its imaginary part be zero we arrive at the following equation:

$$mw [(m^2 + w^2)^2 + (m^2 - w^2)(1 - 3b) + 2b^2] = 0 \quad (3.10)$$

We are not interested into the trivial neutrally stable solution  $w = 0$ , thus we turn our attention to the term in square parentheses. By defining the reduced variable  $q = w^2$  we finally obtain a reduced dispersion relation:

$$q^2 + [3b - 1 + 2m^2] q + [2b^2 - (3b - 1) m^2] \geq 0 \quad (3.11)$$

The discriminant of this equation must be positive to obtain real solutions:

$$\Delta = (3b - 1)^2 + 8m^2(3b - 1) + (4m^4 - 8b^2) \geq 0 \quad (3.12)$$

and in order to have at least one positive root one of the two following inequalities has to be satisfied:

$$\Lambda_1 = 3b - 1 + 2m^2 \leq 0, \quad \Lambda_2 = 2b^2 - (3b - 1)m^2 \leq 0 \quad (3.13)$$

We will now consider separately the two interfaces: cocoon-bow shock and cocoon-jet. The bow shock has relatively higher densities w.r.t. both the cocoon and the jet, and  $T \lesssim 10^8$  K, thus  $\Theta \ll 1$  and we can adopt a classical EoS:  $p = \mu n k_B T$ , with  $\mu \sim 0.62$  being the mean molecular weight of a fully ionized plasma of solar composition. In the bow shock we will then have:  $\Gamma_b \sim 5/3$ ,  $c_b = (k_B T)^{1/2}$ .

Temperatures within the cocoon are instead larger than in the bow shock ( $T_c \gtrsim 10^9 - 10^{10}$  K), thus the coefficient  $b = (c_c/c_b)^2 \gg 1$ , and we see that the discriminant from eq.3.11 is positive:  $\Delta \sim b^2 \geq 0$ . In the same limit we also have:  $\Lambda_1 \approx 3b + 2m^2 \geq 0$  and  $\Lambda_2 \leq 0$  for  $m^2 \gtrsim 2b/3$ , i.e.:  $V \gtrsim c_c^2/c_b$ . Thus, the interface between the bow shock and the backflow can be unstable only for very large backflow velocities, largely exceeding the sound speed within the cocoon. One more empirical argument in this direction is that any shear between backflow and bow shock region is severely damped by the cocoon expansion, simply because it takes gas far away (i.e.  $\phi = 90^\circ$ ).

On the other hand, at the interface between cocoon and jet, for the coefficient, we have  $T_j \sim T_c$ , thus we have to inspect in detail the region of integrability of the above inequalities (eqs. 3.12 and 3.13).

In Fig. 3.12 we show the regions where inequalities 3.12 and 3.13 are satisfied, together with the behavior of run dj-250p6, the same as in Figure 3.8, for the same  $t_{age}$  shown therein, namely 0.6, 1.1 and 2.1 Myr. The error bars represent intrinsic scatter inside backflow streams (this is visible in Figure 3.8, too).

We see that there exists a wide region of the plane  $(b, m^2)$  where  $\Delta \geq 0$  and  $\Lambda_2 \leq 0$ . Here, there is a real positive solution  $q$  for eq.3.11, and consequently a real value of  $w = \pm q^{1/2}$  are allowed. So being in this region would imply the existence of at least one unstable mode, where the frequency is purely imaginary:  $\omega = -iq(c_s k)$ .

As expected, the bent backflow (open glyphs in Fig. 3.12) appears largely KH stable, for the reasons stated above (low values of  $m^2$ ). It is more interesting to notice that the straight backflow is stable too; this means that the jet material is so much hotter and less dense than the cocoon, that this difference prevails for the velocity gradient (small  $b$ ).

We conclude that the reason for the backflow stopping is not to be found in KH instabilities. The *push* this gas is given in the HS is sufficient for it to travel backwards for a few tens of kpc, then eventually it gets lost in the 3D large-scale vorticity or fades while expanding with the cocoon (as we pointed out in Section 3.6.1).

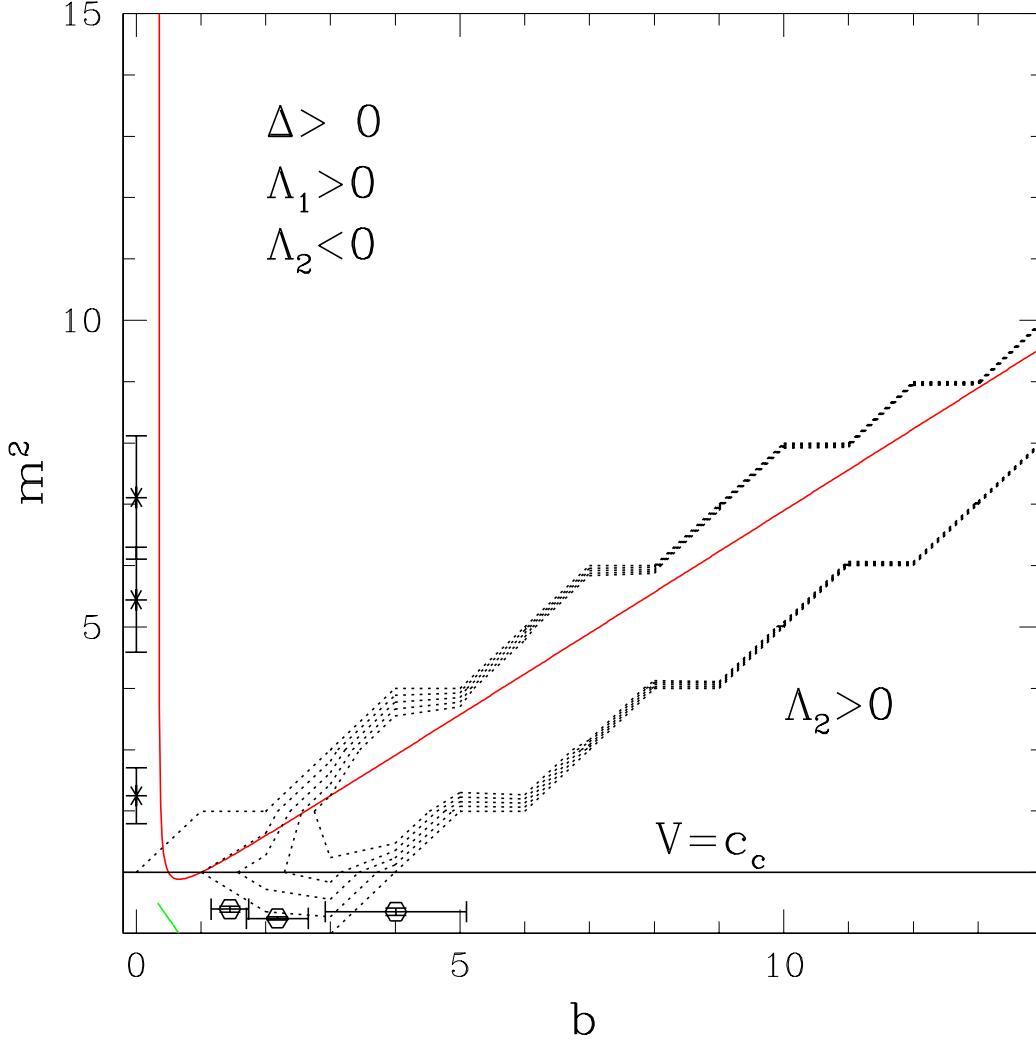


**Figure 3.12:** Conditions for existence of unstable K-H modes. The dotted contours represent values of the discriminant  $\Delta = 10, 16.62, 23.23, 29.85, 36.46$  (from the outermost contour inward). The continuous curve discriminates the regions in the plane  $(b, m^2)$  where the coefficient  $\Lambda_2$  of eq.3.11 changes sign. In the region where the discriminant  $\Delta$  is positive and  $\Lambda_1 > 0, \Lambda_2 < 0$  there exists real solutions of the dispersion relation. The points represent the behavior of run dj-250p6, and correspond to the same snapshots as Figure 3.8. Error bars represent intrinsic scatter in the gas streams. Both the *straight* (starred points) and the *bent* (open glyphs) backflow fall in the stable area.

### 3.7 Discussion

We have performed a series of 3D hydrodynamical simulations of bipolar jets from AGNs, covering the first few Myr of the evolution of this object. Our main aim was to study the transition stage from a compact central source (such as the *Compact Steep Spectrum* sources, *CSSs*, or the *Gigahertz Peaked Spectrum* sources, *GPSs*) to an extended *Fanaroff-Riley type two* (FR II) galaxy. We have studied the geometrical and thermodynamical properties of the extended *cocoon* produced during the propagation of a relativistic jet within the ISM of its host galaxy. Inspired by recent work (Silk, 2013), we have explored the consequences of varying the internal jet pressure  $p_{jet}$ , together with

its density contrast  $\rho_{halo}^C / \rho_{jet}$  and the central velocity dispersion  $\sigma_V$ , which in turn sets the (average) halo mass and virial radius, the SMBH mass and the jet power  $P_{jet}$ .

Our main results may be summarized in the following points.

1. We were able to follow the evolution of compact AGNs into extended sources, distinguishing three main evolutionary stages (see Figure 3.2): cocoon formation (phase C), forward propagation (phase F), and lobe expansion (phase L), when the jet eventually breaks free from the cocoon that confines it. We have highlighted the connections of the expansion history to the system's internal dynamics, especially to the jet piercing its own cocoon after a few Myr. When this happens (or not long after), the jets develop extended lobes, thus turning from a compact to an extended source, while the cocoon (now damaged) is still confined to the innermost 5-10 kpc.

Indeed, any supersonic jet run for long enough will eventually break through its cocoon, since the latter is expanding at the speed of sound; it just has to recover the delay accumulated in phase C (when the cocoon was already expanding but the jet was not advancing). It is however possible that the central engine is switched off before this happens; but this scenario will be different -for instance- from FRI sources, because not only the HS, but also the jets will fade and start mixing with the surrounding gas.

2. We have studied the thermodynamic state and the energy balance of the jet/cocoon system in a realistic hot ISM environment. The expansion is always to a large extent an isothermal process, with the mean cocoon temperature  $T_C$  rapidly converging to  $1-2 \times 10^{10}$  K. The turbulent pressure  $p_t$  always converges to about 10-20% of the cocoon total pressure, thus being dynamically significant in the long term. This happens regardless of the expansion history (mainly, independently of whether self-similarity is reached or not), thus pointing to some *self-regulation mechanism* dependent more on the cocoon's internal dynamics than on the geometry of the expansion.

The energy deposition in the ISM (in the form of  $pdV$  work and  $TdS$  exchanged heat) always, after phase C, remains in the interval 3-5% of the input mechanical power  $P_{jet}$ . Such values of this *energy coupling constant* are believed to be very significant in the galaxy formation context (e.g. Sijacki et al., 2007a; Mocz et al., 2013; Gaspari et al., 2012a).

3. Even though our simulation setup does not allow for testing different physical compositions of the jets, the results are sensitive to the ISM/jet density contrast. In particular, we have analyzed the cocoon geometry and expansion. We have found the cocoon's shape to be more elongated, in order of importance, for higher density contrast, higher  $p_{jet}$  and higher  $\sigma_V$  (Figures 3.3 and 3.4). Very light jets ( $\rho_{halo}^C / \rho_{jet} = 1000$ ) show overall more regular shape and slower expansion. Their shape evolution during the expansion is more likely to reach a self-similar phase (constant axis ratio), so in this sense not very elongated cocoons which undergo self-similar expansion favor lighter jets. A low injection

pressure  $p_{jet}$  may instead result in very little AGN/ISM coupling, giving rise in a few Myr to very large lobes.

4. We have shown the presence of significant *backflows*, i.e. gas circulation within the cocoons that is able to drive hot gas to the central kiloparsec. Such backflows are the product of the interaction between the jet and the local host galaxy's environment, and their contribution to the *Advection Dominated Accretion Flow* (ADAF) on to the central BH demonstrates that a connection between *galaxy-scale feedback* and *central accretion* develops over time-scales of the order of  $\sim 10^5$  years,  $\lesssim 1/10$  of the AGN duty cycle. This *backflow accretion* time-scale is much smaller than that suggested by 2D models (Antonuccio-Delogu and Silk, 2008b), due to the different cocoon expansion rates and behaviour of *large-scale vorticity* in 3D. We investigated the possible rise of Kelvin-Helmholtz instabilities, but found that backflows have insufficient shear to be unstable.

Though the accretion timescale we find may seem small, it only refers to the typical time for the backflow to feed the ADAF, which by that time may have accreted, as we find, up to  $2 \times 10^5 M_{\odot}$  of gas. This phenomenon thus points to a deep connection between AGN feedback and SMBH accretion, as previously hinted by Narayan and McClintock (2008). Finally, we notice that observational evidence for backflows has also been recently found by Laing and Bridle (2012) for two Fanaroff-Riley type I sources.

---

## Long-term Evolution of the Jet/ISM System <sup>1</sup>

---

After shedding light on the early evolution of AGN jets, in this chapter we aim to probe larger spatial scales and longer times. Jets from observed radio galaxies can extend for several hundred kiloparsec, and have lifetimes of order a billion years. We would like to calculate the energy balance of those systems throughout their whole life, in order to better understand:

1. the total amount of heat the jets can deposit in the host galaxy,
2. whether and for how long jets are able to delay catastrophic cooling (Section 1.3.1),
3. whether simulated galaxies develop the same structures we observe in radio galaxies.

Concerning the last point, we mainly refer to the giant *X-ray cavities* or *bubbles*, typically observed in large system (e.g. clusters and superclusters), but not exclusively.

One very famous -and puzzling under more than one aspect!- example of cavities is given by the *Perseus cluster*. In Figure 4.1 we show a very high resolution X-ray view of its center, by the *Chandra X-ray observatory*.

This source shows several series of cavity pairs, ultimately generated by the jet activity (a bipolar jet event for each bubble pair). It is very instructive to study the cavities' properties, formation and eventually disruption from simulations. If not else, because the "pdV" work done by the jets to inflate them is one of the most reliable indicator of jet power, as mentioned in Section 1.2.1. Moreover, they are expected to contribute largely to the heating of large scale gas (Section 4.3).

---

<sup>1</sup>This work is to be promptly submitted.

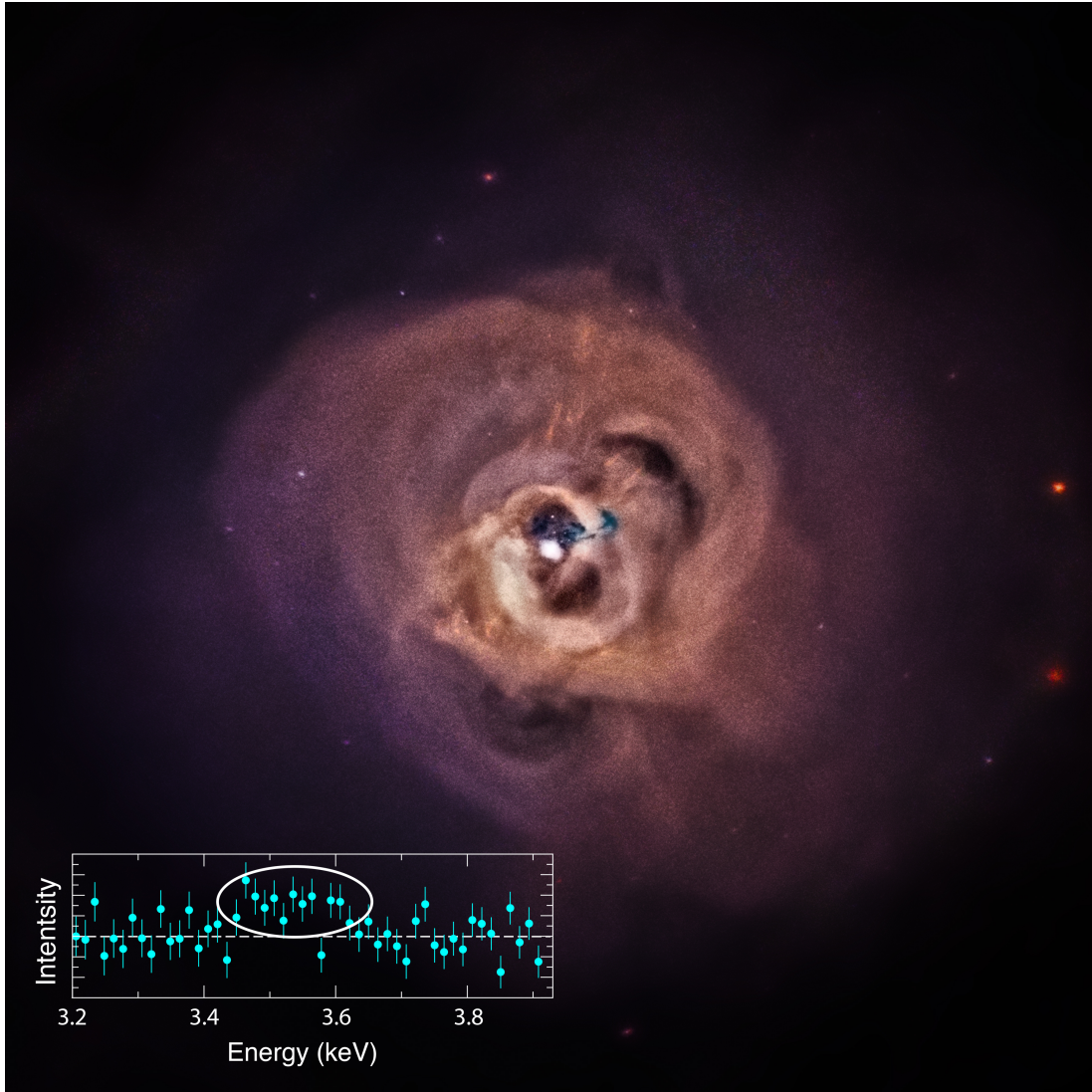


**Figure 4.1:** Recent, very high resolution view of the Perseus Cluster by the Chandra X-ray observatory. Note the several families of cavity pairs, likely generated by central jets. Extra feature: in the lower-left corner a mysterious spectral highlight of this source is shown. This emission feature at 3.5 keV may correspond to no known atomic emission line (Bulbul et al., 2014), and has been interpreted by some as a signature of *Dark Matter*. Credit: NASA.

Thus, in this chapter we present new jet simulations, run for cosmologically relevant times. We focus on the energy balance of the jet/halo systems, extending at later times the findings of Cielo et al. (2014, henceforth C14), essentially Chapter 3 of this thesis. In Section 3.2 we describe our updated setup, our simulation pool and the evolution of a typical run. In Section 4.2 we discuss the jet/ISM energy coupling, while in Section 4.3 we examine the ISM volume fraction heated by the jets and the hot gas bubbles they are actually capable of forming at later times.

## 4.1 Setup and simulation description

Our simulations are run with the FLASH hydrodynamical code (Fryxell et al., 2000). The setup we adopt is an upgrade of the one used in Cielo et al. (2014, henceforth C14) (Section 3.2; see also Section 2.4). The changes introduced since that work include the usage of FLASH’s split *Piecewise Parabolic Method* (PPM) hydro solver, the addition of the gas’ self-gravity on top of the dark matter’s one, and a modest metal content enhancement in the radiative cooling function ( $[\text{Fe}/\text{H}] = -1.0$ ). Finally, we adopt a larger simulation box (640 kpc) in order to encompass the dark matter halo’s radius  $R_{200}$ , which is defined as the radius encompassing a density 200 times larger than the Universe critical density.

The initial gas profile still uses the same model of a spherically symmetric gas distribution, at a constant temperature  $T_0$  and in hydrostatic equilibrium with the external gravity. Following McCarthy et al. (2008), we normalize the profile so that the ratio of gas to dark matter mass within  $R_{200}$  is 0.85 times the cosmic baryon fraction (taken from Komatsu et al. 2011). Our halo features  $R_{200} = 0.25$  Mpc,  $M_{200} = 1.71 \times 10^{12} M_{\odot}$  and a concentration parameter  $c_{200} = 7.8$  (Dutton and Macciò, 2014).

We perform two series of runs, changing the halo gas temperature. The gas density profile is quite sensitive to this parameter, giving rise to qualitatively opposite behaviors:

**The FC series** (for Fast Cooling) features a gas initial temperature  $T_0 = 1.60 \times 10^6$  K and a central density matching the ones in Capelo et al. 2010. The halo has an inner cooling time of order 100 Myr, and its *cooling radius*  $r_{\text{cool}}$  - the radius within which the cooling timescale is relevant for galaxy formation<sup>2</sup> - is 45 kpc. In the reference run with no Jet (F00) the gas cools all the way down to a few thousand Kelvin in about a hundred millions of years.

**The SC series** (for Slow Cooling) is a control series, with a higher initial temperature  $T_0 = 5.19 \times 10^6$  K. This choice of  $T_0$  implies a very shallow initial density profile, with a cooling time of order of the *Hubble time*. The aim of the SC series is to mimic the behavior of a halo in which other feedback mechanisms may have already heated the gas to temperatures much higher than the halo’s virial temperature (e.g. Diehl and Statler, 2008; Pellegrini, 2011). The gas density profile in the SC runs is marginally consistent with observations and it mainly represent an extreme case in which the gas is practically not cooling.

In both cases, we use a maximum refinement level  $l_{\text{ref}} = 10$ , which with our box of 640 kpc grants a resolution of 156 pc. We follow the evolution of the system for timescales of cosmological interest, up to  $t_{\text{max}} \sim 600$  Myr.

Rather than scaling the jet power  $P_{\text{jet}}$  with the black hole mass  $M_{\text{BH}}$  as in C14, we test the effects of varying  $P_{\text{jet}}$  in the range  $10^{42} - 10^{44}$  erg/s. For our halo mass, this

<sup>2</sup>Our exact working definition is: the radius within which the timescale for radiative cooling is smaller than the free-fall time.

brackets the expected Jet power (Fanidakis et al., 2012). Each value of  $P_{\text{jet}}$  is characterized by a typical jet injection time  $t_{\text{on}}$ , after which the jet source is switched off. As an estimate of  $t_{\text{on}}$  we take the synchrotron age of observed radio sources, from Parma et al. (1999).

Finally, in order to model the FRI/FRII dichotomy of the observed radio sources (Owen and Ledlow, 1994; Bicknell, 1995; Perucho et al., 2014a), we assign a lower (internal) jet Mach number  $\mathcal{M}_{\text{jet}}$  to the low-power runs ( $10^{42} - 10^{43}$  erg/s), keeping the high-power ones hypersonic. We tested that -at a given power- differences in  $\mathcal{M}_{\text{jet}}$  are a second-order effect (Cielo et al. in preparation). The parameters of all the different runs are displayed in Table 4.1.

In Figure 4.2 we show the evolution of run FC42 (left column) and SC42 (right column);  $10^{42}$  erg/s is what we expect to be a typical jet luminosity from the radio luminosity function (Sadler et al., 2002; Best et al., 2005); in this sense FC42 is our most representative run, while FRII are quite rare (van Velzen et al., 2014). All runs present the same evolutionary stages described in C14, namely (i) Cocoon creation, (ii) Forward propagation and (iii) Lobe inflation.

After  $t_{\text{on}}$  -when the jet is switched off- the lobes, no more powered by the central engine, turn into roughly ellipsoidal, under-dense, hot bubbles ( $T = 10^8 - 10^9$  K). Such bubbles start to rise due to gravitational buoyancy; at the same time they cool by radiation (mostly via bremsstrahlung processes) and mix with the external medium by turbulent instabilities. The bubbles are more extended and sharply marked in the SC case, while in the FC run a chimney of hot gas connects them to the halo center for a few hundreds Myr more, and they do never extend past 25 kpc. But if  $P_{\text{jet}}$  is increased, sharper bubbles form even in the FC case, and tend to have a more spherical shape. See Section 4.3 for a discussion on the bubbles' fate.

## 4.2 Energy coupling with the halo gas

The top panel of Figure 4.3 shows the evolution of the total energy of the system as a function of time for different jet injection powers. The total energy  $E_{\text{tot}}$  is defined as kinetic + thermal + potential energy of the halo gas, and it is calculated by summation on the simulation volume *within the halo cooling radius*  $r_{\text{cool}} = 45$  kpc, in order to highlight the effects on just the gas that the jet is "required" to heat (or to prevent from cooling).

In the no-Jet case (FC00) the total energy decreases as function of time, as a consequence of cooling and of the inflow of gas towards the center. For a jet of low (but common) power as FC42, the behavior is not very different, with a constant decrease of the total energy as function of time, with just a delay of few Myr with respect to the FC00 run. More powerful (but more rare) jets as FC43 and FC44 are instead able to halt cooling and, in the case of FC44, to substantially heat the gas.

In order to better understand the effect of the jet, it is interesting to look at the energy coupling between the jet and the ambient gas. We define the energy coupling

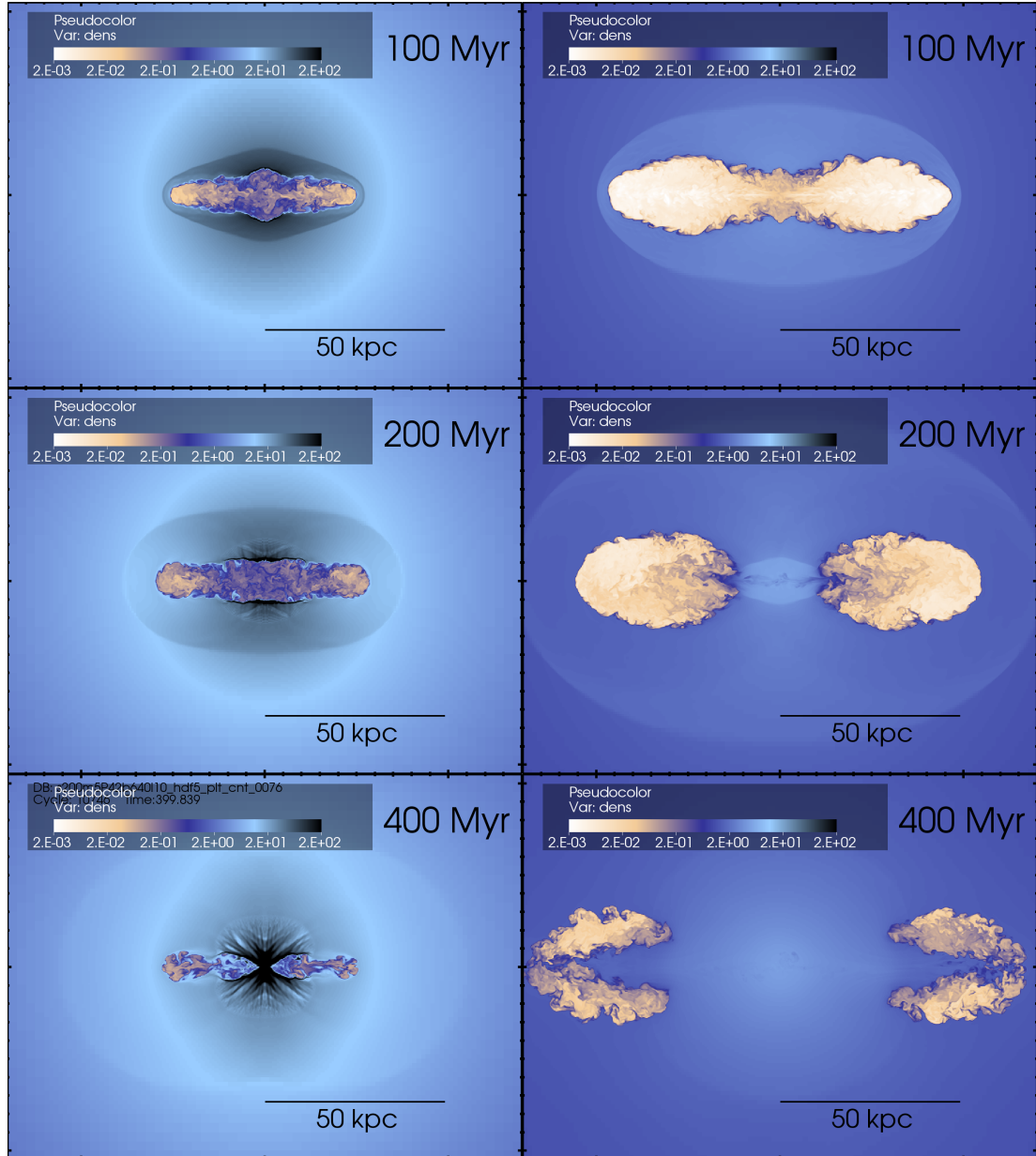


**Figure 4.2:** Central plane slices of the FC42 (left) and SC42 (right) runs. The color coding shows the gas density (internal units). The snapshots are taken at 100, 200 and 400 Myr, roughly corresponding to the different stages: jet immediately after switch-off (top), bubble formation (middle), bubble destruction (bottom). The bubbles originate from the jet lobes, after  $t_{\text{on}}$ , when the jets are turned off. At later times, one can see the bubbles fade due to radiative cooling and turbulent mixing (SC42), or being dragged back to the central region by infalling cold gas (FC42).

**Table 4.1:** Parameters and timings for all the simulation runs.

Name	$P_{\text{jet}}$ [erg/s]	$\mathcal{M}_{\text{jet}}$	$t_{\text{on}}$ [Myr]	$t_{\text{max}}$ [Myr]
<i>Fast Cooling series</i>				
FC00	jet off	N/A	0	550
FC42	$10^{42}$	5	79	480
FC43	$10^{43}$	5	42	380
FC44	$10^{44}$	20	21	180
<i>Slow Cooling (control) series</i>				
SC42	$10^{42}$	5	100	605
SC43	$10^{43}$	5	42	190
SC44	$10^{44}$	20	16	35

Run name, jet kinetic input power, jet internal Mach number, time after which the jet is switched off, total simulation time.

constant  $f_E$  as

$$f_E(t) := \frac{E_{\text{tot}}(t) - E_{\text{tot}}^{00}(t)}{E_{\text{jet}}(t)}, \quad (4.1)$$

where  $E_{\text{tot}}^{00}(t)$  is the total energy of the same halo in a run with no jet (FC00) and  $E_{\text{jet}}(t)$  is the cumulative energy injected by the jet up to the time  $t$ .

This coupling constant  $f_E$  describes the net energetic effect of the jet on the halo, and its evolution is shown in the bottom panel of Figure 4.3. Right after  $t_{\text{on}}$ , the coupling sets to a value of a few percent for all the runs, being slightly higher for higher values of  $P_{\text{jet}}$ . Theoretical arguments by Nulsen and McNamara (2013) indeed agree in that the thermal coupling depends critically on  $P_{\text{jet}}$ , though they suggest it might be more effective for larger halos such as the ones hosting galaxy clusters. Please note that  $f_E$  is rescaled to the jet input energy, so our findings mean that the actual energy transfer is indeed much larger for larger jet power. However, we have already remarked in Section 3.2 that the more powerful FR II events are much less likely to occur.

Later, the coupling constant for the FRI runs grows up to about 10% around 400 Myr. This increased distance from the run with no jet is not due to gas heating of some sort, but just to run FC00 entering the runaway cooling stage. We are basically measuring the difference between two thermal instabilities shifted in time. The FC42 run is long enough for most of the central gas to cool all the way down our cooling table. This happens around 400 Myr, and then  $f_E$  starts to decrease again. The FC43 and FC44 runs show a similar behavior as FC42: an initial peak in the coupling constant followed by a plateau lasting several Myr. Despite the minor differences we have

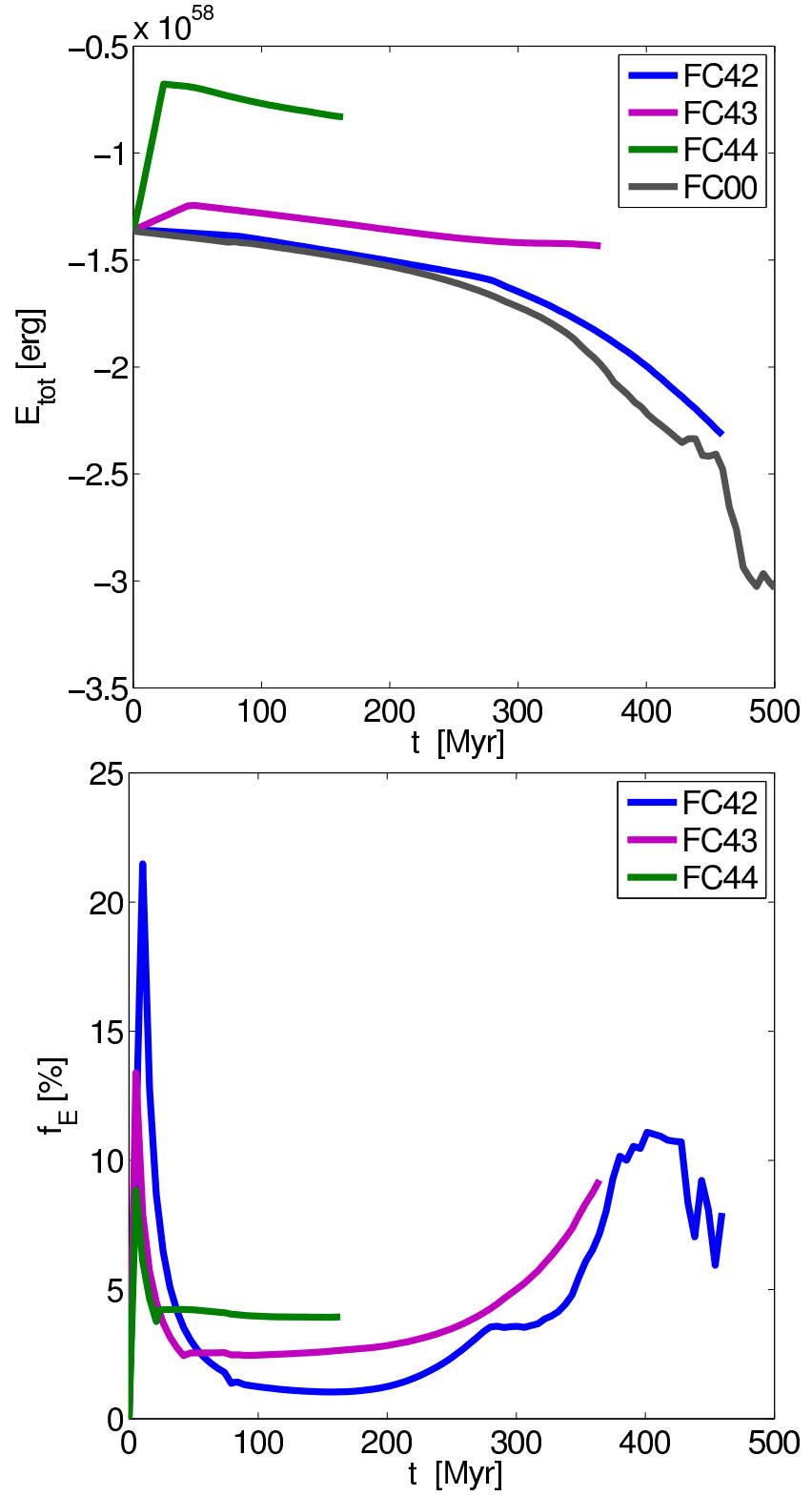


**Figure 4.3:** Evolution of the gas total energy (top) and energy coupling constant (bottom), calculated within the halo cooling radius ( $r_{\text{cool}} = 45$  kpc) for the runs in the FC series. Line colors mark the jet power  $P_{\text{jet}}$ , as indicated by the key.

highlighted, the coupling constant seems to have a very weak dependence from the jet power and always be of the order of few percent, in agreement with the findings of C14.

### 4.3 Hot bubbles and volume coverage

We now want to turn our attention to *where* the jet energy is deposited. After the jet is turned off, the (giant) hot bubbles are the main vector for hot gas to reach large radii. These bubbles are believed to take part in the heating/cooling balance of gas in the Circum-Galactic Medium (CGM), especially for large galaxy clusters (Babul et al., 2002; Croston et al., 2013).

At the same time, virtually all semi-analytical models invoke bubbles as a mechanism to propagate the AGN energy to large distances (most often without explicitly modeling this process), for practically all halo masses above  $10^{12}M_{\odot}$ . The idea behind this paradigm is that these bubbles may halt gas accretion onto the halo center, which otherwise would trigger high levels of star formation, preventing the formation of quiescent, massive red galaxies (e.g. Vogelsberger et al., 2013).

In Figure 4.5, we show the gas volume fraction within  $r_{\text{cool}} = 45$  kpc that has been heated by the jet, i.e. for which now the cooling time  $t_{\text{cool}}$  is larger than the free-fall time  $t_{\text{ff}}$ .

We name this quantity the *volume covering factor*  $f_V$ :

$$f_V := \frac{V_{r_{\text{cool}} > t_{\text{ff}}}}{\frac{4}{3}\pi r_{\text{cool}}^3}. \quad (4.2)$$

We calculate  $f_V$  also for the SC runs within 45 kpc, but with a caveat: the  $t_{\text{cool}}/t_{\text{ff}} > 1$  criterion does not apply because of the extremely long cooling time in the SC halos; as a consequence, we had to increase to 100 this threshold in order to have a robust selection of an analogue region.

At  $t = 0$ ,  $f_V$  is identically zero due to the definition of  $r_{\text{cool}}$ . The volume coverage of the run FC42 barely exceeds 1% at its peak, only to drop down again after another  $\sim 100$  Myr. The jet in this case is confined by the halo density central peak, and is never able to break out. After  $t_{\text{on}}$  the hot gas is dragged back to the center, as described in Section 4.2. This behavior is not present in the SC42 run, in which the jet is not so efficiently confined and  $f_V$  peaks at about 7%. Qualitatively, this is also what happens in the runs FC43 and SC43.

In all the FRI runs but FC42 the bubbles manage to expand and rise due mainly to buoyant forces (but also weak shocks may still play a role, see Perucho et al., 2014a). In the FC43 run the bubbles are still confined within the cooling radius at the end of the simulation ( $\sim 400$  Myrs). Despite the presence of this large amount of hot gas, strong cooling is meanwhile restarting around the jet chimneys (dark regions in Figure 4.4, top panel). These results imply that a FRI-like jet is able to heat the halo center only for short times and cannot balance cooling on long time scales.

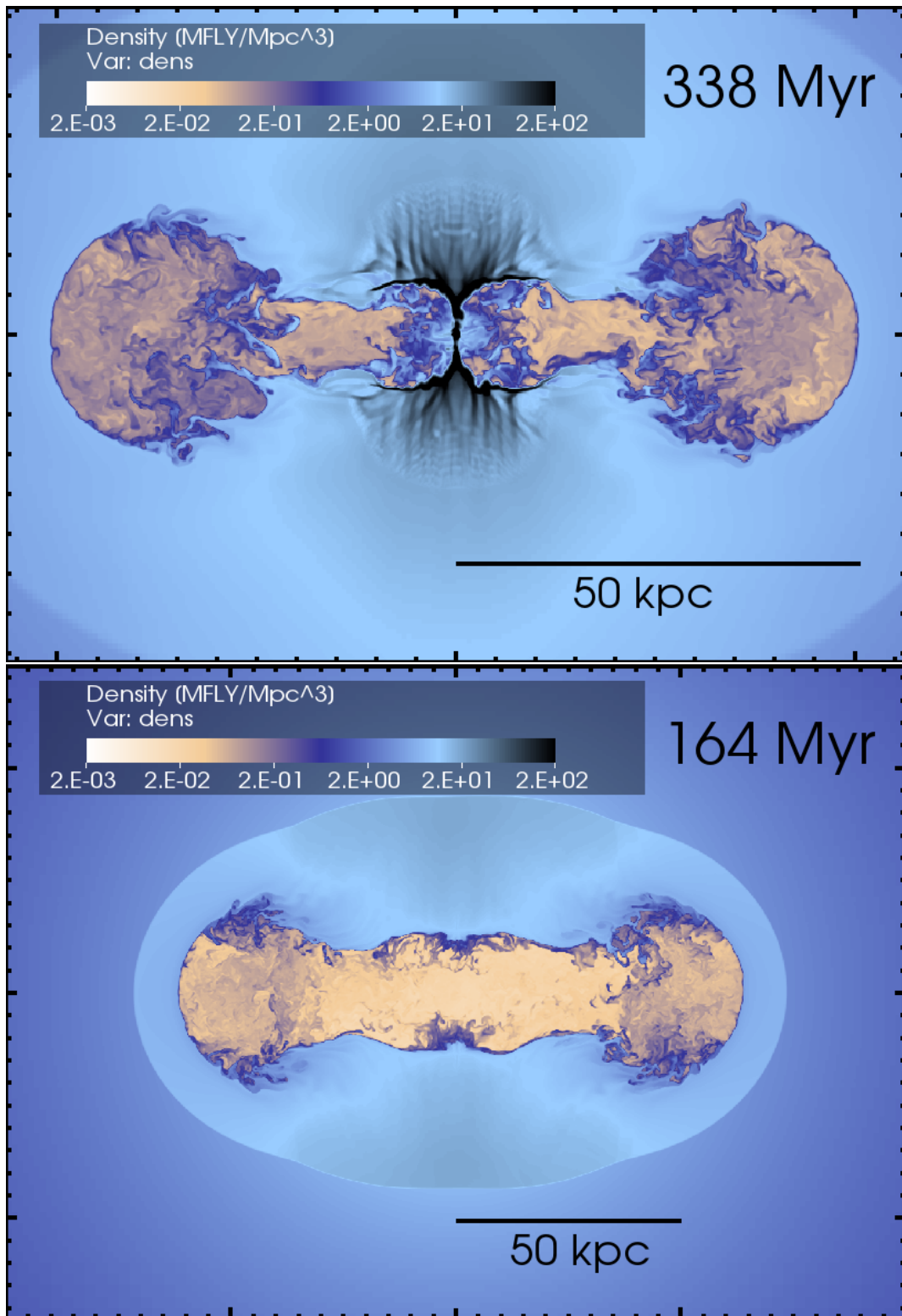


**Figure 4.4:** Advanced bubble phase in runs FC43 (top) and FC44 (bottom). Central density slices as in Figure 4.2. Both runs form extended, very spherical, bubbles. But in the more powerful FC44 run, the gas is quite hotter and less dense, preventing cooling much more effectively. Indeed, incipient runaway cooling is visible in the FC43 run (black region around the central hot chimneys).

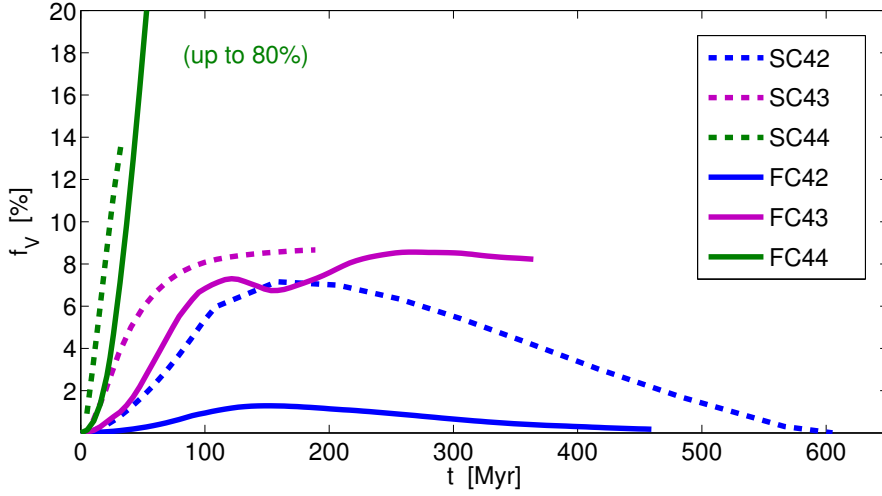


**Figure 4.5:** Volume fraction of the gas that has been heated by the jets, as a function of simulation time.

FR II runs instead have a large  $f_V$ , reaching 80% in less than 200 Myr, and may easily reach 100% (cold gas accretion totally quenched) for longer time scales. As for the bubbles, in FR II jets they tend to form at larger radii, because the cocoon quickly becomes much larger (in run FC44) or more elongated (in run SC44). These bubbles may eventually very well reach and pass  $r_{cool}$ , heating a large fraction of the gas in the process.

Eventually the bubbles will lose energy and fade because of radiative cooling and mixing with the hot environment gas. Following the approach of Agertz et al. (2007) (eqq. 7-9), we calculate the typical timescales  $\tau_{KH}$  and  $\tau_{RT}$  in which Kelvin-Helmholtz shearing instability and Rayleigh-Taylor buoyant instability may affect the bubbles (please note that we consider only the modes with wavelength equal to the bubble's radius, supposedly the most effective ones). For instance, at  $t_{age} = 150$  Myr, we find:

$$\tau_{KH} = 83.5 \text{ Myr}, \quad \tau_{RT} = 1748 \text{ Myr}$$

for run SC42 and

$$\tau_{KH} = 540 \text{ Myr}, \quad \tau_{RT} = 17300 \text{ Myr}$$

for run FC43.

As expected, Rayleigh-Taylor instability is much less effective. On the contrary, the prediction for KH destruction is very accurate in the SC42 case: we actually verify that the cloud is practically gone after  $\sim 5 \tau_{KH}$  (Figure 4.2). This confirms that our simulations can indeed model turbulence with adequate resolution, and that the bubbles feel shearing instabilities.

For FC43,  $\tau_{KH}$  is even longer, comparable to  $t_{cool}$  of the bubbles, so we can conclude that they will fade because of both cooling and mixing, being still unable to heat the gas for long times as discussed in Section 4.2.

## 4.4 Discussion

We performed and analyzed 3D detailed hydrodynamical simulation of jets from Active Galactic Nuclei (AGNs) propagating in a hot galactic halo environment, in order to study the efficiency of large-scale ( $\sim 100$  kpc) gas heating mechanisms. These mechanisms are at the heart of virtually all sub-grid implementations of AGN feedback in semi-analytical models and cosmological simulations.

The most representative of our runs, FC42 and FC43 (i.e.  $P_{\text{jet}} = 10^{42}$  and  $10^{43}$  erg/s, representative of the Fanaroff-Riley I class), show initial jet/halo energy coupling of order 5%, which drop quickly when the outflow ceases. These jets also show poor volume covering: they are able to heat only 2% to 8% of the volume within the halo cooling radius. Right after the jet shuts off, the halo reverts back to its initial state of very rapid cooling.

We have focused on heating by both sound wave (bow-shock) propagation (Section 4.2) and by the hot buoyant bubbles the jets create (Section 4.3); in the FRI case both mechanisms are found inefficient. The extra cooling triggered by the compression wave -if the jet is off- exceeds its energy deposition.

In runs with a jet power of  $10^{42-43}$  erg/s, even during the propagation of the jet there is strong cooling in the direction perpendicular to the jet axis, while the jets' path is still occupied by a hot gas which create a sort of *chimney*.

The hot gas bubbles expand in all the runs but FC42, in which they fall back to the center, dragged by the infall of cooling gas. In the other cases, they eventually fade out due to radiative cooling and/or are destroyed by hydrodynamical instabilities (Section 4.3).

Very powerful (but rare) Fanaroff-Riley II runs ( $M_{\text{jet}} = 20$ ,  $P_{\text{jet}} \geq 10^{44}$  erg/s) manage instead to heat up a larger fraction of the gas in the halo center. As expected, more powerful jets put more energy in the ISM even though they have shorter durations. This scenario is similar to the findings by Gaspari et al. (2012b), in which jets with power  $\gtrsim 10^{44}$  erg/s can delay cooling for more than 1 Gyr (making  $t_{\text{cool}}/t_{\text{ff}} \gtrsim 10$ ). While FRII sources are indeed jet-dominated objects, they are quite rare (e.g. van Velzen et al., 2014), and should not be regarded to as the typical example of AGN feedback.

Our findings show that while AGN jets (FRI) might have significant energy coupling to the gas, they seem to lack the required volume coverage to halt gas cooling onto the central galaxy on cosmological timescales ( $> 100$  Myr). This low covering fraction might challenge the generally accepted picture according to which AGN feedback is able to quench star formation in massive halos. Possible solutions might require an improved treatment of radiative cooling (Kannan et al., 2014), or the addition of a substantial jet precession with time (see Chapter 5).



---

## Work in Progress

---

This chapter covers just work in progress, projects expecting completion throughout the next months/one year; mostly because of their very high computational demands.

### 5.1 Jet tilting

In Chapter 4 we analysed the energy coupling and the volume coverage (with respect to the halo’s cooling radius) of the hot gas injected by AGN jets within a galactic halo (of total mass of order  $2 \times 10^{12} M_{\odot}$ ). We found that, while jets do convey much energy, they are not capable of heating a large enough volume of gas, so that runaway cooling is delayed by no more than the (relatively short) jets’ lifetime. An exception are the very hot and powerful Fanaroff-Riley type II jets, with power  $P_{\text{jet}} \geq 10^{44}$  erg/s.

In particular, Figure 4.2 (left column) shows how cooling is first triggered in gas laying around the jets’ chimney, i.e. in directions perpendicular to the jet.

One may then wonder what would happen if the jets were more effective in heating gas in the transverse direction. One way to achieve this could be injecting a hotter jet, which would result in more spherical cocoons. This is because, as we have verified in Chapter 3 hotter jets inject more thermal energy (thus enhancing isotropic thermal pressure). In our parametrization (eqq. 2.18), that would just mean to select a lower jet *internal Mach number*  $\mathcal{M}_{\text{jet}}$  (eq. 2.18b). Yet the Fanaroff-Riley type I jets we refer to (runs FC42 and FC43 from Table 4.1) are already quite “hot”, having  $\mathcal{M}_{\text{jet}} = 5$ , considered *transonic* in this context.

A more natural way would be to have the jets changing their pointing direction over time, in order to potentially affect a larger solid angle. Jets -not just from AGNs- are indeed expected to behave like this. The angular momentum vector of the central engine (a SMBH in the case of AGNs) is known to *precess* as a result of the accretion

inflow; the jets will eventually align with it. These dynamics are actually quite complex, requiring a general relativistic description, but have been captured in relativistic simulations as in the works listed in Section 3.1 (e.g. Fendt and Sheikhzami, 2013 or Sadowski et al., 2013).

Semi-analytical models are able to use similar prescriptions to follow the evolution of the specific angular momentum of the SMBHs from the actual accretion, but find more complex results than a simple precession around a fixed axis (Fanidakis et al., 2013; also: private communication by N. Fanidakis).

Kiloparsec-scale jets may themselves precess, describing a conic motion: this is the essence of the famous *dentist drill* model, known since long (Scheuer, 1982) and adopted also in simulations, yet usually on cluster scales (e.g. Vernaleo and Reynolds, 2006).

One, slightly simpler, alternative model applies instead to the case of multiple jet events, which are shot in different directions. This is the commonly accepted explanation for *Double-Double* or even *Triple-Double Radio Galaxies* (DDRGs and TDRGs; e.g. Saikia and Jamrozy, 2009) which show two or three pairs of Xray cavities (look also, for instance, at the center of the Perseus cluster shown in Figure 4.1) generated by jets.

We want to apply this model in our simulations, again to the case of Early Type Galaxies. Figure 5.1 shows one recent test of ours, in which we shoot a second bipolar jet at a 45 degree angle with respect the first.

A 3D rendering of the same run is shown in Figure 5.2, which is the basis for the cover picture of this thesis.

The halo is the same as the *Slow Cooling* run series introduced in Table 4.1 (it is a SC45). The jet in this test is actually very powerful:  $P_{\text{jet}} = 10^{45}$  erg/s, which according to our prescription (see Section 3.2) corresponds to a jet lifetime  $t_{\text{on}}$  of about 4.5 Myr. In this time, the jet manages to inflate a cocoon that extends up to almost 40 kpc away from the center. The jet is also quite cold (in other words, highly supersonic), having  $\mathcal{M}_{\text{jet}} = 20$ , so that the cocoons are quite extended along the  $z$  direction.

At this point, the jet direction is suddenly switched by 45 degrees. This is a rather large angle, chosen to give the jet high chances of heating gas in the transverse direction. The second jet has the same density and power as the first, though the injection area (and consequently the jet velocity) changed because the beams are now no more parallel to the grid axes (notes in Section 2.4).

The second bipolar jet has of course a completely different evolution. It initially propagates in the hot, sparse cocoon carved by the first jet, and travel at its unperturbed injection speed up to the cocoon border.

Here, the jet suddenly collides with the overdense bow-shock region, forming a pair of new hot spots due to the resulting strong shocks. Part of the hot jet material “bounces” against the border (bottom-left panel in Figure 5.1) and reaches the outskirts of the cavity, where a buoyant bubble would otherwise be detaching. The bounced beams are slowed down, so they are not able to form further shock features, but instead they keep inflating the cocoon pretty much as the first jet was doing.

The second jet is switched off after further 4.5 Myr, and the total run time is about 16 Myr; the bubbles still kept expanding, so the simulation's computational costs were still increasing.

From this run, we are able to draw the following (qualitative) conclusions.

1. As predictable, the second jet shows quite a different evolution, being confined in the cocoons. During their early stages, they are able to propagate much faster in the hot cocoon gas, but then they are confined by an overdense bow-shock region that they are unable to pierce, unlike the single jets we analysed in Chapter 3;

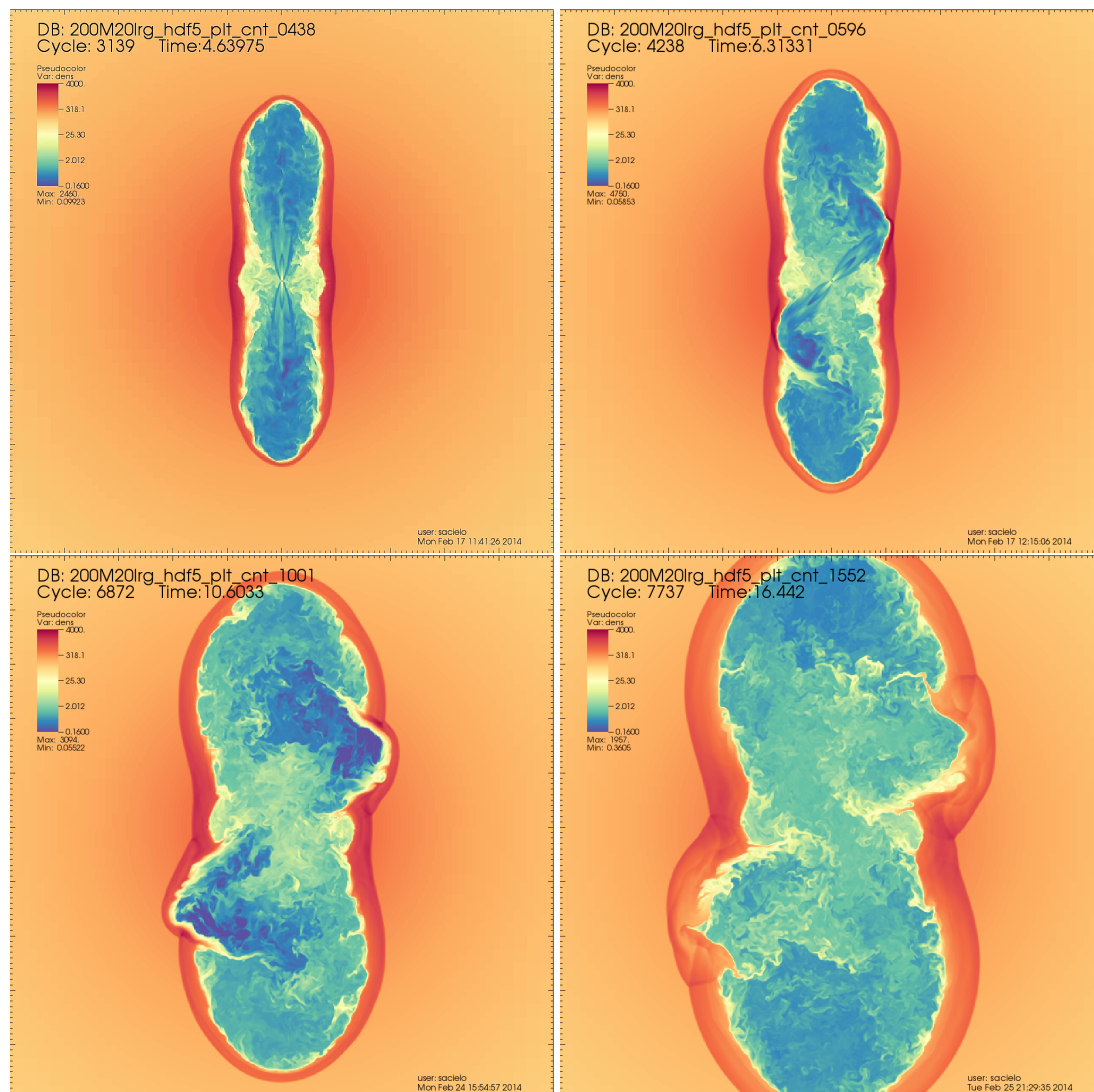


**Figure 5.1:** Evolution of a run with a second jet event, inclined by 45 degrees respect to the first. Here we show density slices along the plane containing both jets; each picture has a physical size of 100 by 100 kpc. The jets have a power of  $10^{45}$  erg/s. The snapshots show the following phases: (top-left) first bipolar jet is on for 4.5 Myr and carves a cocoon in the ISM; (top-right) the jet is tilted; (bottom-left) the second jet pushes the cocoon border, inflating the same cavity; (bottom-right) after the tilted jet is switched off, a very hot cavity filled with turbulent gas is left.

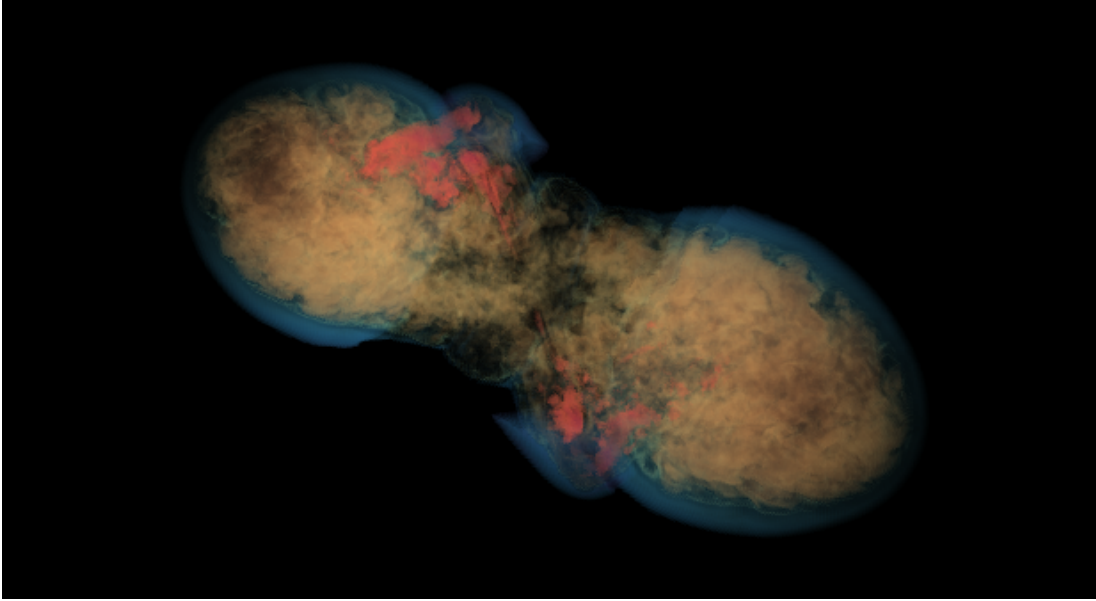


**Figure 5.2:** 3D rendering of the bottom-left panel of Figure 5.1. The color code is given according to temperature. This image is also the basis of this thesis' cover picture.

2. The second jet does not create a distinct bubble pair, but kept inflating the first cavities, delaying the formation and detaching of bubbles. Likely, the jet axis was tilted too quickly, not allowing the gas to relax as in the runs presented in Chapter 4.
3. The jet reaches very quickly the *lobe inflation phase* described in Section 3.3, but this time the gas that inflates the lobes undergoes strong shocks against the cocoon walls, so much brighter hot spots are present. In no run with a single jet event such hot spots co-existed with lobes; this is a clear signature of this stage.
4. The strong shocks are very effective in heating the inner cocoon gas, and the new jets trigger much more Kelvin-Helmholtz instability that persists even after the jets are switched off (bottom-right panel of Figure 5.1). So the cocoon is in general hotter and in a highly turbulent state.
5. The second jets may leave some shape imprint in the bow-shock boundary, in correspondance of the second hot spots, but quite mild.
6. Most importantly, the new jets keep following the tracks carved by the first, so they do not seem to affect larger solid angles at the halo center.

This run is, unfortunately, not quite ideal: the slow cooling halo and high jet power make jet tilting unnecessary for heating purposes. Indeed, an analysis as the one we performed in Chapter 4 would be meaningless: the volume coverage in this case would just trivially saturate at 100%. As an additional complication, in consequence of the high  $P_{\text{jet}}$ , the cavities expanded so fast that the simulation had to be stopped at early times.

At the time of writing, new simulations are running, introducing tilting jets in runs analogue to the FC42 and FC43 in Table 4.1, for which a quantitative analysis such as in Chapter 4 will be significant and readily made.

### 5.1.1 Kinematics of powerful jets: recollimation shocks

The jets in the run presented above show initially a non-zero aperture angle, due to both the temperature discontinuity and the little sampling of the jet radius in the grid, being injected by just four cells. This behaviour is expected, but not desirable, since AGNs jets are very collimated flows. In the simulations as in reality, the jets are actually kept coherent for a few tens of kiloparsecs by a few successive *recollimation shocks*, a series of conical shocks ultimately generated by pressure imbalance between the jets and the hot gas phase. In Figure 5.1 we show simulated recollimation shocks for a run identical to the SC45 presented above, but with no jet tilting. These shocks are visible in the gas pressure as a regular series of “knots” along the jet beam, with a characteristic alternation of high and low pressure regions. These are separated by a constant spacing given approximately by  $\mathcal{M}_{\text{jet}} r_{\text{jet}}$ , where  $r_{\text{jet}}$  is the radius of the jet beam. This spacing matches theoretical predictions and the results of other similar simulations (e.g. Perucho et al., 2014a).

In the run with jet tilting, recollimation shocks are present in both the first and second jet pair. Their “knotty” features are sometimes observed in kiloparsec beams of real radio galaxy, and must not be mistaken for signatures of episodic jet activity (which may be in operation nevertheless, as in this case).

## 5.2 Cold clouds

If the problem we want to address concerns the galactic star formation (Section 1.3.1), we cannot do it directly with just the hot gas component. The Inter-Stellar Medium (ISM) and the Circum-Galactic Medium (CGM) in and around galactic environments must contain also a cold gas component.

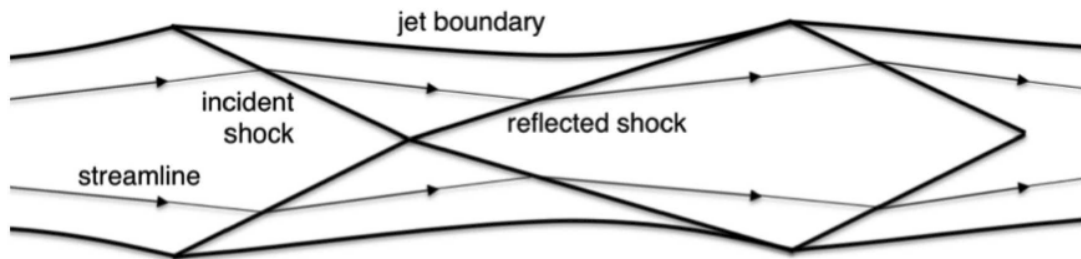
Ideally, one may want to add to the simulation a *warm* neutral gas component (around  $10^4$  K), as well as an atomic (much colder, around 100 K) and molecular (10 K) *cold* ones. These gas components are typically assumed to be distributed in clumps of a few hundred parsec to one kiloparsec in size, although recent observations of high redshift Lyman  $\alpha$  emission around bright high-redshift quasars (e.g. Cantalupo et al., 2014) imply a diffuse warm component. This emission suggests the presence of a population of smaller (tens of parsecs) gas clumps with sub-solar metallicity (Arrighi Battaia et al., 2014).

In Section 2.4 we had introduced our intention of adding a colder gas phase ( $10^4$  K) in the form of spherical clouds, initially in pressure equilibrium with the hot phase, and 50 – 200 pc in size. These clouds would be Jeans-unstable on their largest scales, allowing explicit star formation tracing (of course, on scales of 10 – 20 pc) by use of *sink particles*, as shown in Figure 5.4 (left panel).

This setup allows us to study the direct effect of AGN feedback on star formation with a minimum set of external assumptions; for instance we would not have to impose manually -as it is custom where there is cold gas but no stars- that star formation follows a Schmidt-Kennicutt (Schmidt, 1959) relation; this result would have to follow directly from the model implementation. Of course, it would have to be verified in the first place.

The inclusion of the cold clouds could also change the value of the energy coupling constants calculated in Section 4.2.

These parts of the simulation setup have already been tested, and in this section



DB: s200m10P45b640110\_hdf5\_plt\_cnt\_0087  
Cycle: 4964 Time:8.57543

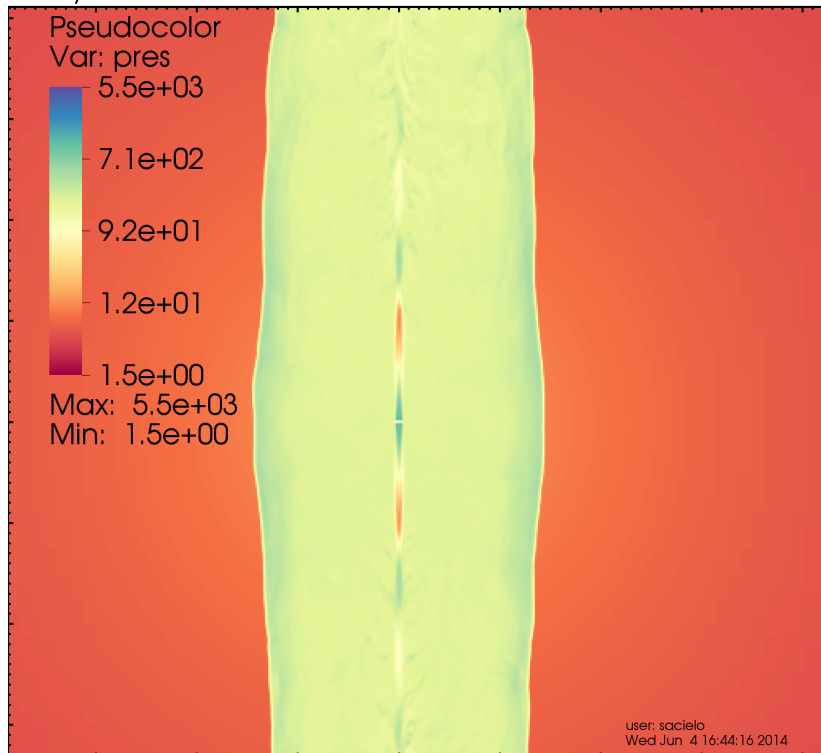


**Figure 5.3:** Top: sketch of how recollimation shocks can focus a highly supersonic jet beam; in the case of AGNs this mechanism is able to collimate them for several tens of kiloparsecs. Picture from Perucho et al. (2014a). Bottom: recollimation shocks visible as “knots” in the jet beam of our simulated jets (pressure slices). The image size is 65 by 65 kpc. The spacing of these shock features is roughly equal to the jet’s internal Mach number times the beam radius, matching theoretical predictions.

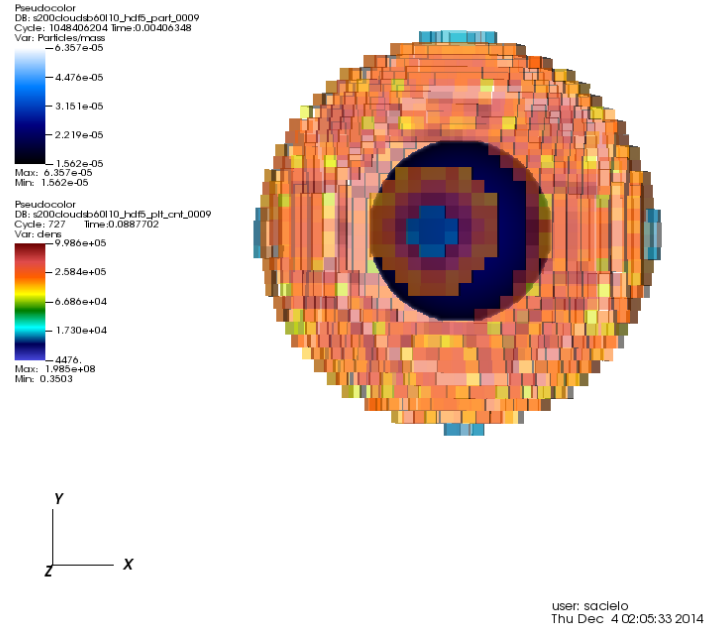


**Figure 5.4:** 3D false color plot of a single cloud, resolved by about 400 cells. The shading reveals a single sink particles at its center, generated by FLASH in run time. The particle has taken some of the clouds' gas, converting it into its internal mass, which we can interpretate as newly formed stellar mass.

we show some prototype runs.

In Figure 5.5 we show a simple 3D rendering of a run featuring a few clouds about the halo center, giving a good idea of their relative size and resolution requirements. We were forced to adopt a much smaller simulation box than the one used in Chapter 4 (the box side is 64 instead of 640 kpc).

Unfortunately, so far we were not yet able to produce runs with a cold component, the main limitation being the high computational requirements.

Absolute resolution is not a problem, as we could with relative ease push it down to 10 or 20 parsec, to resolve quite well at least the largest clouds. Yet, a gas phase with such a different temperature would be immediately maximally refined by FLASH (see Section 2.2), together with all the volume it is distributed in<sup>1</sup> (see also Figure 5.6).

This would completely negate the advantages of the AMR scheme, unless we were able to push the maximum resolution up to a point in which clouds would not require the maximum refinement level. Such a simulation will still be an optimal use of AMR, but will of course be even more demanding than the ones shown here.

Other solutions may contemplate changing the grid type to uniform or to patch-based AMR (Section 2.2). Uniform grids are supported by FLASH, yet adopting it would be a rather major change in the setup. This path is still impractical due to memory and disk space: computational efforts will be reduced by eliminating the

<sup>1</sup>This is not just a computational problem: we NEED those clouds to be maximally resolved.

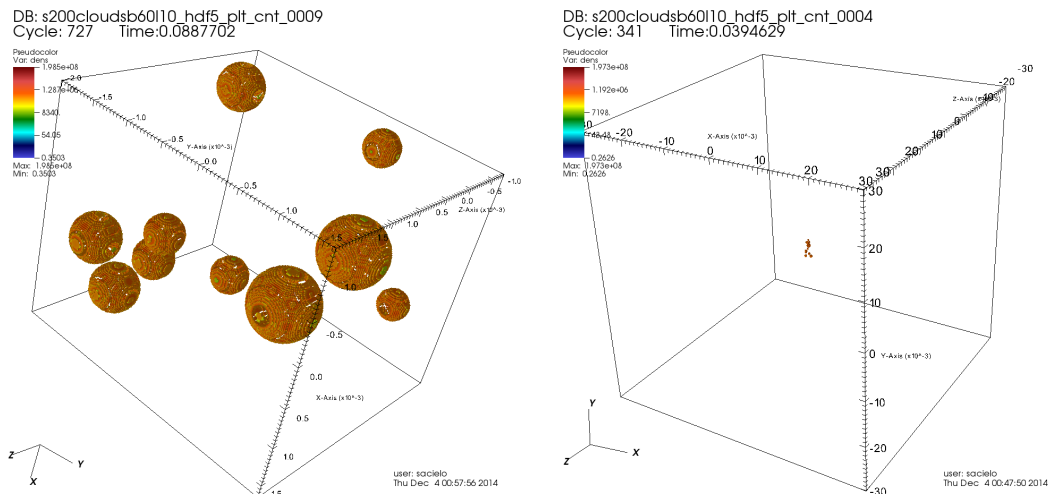


**Figure 5.5:** Simple 3D false color plot of a few clouds in a test run without jets (color code according to the clouds' density). Left: the clouds fill the central kpc of the halo. The resolution elements (cubic cells) are barely visible; such a cloud manages (and needs) to be resolved by at the very least about 200 cells (in 3D). Right: the same clouds in their full simulation box, a cube of 64 kpc side, to show the relative cloud size. The volume of this box is already a factor  $10^3$  smaller than in our runs shown in Chapter 4.

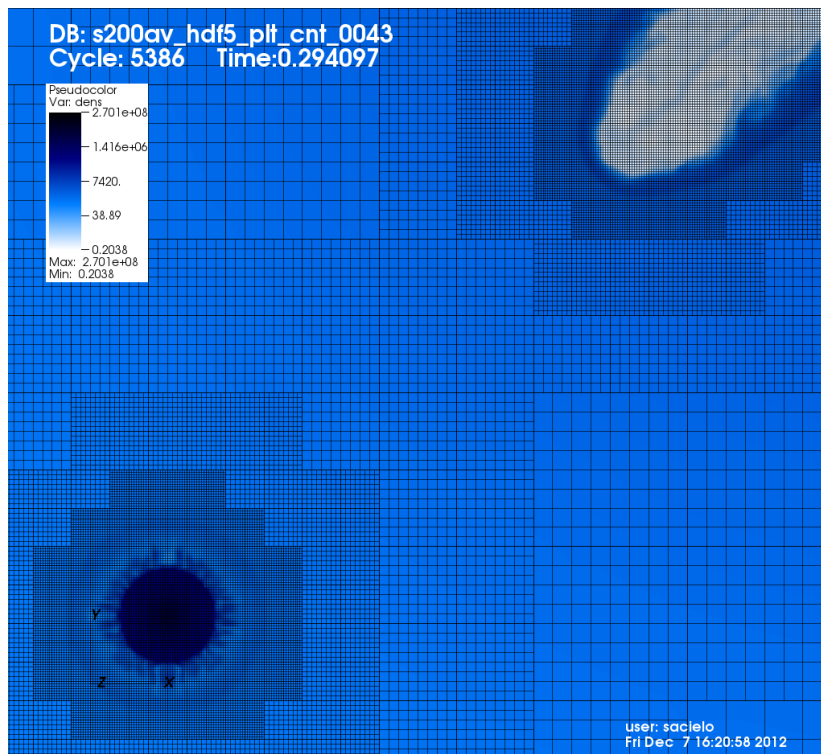


**Figure 5.6:** 2D density slice of a run with a single cloud, analogue to the 200p5 run from Table 3.1, including a plot of the refined mesh. Image size: roughly 5 kpc. One cloud can trigger refinement in a much larger volume.

AMR structure, but the computational domain will still be huge. Patch-based AMR could offer a much more practical solution, provided that the refinement patches do not exceed by much the size of the single clouds, which condition seems quite easily

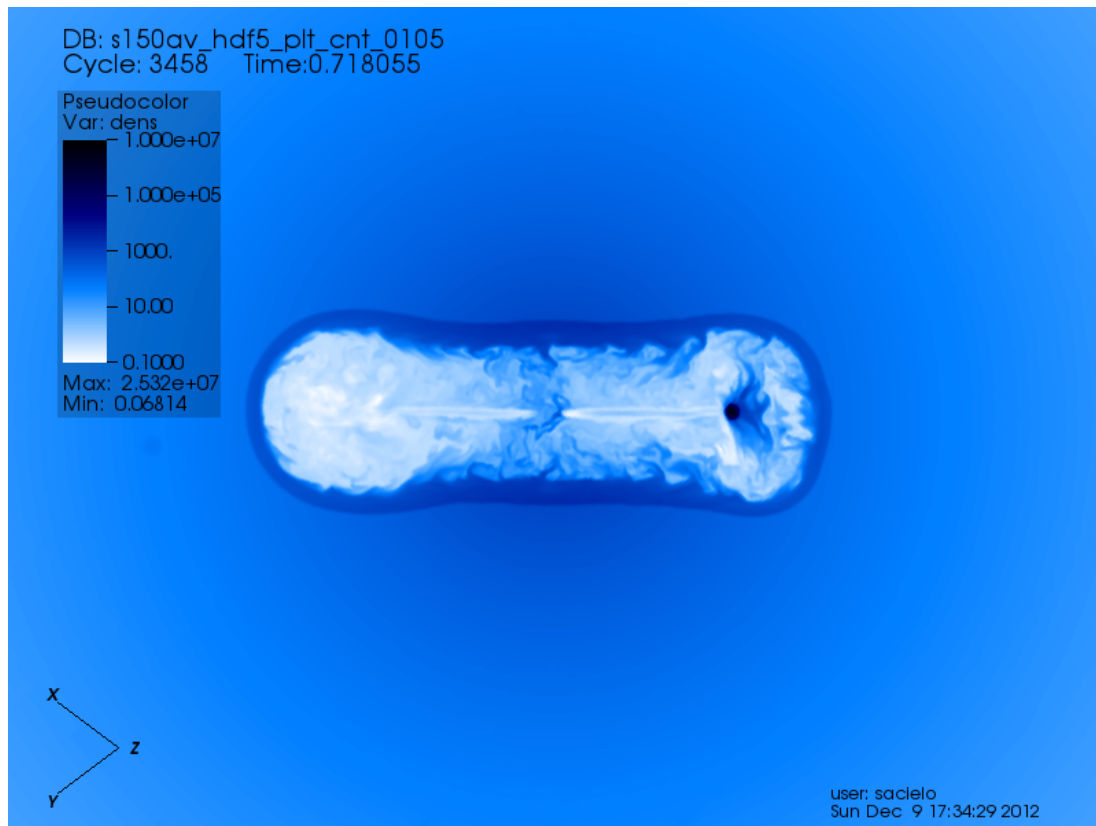


**Figure 5.7:** 2D density slice as in Figure 5.6, for a run analogue to the 150p5 run from Table 3.1. Only the clouds' outer layers were heated and sheared by the cocoon.

achieved. The next FLASH updates will be crucial on this respect.

Meanwhile, to conduct our tests we had to keep the number of clouds very low, and tried to segregate them in the halo center or in a single plane with little scatter. A unique case of a jet cocoon encountering one cloud is shown in Figure 5.7. Only the cloud external layers were affected by the jets.

Furhter developments of this setup would require also the inclusion of thermal conductivity, but it is wiser to wait for the full inclusion of the CHOMBO patch-based AMR in FLASH.

### 5.3 Synthetic X-ray images

We mentioned several times how the hot bubbles are observed as X-ray cavities (sometimes filled by radio emission from the jets), and how these observations have been useful in deducing the jets' global parameters.

The opposite approach, i.e. *forward modeling* can, in turn, favour very much the interpretation of observed images. Managing to create mock observational data from our simulations can indeed be very instructive. The easiest interesting part of the

electromagnetic spectrum to model is just the X-ray.

On the very first approximation, the X-ray luminosity comes mostly from *thermal brehmsstrahlung emission* from the hot electron population. The *integrated brehmsstrahlung luminosity* gives in turn precise information about the (electron) gas density and temperature, as for instance shown in Rybicki and Lightman (2007), equation (5.15b). We adopt the same equation in computing radiative cooling rates at the highest temperatures (above  $10^{8.5}$  K), in order to extend the upper temperature end of our cooling table (see Section 2.3).

In Figure 5.8 (top panel) we plot the simple expression  $\rho^2 T^{0.5}$  from run FC42 (where  $\rho$  is the gas density and  $T$  its temperature). Assuming that the gas and the electrons have the same temperature, and that the electron density is everywhere proportional to the gas density, these are just the essential factors appearing in the thermal brehmsstrahlung integrated emission. The picture presents most of the cocoon relevant features, and the bubbles are indeed darker.

Such an image does not really “go very forward” in the observational modeling. The X-ray luminosity obtained from actual observations presents in fact the characteristics mentioned in the following list:

1. the observations are restricted to some finite band (typically around 1 and a few keV). For brehmsstrahlung, this means looking through a precise electron temperature window (Boltzmann factor in Rybicki and Lightman, 2007, equation 5.14b).
2. the emitting electron population number density and temperature are not exactly the same as in the global gas.
3. the emission contains not only thermal brehmsstrahlung, but also atomic emission lines (mostly from highly ionized metals).
4. The actual measurements depend on the parameters of the telescope (response functions, telescope area), of the object (distance, redshift, galactic extinction) and on the exposure time.

This is why we wanted to move to some more sophisticated method, that could make use of the resources provided by the observational community. In particular, we used the the *Photon Simulator* module of the yt analysis software in order to simulate observation by the Chandra X-ray telescope. The result is shown in the bottom panel of Figure 5.8, for the same spatial region as before, for direct comparison. The picture is obtained just by following the Photon Simulator tutorial.

As explained in the tutorial, the Photon Simulator analysis module enables the creation of simulated X-ray photon lists of events from datasets that yt is able to read<sup>2</sup>. The simulated events then can be exported to X-ray telescope simulators to produce realistic observations or can be analyzed in-line. The algorithm is based off of that

<sup>2</sup>FLASH datasets are natively supported by yt, but reading datasets in FLY units required the active help of the yt developers community.

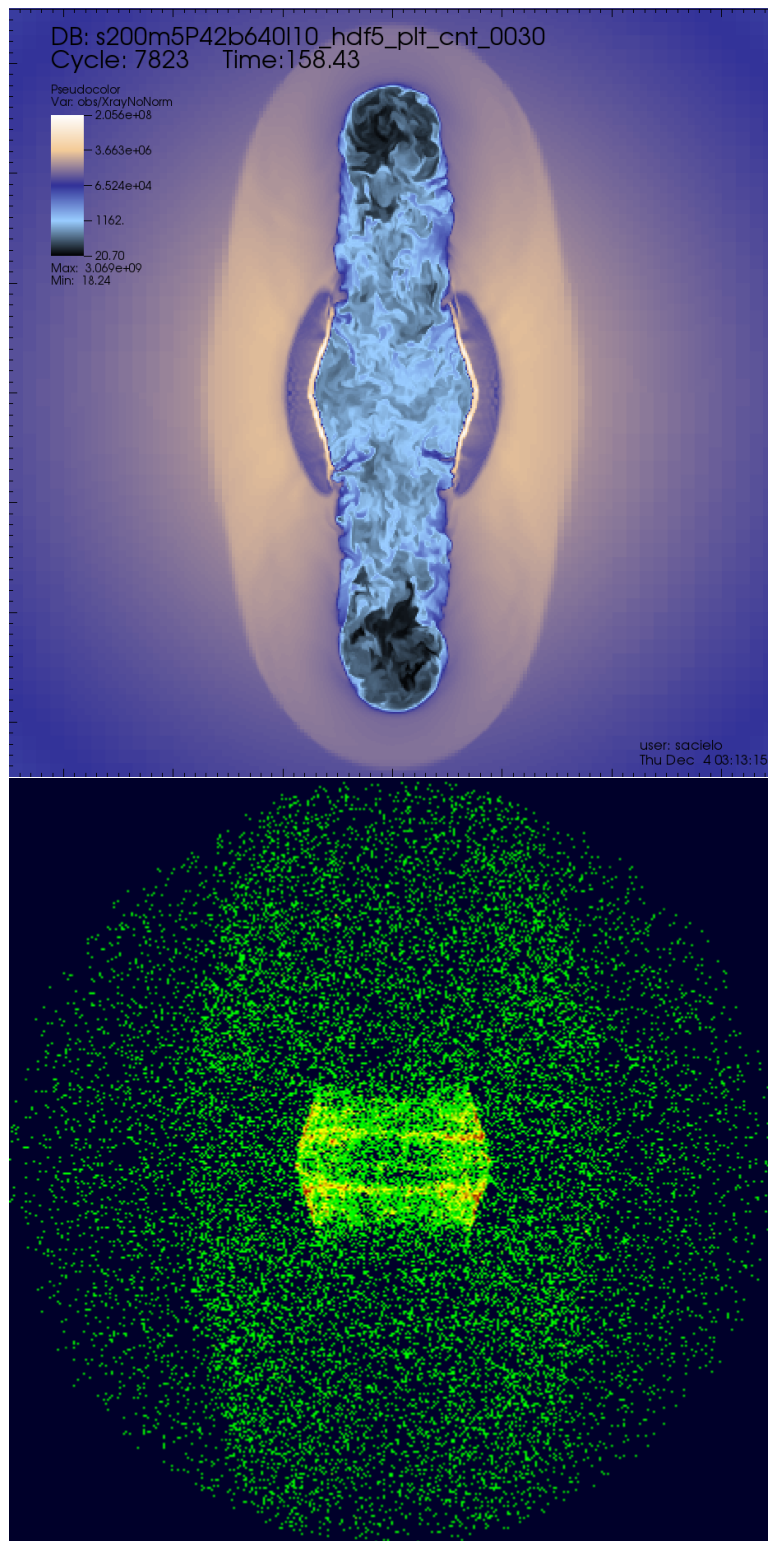


**Figure 5.8:** Synthetic X-ray images created from run FC42. Both images have a physical size of 70 kpc, for comparison. Top: 2D slice of (a simple proxy for) integrated thermal brehmsstrahlung luminosity (arbitrary units). Bottom: mock X-ray image simulating an observation from the Chandra X-ray telescope, obtained by the *Photon Simulator* package of the yt analysis software (<http://yt-project.org/>).

implemented in PHOX for SPH datasets by Veronica Biffi and Klaus Dolag (Biffi et al., 2012, 2013).

The basic procedure is as follows:

1. Using a spectral model for the photon flux given the gas properties, and an algorithm for generating photons from the dataset loaded in yt, produce a large number of photons in three-dimensional space associated with the cells of the dataset.
2. Use this three-dimensional dataset as a sample from which to generate photon events that are projected along a line of sight, Doppler and cosmologically shifted, and absorbed by the Galactic foreground.
3. Optionally convolve these photons with instrument responses and produce images and spectra.

In this case, the photons were generated using the AtomDB library version 2.0.2. The photons were created with energies between 0.1 and 2.0 keV (about  $10^5$  to  $2.5 \times 10^6$  K), binned in 100 channels. The density and temperature of the gas generating photons were read from the simulation outputs; the gas' hydrogen mass fraction was set to 0.75 and its metallicity of 0.3 times the solar value.

The simulated telescope would have a collecting area of  $6000 \text{ cm}^2$ ; the exposure time was set to  $4 \times 10^5$  seconds. The source was set to have a redshift 0.01 and we asked Photon Simulator to correct for galactic absorption. The generated photon 3D density was projected along the same line of sight as the upper panel of the figure; finally the results were convolved with the Chandra Telescope's response functions. This process yielded about 45000 individual photons. The telescope parameters set above may actually represent a downgrade of Chandra's capabilities, and were chosen in order to have an easier test.

In the resulting image one can still see the bow-shock region around the darker bubbles, but this time the most prominent feature is actually the fast-cooling gas in the central ring (Figure 4.2).

---

## Summary and Conclusions

---

Active Galactic Nuclei (AGNs) are the most powerful engines in the Universe, capable of powering quasars as luminous as  $10^{46}$  erg/s and generated the kiloparsec-scale jets we see in radio galaxies (Chapter 1).

AGNs are found in galactic halos that span a broad range of mass: from halos hosting Milky Way sized objects to the most massive galaxy clusters and superclusters. Feedback from AGNs is believed to play an important role in galaxy formation and in the energetic balance within galactic halos. Current models of galaxy formation require heat from AGN feedback to prevent large quantities of gas from overcooling, thus resulting in too high stellar masses (Section 1.3.1).

In this thesis we test heating by AGNs with small scale simulations of bipolar jets in individual halos. We run a pool of high resolution, threedimensional simulations with the Adaptive Mesh Refinement hydrodynamics code FLASH (Chapter 2).

In Chapter 3 we present some very detailed simulations of the early stages of AGN jets, varying a broad range of parameters: jet density, thermal pressure, and internal Mach number, mass of the host halo. We analyse the evolutionary stages of the systems (Section 3.3), the shape of the cavities (the “cocoon”) the jets inflate (Section 3.4), their thermodynamic state and energy coupling with the hot halo gas (Section 3.5); these results are finally discussed in Section 3.7.

We are able follow the evolution of jets up to the development of extended hot lobes; the details vary with the halo and jet paramers, but we could distinguish three main evolutionary phases:

**Creation of a cocoon** The jet shocks the halo gas and starts inflating a cavity delimited by a dense, expanding, *bow-shock* region; the most powerful jets show two *hot spots* where the jet beam shock-hits the cocoon.

**Forward propagation** This phase is characterized by complex hydrodynamics that eventually shape the cocoon.

**Lobe inflation** After the supersonic jet reaches the outskirts of the halo, it often pierces the cocoon and opens in large lobes, analogue to observed kiloparsec-scale radio lobes.

We measure the shapes of the cocoons our jets produce; we found with little surprise that more powerful jets have a faster evolution, and that hotter jets tend to create more spherical cocoons. **We approximated the cocoons as ellipsoids, and compared their axis ratio to theoretical models, not confirming -in general- the prediction of a self-similar evolution** (i.e. axis ratio constant over time), mainly because of the complex hydrodynamical processes in play during the forward propagation phase. The jets who most likely reach a self-similar state -before the lobe phase- are the least dense ones.

As for the thermodynamics of the system, we found that **the inner gas in the cocoon/lobes reaches quickly a constant temperature ( $10^{10}$  K) and keeps it during the expansion**; the ratio of turbulent over thermal pressure converges to 10 – 20%, so that turbulence is dynamically important. As for the energy balance of the system, the mechanical work done by inflating the cavities and the exchanged heat yield an **energy coupling (energy deposited over input energy) of a few percent**, very significant in term of galaxy evolution.

Previous 2D simulations had observed gas flowing from the outskirts of the cocoons back to the central region. These *backflows* are likely contributors to the gas accretion onto the central Black Hole, though it is impossible to resolve direct accretion scales in this kind of simulations. **We measure significant backflow for the first  $\sim 10^5$  years**, but find that after this period the flows within an expanding cocoon cannot reach the halo center anymore, unlike in the 2D models. We proved that the flows are not destroyed by shearing (Kelvin-Helmholtz) instability (Section 3.6.2), so the reason has to lie in the dynamics of cocoon expansion with an increased degree of freedom (see Figure 3.10). Nevertheless, by the time the backflows cease, a hot ( $10^8$  K) gas reservoir as massive as  $2 \sim 10^5 M_{\odot}$  is formed in the halo center.

In Chapter 4, we expand our analysis to cosmologically relevant timescales, focusing mostly on the effect of feedback of Fanaroff-Riley type I (FRI) sources in halos hosting individual Early Type Galaxies (Section 4.1). These FRI jets are on average less powerful than the ones studied in Chapter 3, but they are far more representative examples of AGN feedback.

We assume the jets to be active for a time  $t_{\text{on}}$  (a few to about a hundred Myr, depending on the jet power); we then switch them off, and observe how the lobes evolve to form hot **buoyant bubbles**. These bubbles are seen to be Kelvin-Helmholtz unstable, and subject to radiative cooling, so they fade and mix with the ambient gas after a few hundred Myr (Section 4.3).

Again, the energy coupling is of order 3 – 5% for all runs, but **the FRI jets do not significantly counteract cooling** (Section 4.2) after the central energy source is turned off.

---

More powerful jets (Fanaroff-Riley type II; in our simulations, these are the jets with a mechanical power  $\geq 10^{44}$  erg/s) can set the gas on a much hotter track, potentially delaying cooling for cosmological timescales.

We also investigate where in the halo the energy is deposited: again, **FRI jets are not very effective, heating only up to 8% of the gas volume** within the halo's *cooling radius* (Section 4.3). We distinguish the energy contribution of the lobes/bubbles from the one of bow-shock region: although the latter may reach out to larger distances, its contribution to the gas heating is negligible.

In Chapter 5, we present a few extensions of our model. We had found that cooling is triggered in gas laying in the plane perpendicular to the jet axis; this may imply that recurring jet events, each shot in different directions, may be more effective in delay the cooling. We try thus to implement this feature in our run, and show some qualitative result. We also test the inclusion of a cold gas component, in form of spherical clouds. Finally, we successfully lay the basis for production of **synthetic X-ray images** directly from the simulation outputs (Section 5.3), that can significantly help the interpretation of observed sources.

Over all, our findings show that while AGN jets might have significant energy coupling with Inter-Stellar/Circum-Galactic Medium, they (except in the most powerful, but rare, cases) seem to lack the required volume coverage to halt gas cooling onto the central galaxy on cosmological timescales ( $> 100$  Myr).

This low covering fraction might **challenge the generally accepted picture according to which AGN feedback is able to quench star formation in massive halos.**



---

## References

---

- Abdo, A. A., Ackermann, M., Ajello, M., Asano, K., Atwood, W. B., Axelsson, M., Baldini, L., Ballet, J., Barbiellini, G., Baring, M. G., and et al. (2009). A limit on the variation of the speed of light arising from quantum gravity effects. *Nature*, 462:331–334.
- Agertz, O., Moore, B., Stadel, J., Potter, D., Miniati, F., Read, J., Mayer, L., Gawryszczak, A., Kravtsov, A., Nordlund, Å., Pearce, F., Quilis, V., Rudd, D., Springel, V., Stone, J., Tasker, E., Teyssier, R., Wadsley, J., and Walder, R. (2007). Fundamental differences between sph and grid methods. *MNRAS*, 380:963–978.
- Alexander, P. (2002). On the interaction of FR II radio sources with the intracluster medium. *MNRAS*, 335:610–620.
- Alexander, P. (2006). Models of young powerful radio sources. *MNRAS*, 368:1404–1410.
- Antonuccio-Delogu, V., Becciani, U., and Ferro, D. (2003). FLY. A parallel tree N-body code for cosmological simulations. *Computer Physics Communications*, 155:159–179.
- Antonuccio-Delogu, V. and Silk, J. (2008a). Active galactic nuclei jet-induced feedback in galaxies - I. Suppression of star formation. *MNRAS*, 389:1750–1762.
- Antonuccio-Delogu, V. and Silk, J. (2008b). Agn feedback from jet-ism/igm interactions. In Bureau, M., Athanassoula, E., and Barbuy, B., editors, *IAU Symposium*, volume 245 of *IAU Symposium*, pages 31–32.
- Antonuccio-Delogu, V. and Silk, J. (2010a). Active galactic nuclei activity: self-regulation from backflow. *MNRAS*, 405:1303–1314.
- Antonuccio-Delogu, V. and Silk, J. (2010b). Feeding the agn with backflows. In Maraschi, L., Ghisellini, G., Della Ceca, R., and Tavecchio, F., editors, *Accretion and Ejection in AGN: a Global View*, volume 427 of *Astronomical Society of the Pacific Conference Series*, page 343.

- Arrigoni Battaia, F., Yang, Y., Hennawi, J. F., Prochaska, J. X., Matsuda, Y., Yamada, T., and Hayashino, T. (2014). A Deep Narrowband Imaging Search for CIV and He II Emission from Ly alpha Blobs. *ArXiv e-prints*.
- Babul, A., Balogh, M. L., Lewis, G. F., and Poole, G. B. (2002). Physical implications of the x-ray properties of galaxy groups and clusters. *MNRAS*, 330:329–343.
- Balbus, S. A. and Hawley, J. F. (1991). A powerful local shear instability in weakly magnetized disks. 1. Linear analysis. 2. Nonlinear evolution. *Astrophys.J.*, 376:214–233.
- Beckmann, V. and Shrader, C. (2012). *AGN Types and Unification*, pages 89–140. Wiley-VCH Verlag GmbH and Co. KGaA.
- Beckwith, K., Hawley, J. F., and Krolik, J. H. (2008). The Influence of Magnetic Field Geometry on the Evolution of Black Hole Accretion Flows: Similar Disks, Drastically Different Jets. *ApJ*, 678:1180–1199.
- Begelman, M. C. (2012). Radiatively inefficient accretion: breezes, winds and hyper-accretion. *MNRAS*, 420:2912–2923.
- Best, P. N., Kauffmann, G., Heckman, T. M., Brinchmann, J., Charlot, S., Ivezić, Ž., and White, S. D. M. (2005). The host galaxies of radio-loud active galactic nuclei: mass dependences, gas cooling and active galactic nuclei feedback. *MNRAS*, 362:25–40.
- Bicknell, G. V. (1995). Relativistic jets and the fanaroff-riley classification of radio galaxies. *ApJS*, 101:29.
- Biffi, V., Dolag, K., and Böhringer, H. (2013). Investigating the velocity structure and X-ray observable properties of simulated galaxy clusters with PHOX. *MNRAS*, 428:1395–1409.
- Biffi, V., Dolag, K., Böhringer, H., and Lemson, G. (2012). Observing simulated galaxy clusters with PHOX: a novel X-ray photon simulator. *MNRAS*, 420:3545–3556.
- Blandford, R. and Znajek, R. (1977). Electromagnetic extractions of energy from kerr black holes. *MNRAS*, 179:433–456.
- Blandford, R. D. and Begelman, M. C. (1999). On the fate of gas accreting at a low rate on to a black hole. *MNRAS*, 303:L1–L5.
- Blandford, R. D. and Payne, D. G. (1982). Hydromagnetic flows from accretion discs and the production of radio jets. *MNRAS*, 199:883–903.
- Broderick, A. E., Chang, P., and Pfrommer, C. (2012). The Cosmological Impact of Luminous TeV Blazars. I. Implications of Plasma Instabilities for the Intergalactic Magnetic Field and Extragalactic Gamma-Ray Background. *ApJ*, 752:22.
- Bulbul, E., Markevitch, M., Foster, A., Smith, R. K., Loewenstein, M., and Randall, S. W. (2014). Detection of an Unidentified Emission Line in the Stacked X-Ray Spectrum of Galaxy Clusters. *ApJ*, 789:13.

- 
- Cantalupo, S., Arrigoni-Battaia, F., Prochaska, J. X., Hennawi, J. F., and Madau, P. (2014). A cosmic web filament revealed in Lyman- $\alpha$  emission around a luminous high-redshift quasar. *Nature*, 506:63–66.
- Capelo, P. R., Natarajan, P., and Coppi, P. S. (2010). Hydrostatic equilibrium profiles for gas in elliptical galaxies. *MNRAS*, 407:1148–1156.
- Chattopadhyay, I. and Ryu, D. (2009). Effects of Fluid Composition on Spherical Flows Around Black Holes. *ApJ*, 694:492–501.
- Cielo, S., Antonuccio-Delogu, V., Macciò, A. V., Romeo, A. D., and Silk, J. (2014). 3d simulations of the early stages of agn jets: geometry, thermodynamics and backflow. *MNRAS*, 439:2903–2916.
- Croston, J. H., Sanders, J. S., Heinz, S., Hardcastle, M. J., Zhuravleva, I., Birzan, L., Bower, R. G., Brüggén, M., Churazov, E., Edge, A. C., Etori, S., Fabian, A. C., Finoguenov, A., Kaastra, J., Gaspari, M., Gitti, M., Nulsen, P. E. J., McNamara, B. R., Pointecouteau, E., Ponman, T. J., Pratt, G. W., Rafferty, D. A., Reiprich, T. H., Sijacki, D., Worrall, D. M., Kraft, R. P., McCarthy, I., and Wise, M. (2013). The hot and energetic universe: Agn feedback in galaxy clusters and groups. *ArXiv e-prints*: 1306.2323.
- Croton, D. J., Springel, V., White, S. D. M., De Lucia, G., Frenk, C. S., Gao, L., Jenkins, A., Kauffmann, G., Navarro, J. F., and Yoshida, N. (2006). The many lives of active galactic nuclei: cooling flows, black holes and the luminosities and colours of galaxies. *MNRAS*, 365:11–28.
- della Ceca, R., Lamorani, G., Maccacaro, T., Wolter, A., Griffiths, R., Stocke, J. T., and Setti, G. (1994). The properties of X-ray selected active galactic nuclei. 3: The radio-quiet versus radio-loud samples. *ApJ*, 430:533–544.
- Di Matteo, T., Quataert, E., Allen, S. W., Narayan, R., and Fabian, A. C. (2000). Low-radiative-efficiency accretion in the nuclei of elliptical galaxies. *MNRAS*, 311:507–521.
- Díaz Trigo, M., Miller-Jones, J. C. A., Migliari, S., Broderick, J. W., and Tzioumis, T. (2013). Baryons in the relativistic jets of the stellar-mass black-hole candidate 4U1630-47. *Nature*, 504:260–262.
- Diehl, S. and Statler, T. S. (2008). The Hot Interstellar Medium in Normal Elliptical Galaxies. III. The Thermal Structure of the Gas. *ApJ*, 687:986–996.
- Dubois, Y., Pichon, C., Welker, C., Le Borgne, D., Devriendt, J., Laigle, C., Codis, S., Pogosyan, D., Arnouts, S., Benabed, K., Bertin, E., Blaizot, J., Bouchet, F., Cardoso, J.-F., Colombi, S., de Lapparent, V., Desjacques, V., Gavazzi, R., Kassin, S., Kimm, T., McCracken, H., Milliard, B., Peirani, S., Prunet, S., Rouberol, S., Silk, J., Slyz, A., Sousbie, T., Teyssier, R., Tresse, L., Treyer, M., Vibert, D., and Volonteri, M. (2014a). Dancing in the dark: galactic properties trace spin swings along the cosmic web. *ArXiv e-prints*.

- Dubois, Y., Volonteri, M., and Silk, J. (2014b). Black hole evolution - III. Statistical properties of mass growth and spin evolution using large-scale hydrodynamical cosmological simulations. *MNRAS*, 440:1590–1606.
- Dutton, A. A. and Macciò, A. V. (2014). Cold dark matter haloes in the Planck era: evolution of structural parameters for Einasto and NFW profiles. *MNRAS*, 441:3359–3374.
- Elbaz, D., Jahnke, K., Pantin, E., Le Borgne, D., and Letawe, G. (2009). Quasar induced galaxy formation: a new paradigm? *A&A*, 507:1359–1374.
- Fabian, A. C. (2012). Observational Evidence of Active Galactic Nuclei Feedback. *ARA&A*, 50:455–489.
- Falle, S. A. E. G. (1991). Self-similar jets. *MNRAS*, 250:581–596.
- Fan, X., Carilli, C. L., and Keating, B. (2006). Observational Constraints on Cosmic Reionization. *ARA&A*, 44:415–462.
- Fanaroff, B. L. and Riley, J. M. (1974). The morphology of extragalactic radio sources of high and low luminosity. *MNRAS*, 167:31P–36P.
- Fanidakis, N., Baugh, C. M., Benson, A. J., Bower, R. G., Cole, S., Done, C., Frenk, C. S., Hickox, R. C., Lacey, C., and Del P. Lagos, C. (2012). The evolution of active galactic nuclei across cosmic time: what is downsizing? *MNRAS*, 419:2797–2820.
- Fanidakis, N., Georgakakis, A., Mountrichas, G., Krumpe, M., Baugh, C. M., Lacey, C. G., Frenk, C. S., Miyaji, T., and Benson, A. J. (2013). Constraints on black hole fuelling modes from the clustering of X-ray AGN. *MNRAS*, 435:679–688.
- Fendt, C. and Sheikhnezami, S. (2013). Bipolar Jets Launched from Accretion Disks. II. The Formation of Asymmetric Jets and Counter Jets. *ApJ*, 774:12.
- Ferrarese, L. and Merritt, D. (2000). A fundamental relation between supermassive black holes and their host galaxies. *ApJLett*, 539:L9–L12.
- Field, G. B. (1965). Thermal Instability. *ApJ*, 142:531.
- Fields, B. and Sarkar, S. (2006). Big-Bang nucleosynthesis (Particle Data Group mini-review). *ArXiv Astrophysics e-prints*.
- Fryxell, B., Olson, K., Ricker, P., Timmes, F., Zingale, M., Lamb, D., MacNeice, P., Rosner, R., Truran, J., and Tufo, H. (2000). Flash: An adaptive mesh hydrodynamics code for modeling astrophysical thermonuclear flashes. *ApJS*, 131:273–334.
- Gaibler, V., Camenzind, M., and Krause, M. (2008). Large-scale propagation of very light jets in galaxy clusters. In Rector, T. A. and De Young, D. S., editors, *Extragalactic Jets: Theory and Observation from Radio to Gamma Ray*, volume 386 of *Astronomical Society of the Pacific Conference Series*, page 32.
- Gaibler, V., Khochfar, S., and Krause, M. (2011). Asymmetries in extragalactic double radio sources: clues from 3D simulations of jet-disc interaction. *MNRAS*, 411:155–161.

- 
- Gaibler, V., Khochfar, S., Krause, M., and Silk, J. (2012). Jet-induced star formation in gas-rich galaxies. *MNRAS*, 425:438–449.
- Gaspari, M., Brighenti, F., D’Ercole, A., and Melioli, C. (2011a). Agn feedback in galaxy groups: the delicate touch of self-regulated outflows. *MNRAS*, 415:1549–1568.
- Gaspari, M., Brighenti, F., and Ruszkowski, M. (2013). Solving the cooling flow problem through mechanical AGN feedback. *Astronomische Nachrichten*, 334:394.
- Gaspari, M., Brighenti, F., and Temi, P. (2012a). Mechanical agn feedback: controlling the thermodynamical evolution of elliptical galaxies. *MNRAS*, 424:190–209.
- Gaspari, M., Melioli, C., Brighenti, F., and D’Ercole, A. (2011b). The dance of heating and cooling in galaxy clusters: three-dimensional simulations of self-regulated active galactic nuclei outflows. *MNRAS*, 411:349–372.
- Gaspari, M., Ruszkowski, M., and Sharma, P. (2012b). Cause and Effect of Feedback: Multiphase Gas in Cluster Cores Heated by AGN Jets. *ApJ*, 746:94.
- Gerwin, R. A. (1968). Stability of the interface between two fluids in relative motion. *Rev. Mod. Phys.*, 40(3):652–658.
- Haardt, F. and Madau, P. (1996). Radiative Transfer in a Clumpy Universe. II. The Ultraviolet Extragalactic Background. *ApJ*, 461:20.
- Heinz, S., Brüggén, M., Young, A., and Levesque, E. (2006). The answer is blowing in the wind: simulating the interaction of jets with dynamic cluster atmospheres. *MNRAS*, 373:L65–L69.
- Hopkins, P. F. (2012). Dynamical delays between starburst and AGN activity in galaxy nuclei. *MNRAS*, 420:L8–L12.
- Ichimaru, S. (1977). Bimodal behavior of accretion disks - Theory and application to Cygnus X-1 transitions. *ApJ*, 214:840–855.
- Kaiser, C. R. and Alexander, P. (1997). A self-similar model for extragalactic radio sources. *MNRAS*, 286:215–222.
- Kannan, R., Stinson, G. S., Macciò, A. V., Brook, C., Weinmann, S. M., Wadsley, J., and Couchman, H. M. P. (2014). The MaGICC volume: reproducing statistical properties of high-redshift galaxies. *MNRAS*, 437:3529–3539.
- Kawakatu, N., Nagai, H., and Kino, M. (2008). The fate of young radio galaxies: Decelerations inside host galaxies? *ApJ*, 687:141–155.
- Kellermann, K. I., Vermeulen, R. C., Zensus, J. A., and Cohen, M. H. (1998). Sub-Milliarcsecond Imaging of Quasars and Active Galactic Nuclei. *AJ*, 115:1295–1318.
- Kharb, P., O’Dea, C. P., Baum, S. A., Daly, R. A., Mory, M. P., Donahue, M., and Guerra, E. J. (2008). A Study of 13 Powerful Classical Double Radio Galaxies. *ApJS*, 174:74–110.

- Kino, M. and Kawakatu, N. (2005). Estimate of the total kinetic power and age of an extragalactic jet by its cocoon dynamics: the case of cygnus a. *MNRAS*, 364:659–664.
- Komatsu, E., Smith, K. M., Dunkley, J., Bennett, C. L., Gold, B., Hinshaw, G., Jarosik, N., Larson, D., Nolta, M. R., Page, L., Spergel, D. N., Halpern, M., Hill, R. S., Kogut, A., Limon, M., Meyer, S. S., Odegard, N., Tucker, G. S., Weiland, J. L., Wollack, E., and Wright, E. L. (2011). Seven-year Wilkinson Microwave Anisotropy Probe (WMAP) Observations: Cosmological Interpretation. *ApJS*, 192:18.
- Krawczynski, H. and Treister, E. (2013). Active galactic nuclei – the physics of individual sources and the cosmic history of formation and evolution. *Frontiers of Physics*, 8:609–629.
- Laing, R. A. and Bridle, A. H. (2012). Relativistic jet models for two low-luminosity radio galaxies: evidence for backflow? *MNRAS*, 424:1149–1169.
- Lintott, C. J., Ferreras, I., and Lahav, O. (2006). Massive Elliptical Galaxies: From Cores to Halos. *ApJ*, 648:826–834.
- Liu, Y., Jiang, D. R., and Gu, M. F. (2006). The jet power, radio loudness, and black hole mass in radio-loud active galactic nuclei. *ApJ*, 637(2):669.
- Livio, M. (2004). Astrophysical Jets. *Baltic Astronomy*, 13:273–279.
- Macciò, A. V., Dutton, A. A., and Van Den Bosch, F. C. (2008). Concentration, spin and shape of dark matter haloes as a function of the cosmological model: Wmap1, wmap3 and wmap5 results. *MNRAS*, 391(4):1940–1954.
- McCarthy, I. G., Babul, A., Bower, R. G., and Balogh, M. L. (2008). Towards a holistic view of the heating and cooling of the intracluster medium. *MNRAS*, 386:1309–1331.
- McKinney, J. C. and Narayan, R. (2007). Disc-jet coupling in black hole accretion systems - I. General relativistic magnetohydrodynamical models. *MNRAS*, 375:513–530.
- McKinney, J. C., Tchekhovskoy, A., and Blandford, R. D. (2012). General relativistic magnetohydrodynamic simulations of magnetically choked accretion flows around black holes. *MNRAS*, 423:3083–3117.
- Meyer, M., Raue, M., Mazin, D., and Horns, D. (2012). Limits on the extragalactic background light in the Fermi era. *A&A*, 542:A59.
- Mizuta, A., Kino, M., and Nagakura, H. (2010). Hysteresis of Backflow Imprinted in Collimated Jets. *ApJLett*, 709:L83–L87.
- Mocz, P., Fabian, A. C., and Blundell, K. M. (2013). Cosmological growth and feedback from supermassive black holes. *MNRAS*, 432:3381–3390.
- Morsony, B. J., Miller, J. J., Heinz, S., Freeland, E., Wilcots, E., Brügggen, M., and Ruszkowski, M. (2013). Simulations of bent-double radio sources in galaxy groups. *MNRAS*, 431:781–792.

- 
- Moster, B. P., Somerville, R. S., Maulbetsch, C., van den Bosch, F. C., Macciò, A. V., Naab, T., and Oser, L. (2010). Constraints on the Relationship between Stellar Mass and Halo Mass at Low and High Redshift. *ApJ*, 710:903–923.
- Narayan, R. and McClintock, J. E. (2008). Advection-dominated accretion and the black hole event horizon. *New Astron.Rev.*, 51:733–751.
- Narayan, R. and Yi, I. (1994). Advection-dominated accretion: A self-similar solution. *ApJLett*, 428:L13–L16.
- Navarro, J. F., Frenk, C. S., and White, S. D. M. (1996). The Structure of Cold Dark Matter Halos. *ApJ*, 462:563.
- Noble, S. C., Krolik, J. H., Schnittman, J. D., and Hawley, J. F. (2011). Radiative Efficiency and Thermal Spectrum of Accretion onto Schwarzschild Black Holes. *ApJ*, 743:115.
- Norman, M. L., Winkler, K.-H. A., Smarr, L., and Smith, M. D. (1982). Structure and dynamics of supersonic jets. *A&A*, 113:285–302.
- Nulsen, P. E. J. and McNamara, B. R. (2013). AGN feedback in clusters: Shock and sound heating. *Astronomische Nachrichten*, 334:386.
- Owen, F. N. and Ledlow, M. J. (1994). The FRI/II Break and the Bivariate Luminosity Function in Abell Clusters of Galaxies. In Bicknell, G. V., Dopita, M. A., and Quinn, P. J., editors, *The Physics of Active Galaxies*, volume 54 of *Astronomical Society of the Pacific Conference Series*, page 319.
- Page, D. N. and Thorne, K. S. (1974). Disk-Accretion onto a Black Hole. Time-Averaged Structure of Accretion Disk. *ApJ*, 191:499–506.
- Parma, P., Murgia, M., Morganti, R., Capetti, A., de Ruiter, H. R., and Fanti, R. (1999). Radiative ages in a representative sample of low luminosity radio galaxies. *A&A*, 344:7–16.
- Pellegrini, S. (2011). The Temperature of Hot Gas Halos of Early-type Galaxies. *ApJ*, 738:57.
- Penna, R. F., Narayan, R., and Sądowski, A. (2013). General relativistic magneto-hydrodynamic simulations of blandford-znajek jets and the membrane paradigm. *MNRAS*, 436:3741–3758.
- Penna, R. F., Sądowski, A., and McKinney, J. C. (2012). Thin-disc theory with a non-zero-torque boundary condition and comparisons with simulations. *MNRAS*, 420:684–698.
- Perucho, M. and Martí, J. M. (2007). A numerical simulation of the evolution and fate of a Fanaroff-Riley type I jet. The case of 3C 31. *MNRAS*, 382:526–542.
- Perucho, M., Martí, J. M., Laing, R. A., and Hardee, P. E. (2014a). On the deceleration of Fanaroff-Riley Class I jets: mass loading by stellar winds. *MNRAS*, 441:1488–1503.

- Perucho, M., Martí, J.-M., Quilis, V., and Ricciardelli, E. (2014b). Large-scale jets from active galactic nuclei as a source of intracluster medium heating: cavities and shocks. *MNRAS*, 445:1462–1481.
- Psaltis, D. (2008). Probes and tests of strong-field gravity with observations in the electromagnetic spectrum. *Living Reviews in Relativity*, 11(9).
- Quataert, E. and Gruzinov, A. (2000). Convection-dominated Accretion Flows. *ApJ*, 539:809–814.
- Rossi, P., Mignone, A., Bodo, G., Massaglia, S., and Ferrari, A. (2008). Formation of dynamical structures in relativistic jets: the FRI case. *A&A*, 488:795–806.
- Rybicki, G. B. and Lightman, A. P. (2007). *Radiative Processes in Astrophysics*. Wiley-VCH Verlag GmbH.
- Sadler, E. M., Jackson, C. A., Cannon, R. D., McIntyre, V. J., Murphy, T., Bland-Hawthorn, J., Bridges, T., Cole, S., Colless, M., Collins, C., Couch, W., Dalton, G., De Propris, R., Driver, S. P., Efstathiou, G., Ellis, R. S., Frenk, C. S., Glazebrook, K., Lahav, O., Lewis, I., Lumsden, S., Maddox, S., Madgwick, D., Norberg, P., Peacock, J. A., Peterson, B. A., Sutherland, W., and Taylor, K. (2002). Radio sources in the 2dF Galaxy Redshift Survey - II. Local radio luminosity functions for AGN and star-forming galaxies at 1.4 GHz. *MNRAS*, 329:227–245.
- Sadowski, A., Narayan, R., Penna, R., and Zhu, Y. (2013). Energy, momentum and mass outflows and feedback from thick accretion discs around rotating black holes. *ArXiv e-prints*: 1307.1143.
- Saikia, D. J. and Jamrozy, M. (2009). Recurrent activity in Active Galactic Nuclei. *Bulletin of the Astronomical Society of India*, 37:63–89.
- Schawinski, K., Khochfar, S., Kaviraj, S., Yi, S. K., Boselli, A., Barlow, T., Conrow, T., Forster, K., Friedman, P. G., Martin, D. C., Morrissey, P., Neff, S., Schiminovich, D., Seibert, M., Small, T., Wyder, T. K., Bianchi, L., Donas, J., Heckman, T., Lee, Y.-W., Madore, B., Milliard, B., Rich, R. M., and Szalay, A. (2006). Suppression of star formation in early-type galaxies by feedback from supermassive black holes. *Nature*, 442:888–891.
- Schaye, J., Crain, R. A., Bower, R. G., Furlong, M., Schaller, M., Theuns, T., Dalla Vecchia, C., Frenk, C. S., McCarthy, I. G., Helly, J. C., Jenkins, A., Rosas-Guevara, Y. M., White, S. D. M., Baes, M., Booth, C. M., Camps, P., Navarro, J. F., Qu, Y., Rahmati, A., Sawala, T., Thomas, P. A., and Trayford, J. (2014). The EAGLE project: Simulating the evolution and assembly of galaxies and their environments. *ArXiv e-prints*.
- Scheuer, P. A. G. (1982). Morphology and power of radio sources. In Heeschen, D. S. and Wade, C. M., editors, *Extragalactic Radio Sources*, volume 97 of *IAU Symposium*, pages 163–165.
- Schmidt, M. (1959). The Rate of Star Formation. *ApJ*, 129:243.

- 
- Shakura, N. I. and Sunyaev, R. A. (1973). Black holes in binary systems. Observational appearance. *A&A*, 24:337–355.
- Shapiro, P. R., Iliev, I. T., and Raga, A. C. (1999). A model for the post-collapse equilibrium of cosmological structure: truncated isothermal spheres from top-hat density perturbations. *MNRAS*, 307:203–224.
- Sheikhnezami, S., Fendt, C., Porth, O., Vaidya, B., and Ghanbari, J. (2012). Bipolar Jets Launched from Magnetically Diffusive Accretion Disks. I. Ejection Efficiency versus Field Strength and Diffusivity. *ApJ*, 757:65.
- Sijacki, D., Springel, V., Di Matteo, T., and Hernquist, L. (2007a). A unified model for AGN feedback in cosmological simulations of structure formation. *MNRAS*, 380:877–900.
- Sijacki, D., Springel, V., Di Matteo, T., and Hernquist, L. (2007b). A unified model for agn feedback in cosmological simulations of structure formation. *MNRAS*, 380:877–900.
- Silk, J. (2013). Unleashing Positive Feedback: Linking the Rates of Star Formation, Supermassive Black Hole Accretion and Outflows in Distant Galaxies. *ArXiv e-prints: 1305.5840*.
- Silk, J. and Rees, M. J. (1998). Quasars and galaxy formation. *A&A*, 331:L1–L4.
- Somerville, R. S., Hopkins, P. F., Cox, T. J., Robertson, B. E., and Hernquist, L. (2008a). A semi-analytic model for the co-evolution of galaxies, black holes and active galactic nuclei. *MNRAS*, 391:481–506.
- Somerville, R. S., Hopkins, P. F., Cox, T. J., Robertson, B. E., and Hernquist, L. (2008b). A semi-analytic model for the co-evolution of galaxies, black holes and active galactic nuclei. *MNRAS*, 391:481–506.
- Springel, V. (2010). E pur si muove: Galilean-invariant cosmological hydrodynamical simulations on a moving mesh. *MNRAS*, 401:791–851.
- Stinson, G. S., Bovy, J., Rix, H.-W., Brook, C., Roškar, R., Dalcanton, J. J., Macciò, A. V., Wadsley, J., Couchman, H. M. P., and Quinn, T. R. (2013). MaGICC thick disc - I. Comparing a simulated disc formed with stellar feedback to the Milky Way. *MNRAS*, 436:625–634.
- Sutherland, R. S. and Bicknell, G. V. (2007). Interaction of jets with the ism of radio galaxies. *Ap&SS*, 311:293–303.
- Sutherland, R. S. D. M. A. (1993). Cooling functions for low-density astrophysical plasmas. *ApJS(ISSN 0067-0049)*, 88(1):253–327.
- Taylor, A. M., Vovk, I., and Neronov, A. (2011). Extragalactic magnetic fields constraints from simultaneous GeV-TeV observations of blazars. *A&A*, 529:A144.
- Tchekhovskoy, A., McKinney, J. C., and Narayan, R. (2012). General relativistic modeling of magnetized jets from accreting black holes. *Journal of Physics Conference Series*, 372(1):012040.

- Tooper, R. F. (1969). Entropy of a relativistic electron gas. *ApJ*, 157:1391.
- Tortora, C., Antonuccio-Delogu, V., Kaviraj, S., Silk, J., Romeo, A. D., and Becciani, U. (2009). AGN jet-induced feedback in galaxies - II. Galaxy colours from a multcloud simulation. *MNRAS*, 396:61–77.
- van Velzen, S., Falcke, H., and Koerding, E. (2014). Nature and evolution of powerful radio galaxies and their link with the quasar luminosity function. *ArXiv e-prints*.
- Vernaleo, J. C. and Reynolds, C. S. (2006). AGN Feedback and Cooling Flows: Problems with Simple Hydrodynamic Models. *ApJ*, 645:83–94.
- Vogelsberger, M., Genel, S., Sijacki, D., Torrey, P., Springel, V., and Hernquist, L. (2013). A model for cosmological simulations of galaxy formation physics. *MNRAS*, 436:3031–3067.
- Vogelsberger, M., Genel, S., Springel, V., Torrey, P., Sijacki, D., Xu, D., Snyder, G. F., Nelson, D., and Hernquist, L. (2014). Introducing the Illustris Project: Simulating the coevolution of dark and visible matter in the Universe. *ArXiv e-prints*.
- Wagner, A. Y. and Bicknell, G. V. (2011). Relativistic Jet Feedback in Evolving Galaxies. *ApJ*, 728:29.
- Wagner, A. Y., Bicknell, G. V., and Umemura, M. (2012). Driving Outflows with Relativistic Jets and the Dependence of Active Galactic Nucleus Feedback Efficiency on Interstellar Medium Inhomogeneity. *ApJ*, 757:136.
- Walg, S., Achterberg, A., Markoff, S., Keppens, R., and Meliani, Z. (2013). Relativistic agn jets i. the delicate interplay between jet structure, cocoon morphology and jet-head propagation. *ArXiv e-prints: 1305.2157*.
- Yao, Y., Shull, J. M., Wang, Q. D., and Cash, W. (2012). Detecting the Warm-Hot Inter-galactic Medium through X-Ray Absorption Lines. *ApJ*, 746:166.

# Acknowledgements

The software used in this work was in part developed by the DOE NNSA-ASC OASCR Flash Center at the University of Chicago. The simulations have been performed and analyzed on the HYDRA, THEO and VIZ cluster at the RechenZentrum Garching (RZG) of the Max Planck Society.

\* \* \*

Thanks to my supervisor Andrea Macciò, for the constant close guidance and support, for the time and dedication put in supervising my work during my PhD, for chasing me when occasionally I wandered on my own, for being understanding and friendly, for caring about my scientific and human growth.

Thanks to my advisor Vincenzo Antonuccio-Delogu, to whom I really owe much, not just professionally; for the helpful comments, for the patience shown on our long office calls, for our programming sessions, sometimes for just solving the problem, for caring about my social network.

Thanks to Andrea and to Björn Malte Schäfer for agreeing to referee my thesis; thanks as well to Luca Amendola and Henrik Beuther for being part of my defense committee.

Thanks to everyone in the Galaxy Formation Group for always making me feel in the right place and valorising my work.

Thanks to my collaborators Nikolaos Fanidakis and Alessio Romeo Veloná.

Thanks to the whole IMPRS and its coordinator Christian Fendt, for giving me and my fellow students this chance of being together.

Thanks to my friends from IMPRS, generations 6, 7, 8, 9 and 10 for the great time spent together! They are just too many to list them all!

Thanks to the wonderful people of office 225 (present and past), for our instructive discussions, for the frequents rides up and down the hill, for our funny jokes, and for making every day special.

Thanks to my family, “mamma” Lia, “papà” Gianni and Federico, for always finding a way to stay close to me even when physically far away.

- S. C. -